

Markus Henrikssønn Blytt

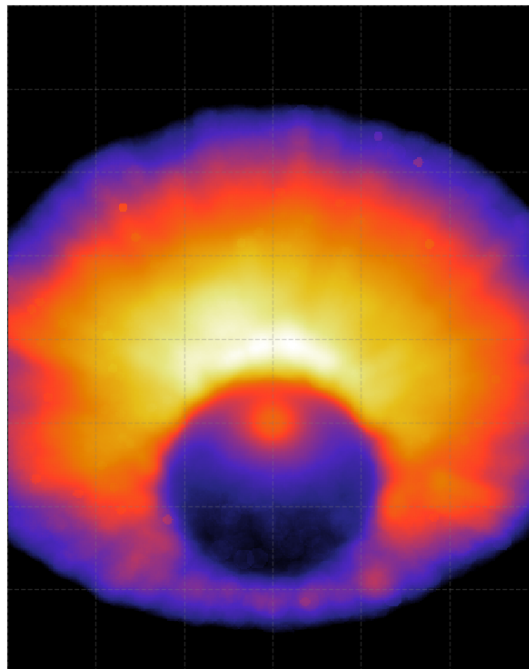
Implementation of Three-Dimensional Electromagnetic Cascades into Elmag

Master's thesis in Applied Physics and Mathematics

Supervisor: Michael Kachelrieß

June 2019

NTNU
Norwegian University of Science and Technology
Faculty of Natural Sciences
Department of Physics



Markus Henrikssønn Blytt

Implementation of Three-Dimensional Electromagnetic Cascades into Elmag

Master's thesis in Applied Physics and Mathematics
Supervisor: Michael Kachelrieß
June 2019

Norwegian University of Science and Technology
Faculty of Natural Sciences
Department of Physics

 **NTNU**
Norwegian University of
Science and Technology

“It’s not that I’m so smart , it’s just that I stay with problems longer.”

- Albert Einstein

Abstract

A development of the Monte Carlo program ELMAG is presented. The program simulates electromagnetic cascades initiated by high energy γ -rays interacting with the extragalactic background light, producing charged particles that are deflected in the extragalactic magnetic field and again interact with the background photons. ELMAG calculates now the three-dimensional evolution of the cascade with deflections by a turbulent magnetic field. The magnetic field considered is helical, because theoretical predictions suggest that detecting polarization in such a field can prove CP violation in the Early Universe. The particle physics of electromagnetic cascades and the generation of a turbulent magnetic field is presented. An appropriate numerical solver is chosen, and tested against analytic formulae to provide sufficient proof of a correct implementation. The complete Monte Carlo program is made as general as possible, and is explained in detail, to make it easy for a user to specify desired input and output routines. Results from the program are in satisfying agreement with other programs in the high energy regime. A consequence of the desired efficiency in the program is that it should only be applied for photon energies above ~ 1 GeV. As final results, the simulations from the program provide surface brightness band images of the γ -ray sky around the blazar 1ES 0229+200. The spectra of time delayed secondary particles are evaluated, and are in good agreement with theoretical predictions. Left-handed and right-handed polarizations of the magnetic field lead to different deformations of the observed band image. However, a more detailed statistical treatment is required to make a reliable test for the polarization of the extragalactic magnetic field.

Sammendrag

En oppdatert versjon av Monte Carlo programmet ELMAG er presentert. Programmet simulerer elektromagnetiske kaskader som startes av høyenergiske fotoner fra kvasarer. De høyenergiske fotonene vekselvirker med bakgrunnsfotoner og produserer elektron-positron par, som blir bøyd av et kosmologisk magnetisk felt, og deretter vekselvirker igjen med andre bakgrunnsfotoner. ELMAG kan nå ta høyde for den tredimensjonal utviklingen av kaskaden i et turbulent magnetisk felt. Det magnetiske feltet i programmet er en turbulent superposisjon av helikser, da det er ønskelig å undersøke polarisasjon i et kosmologisk magnetisk felt, som kan bevise ulikheter i oppførselen til matterie og antimatterie i Universets begynnelse. Partikkelfysikken bak de elektromagnetiske kaskadene blir utledet, samt en beskrivelse av hvordan det magnetiske feltet blir generert. En avansert numerisk rutine blir presentert for å beregne partikkelbanen i det turbulente magnetiske feltet. Flere tester er blitt utført for bevise at den numeriske rutinen fungerer som ønskelig. Det ferdige programmet er laget så generelt som mulig, og blir beskrevet i detalj for å la enhver bruker tilpasse programmet til ønskelig formål. Programmet gir gode resultater når det sammenlignes med andre tilsvarende simuleringer. Dog anbefales programmet kun for bruk når det simuleres for energier høyere enn ~ 1 GeV. Som sluttresultat presenteres band bilder av overflatelystyrken fra blasaren 1ES 0229+200. Teoretisk forventning av tidsforsinkelse for avbøyde partikler er i overensstemmelse med resultatene fra programmet. Venstrehåndspolarisasjon og høyrehåndspolarisasjon av det magnetiske feltet blir også evaluert. Det oppstår en tydelig forskjell i de respektive band bildene. Dog er dette tilfellet for kun ett sett av tilfeldige parametre som initialiserer magnetfeltet. Det konkluderes dermed med at det må opparbeides mer statistikk før man kan dra en troverdig konklusjon på hvordan venstrehånds- og høyrehåndspolarisasjon vil påvirke band bildet ulikt.

Preface

This Master thesis concludes my five years of study at the department of Applied Physics and Mathematics at NTNU. It has been five challenging, but joyful years. In my fourth year, I had the opportunity of doing an exchange year at ETH (Eidgenössische Technische Hochschule) in Zürich. This was a truly exciting year, which motivated me to pursue a thesis in astroparticle physics.

I would like to thank my supervisor Prof. Michael Kachelrieß for the opportunity to do my thesis in what I think is one of the most interesting areas of physics. It has been a challenging year, with many pitfalls and long nights, but with the indispensable help from Prof. Michael Kachelrieß, we have managed to complete the objectives of the thesis.

During the final month of completing this thesis my friends, colleagues, and girlfriend have been paramount in maintaining my motivation and persistence. Late night coffee breaks, chats and phone calls are among many of the little things that I have truly appreciated. I would also like to thank my parents for the unconditional support over almost a quarter century, and all my good friends in Trondheim and Zürich for the good memories from my five years of study.

Finally, I would like to send my regards to my high school physics teacher, who was one of the main reasons I have pursued further education within physics.

Abstract	i
Sammendrag	iii
Preface	v
List of Tables	ix
List of Figures	xi
1 Introduction	1
1.1 Motivation	1
1.2 Approach	3
1.3 Objective	3
1.4 Structure of the Thesis	4
2 Theoretical Background	5
2.1 Terminology	5
2.2 Standard Model of Cosmology	5
2.3 Blazar	6
2.4 Extragalactic Background Light	8
2.5 Primordial Magnetic Field	9
3 Scattering on the Extragalactic Background Light	13
3.1 Standard Model of Particle Physics	13
3.1.1 Feynman Diagrams - QED	14
3.1.2 Pair Production	15
3.1.3 Inverse Compton Scattering	17
3.2 Modeling of Electron-Photon Interactions	18
3.3 Analysis of Extragalactic Interactions	20
4 Modeling and Deflection in the Extragalactic Magnetic Field	25
4.1 Generation of a Turbulent Magnetic Field	25
4.2 Deflection in a Turbulent Magnetic Field	27

5 The Program: ELMAG	35
5.1 Modeling of the Cascade	35
5.2 Program Structure	39
5.3 Example Inputs/Outputs	42
5.3.1 Input parameters and variables	42
5.3.2 Output	44
5.4 Additional Theory for Interpreting the Results	45
5.4.1 Qualitative Analysis	45
5.4.2 Time Delay	46
5.4.3 Energy Distribution	46
6 Results and Discussion	47
6.1 Comparison to Old Program	47
6.1.1 Old Program Implementation	50
6.2 Tests of the New Program	50
6.3 Sky Images	52
6.4 Future Work	60
7 Conclusion	63
Bibliography	65
Acronyms	69
Appendices	71
A Mandelstam Variables	73
B Additional Figures	75

LIST OF TABLES

3.1	The Feynman Rules of QED	15
4.1	Magnetic field correlation lengths	30
4.2	Summary of initial parameters for the numerical solver	33
6.1	List of time bins used in the simulations of the band images	53
6.2	Expected angular brightness offset	54

LIST OF FIGURES

2.1 Spectral energy distribution of Markarian 421	7
2.2 Measurement of the EBL	8
2.3 Constraints on the primordial magnetic field	10
3.1 Example QED vertices	14
3.2 Tree level diagrams of pair production	16
3.3 Tree level diagrams of inverse Compton scattering	17
3.4 Cross section of pair production with the EBL	21
3.5 Cross section of IC scattering in the center-of-momentum frame	22
4.1 Deflection in magnetic fields with Kolmogorov, Kraichnan and Bohm turbulence	31
4.2 Deflection in polarized magnetic fields	32
4.3 Deflection in magnetic fields for different error thresholds	32
5.1 Sketch of angle delay calculation in the program	38
5.2 Qualitative sketch of particle track from source to the Earth	45
6.1 Photon and electron-positron spectrum	48
6.2 Photon spectrum inside and outside ϑ_{95}	48
6.3 Photon spectrum split into time bins of arrival time	49
6.4 Old routines in new program compared to old program	50
6.5 Helical motion of a charged particle in a uniform magnetic field	51
6.6 Surface brightness plot comparable to results from Elyiv et al.	52
6.7 Band image for $E_{\gamma_0} = 1$ TeV, $\Theta_{\text{obs}} = 0^\circ$ and $B_{\text{rms}} = 10^{-15}$ G	54
6.8 Band image for $E_{\gamma_0} = 1$ TeV, $\Theta_{\text{obs}} = 3^\circ$ and $B_{\text{rms}} = 10^{-16}$ G	55
6.9 Band image for $E_{\gamma_0} = 1$ TeV, $\Theta_{\text{obs}} = 6^\circ$ and $B_{\text{rms}} = 10^{-14}$ G	55
6.10 Band image for $\Theta_{\text{obs}} = 3^\circ$ and $B_{\text{rms}} = 10^{-14}$ G	56
6.11 Band image for $\Theta_{\text{obs}} = 3^\circ$ and $B_{\text{rms}} = 10^{-15}$ G	57
6.12 Band image for $\Theta_{\text{obs}} = 6^\circ$ and $B_{\text{rms}} = 10^{-15}$ G	58
6.13 Time integrated band image for $\Theta_{\text{obs}} = 6^\circ$ and $B_{\text{rms}} = 10^{-13} - 10^{-16}$ G	59

A.1	Feynman diagrams representing the Mandelstam variables	73
B.1	Surface brightness plot from Elyiv et al.	75
B.2	Band image for $\Theta_{\text{obs}} = 3^\circ$ and $B_{\text{rms}} = 10^{-13}$ G	76
B.3	Band image for $\Theta_{\text{obs}} = 3^\circ$ and $B_{\text{rms}} = 10^{-16}$ G	77
B.4	Band image for $\Theta_{\text{obs}} = 6^\circ$ and $B_{\text{rms}} = 10^{-13}$ G	78
B.5	Band image for $\Theta_{\text{obs}} = 6^\circ$ and $B_{\text{rms}} = 10^{-14}$ G	79
B.6	Band image for $\Theta_{\text{obs}} = 6^\circ$ and $B_{\text{rms}} = 10^{-16}$ G	80

1.1 MOTIVATION

The ultimate aim of physicists is to understand how the Universe works. To that end, everything from subatomic interactions to the gravitational pull from black holes can be described by using theories and models. Two of the most acknowledged and verified theories are the Standard Model of particle physics and the Standard Model of cosmology.

The Standard Model of particle physics requires that to create matter there also has to be created antimatter. If this is the model to describe the Universe, naively there should exist as much matter as antimatter. However, measurements indicate that the observed Universe consists almost entirely of matter. A possible explanation is that antimatter cannot be observed using today's technology. However, this is improbable, as antimatter in the Standard Model of particle physics follows the same laws of quantum electrodynamics (QED) as matter. Alternatively, the expected amount of antimatter could exist in the Universe, but in a part outside the observable boundaries. This would be a simple explanation but for now an improvable theory. Further, it is possible that the Standard Model of particle physics is incomplete, which is a thesis currently undergoing heavy research.

In cosmology, it is possible to estimate the beginning of the Universe by finding its expansion rate. This rate implies that the Universe started 15 billion years ago [1] (in fact, more recent studies by WMAP indicate that the Universe is ~ 13.8 yr old [2]). During the first 10^{-32} seconds the Universe experienced an inflation process, where its volume expanded by a factor of more than 10^{78} . During inflation or shortly after, the Universe probably experienced baryogenesis. Baryogenesis is a hypothetical physical process that creates a baryon asymmetry, i.e. matter and antimatter are produced at different rates. However, for baryogenesis to occur, some conditions must hold in the Early Universe. These are called the Sakharov conditions and are:

- Baryon-number-violating processes.
- Violation of C and CP symmetry.

- Interactions out of thermal equilibrium.

Violation of C and CP symmetry means that the physics are not the same for matter and antimatter, and will henceforth be referred to as CP violation. In the electroweak sector of the Standard Model of particle physics, CP violation is allowed theoretically and has also been verified experimentally. However, calculations show that CP violation in the Standard Model of particle physics cannot account for baryogenesis. Therefore, CP violations in the Early Universe must be further investigated. To investigate this it would be beneficial to observe the Early Universe.

In 1963 Penzias and Wilson accidentally detected a faint signal in the cosmological microwave regime [3]. The detection was first proposed as noise due to bird droppings on the antennas, but after a thorough cleaning and further analysis of more data, the detection was categorized as a signal. Today, this signal is known as the cosmic microwave background (CMB). The CMB is a photon map of the Early Universe, where the photons decoupled (recombination), and electrons and protons were for the first time free to form hydrogen. The decoupling of photons is defined as the first time photons could travel freely through the Universe, meaning they did not constantly interact with matter. By analyzing and interpreting the CMB, observation of the Early Universe became possible. Even though the CMB is considered very old, it depicts the Universe as late as $\sim 400\,000$ yr after the Big Bang. To look at the even earlier Universe one could observe the cosmic neutrino background (C ν B), which would provide a picture of a one second old Universe, where the neutrinos decoupled for the first time. Unfortunately, it is not possible to observe and map the C ν B at this time, but this might become possible with future technology. For now, it is more convenient to look for other parts of the primordial Universe for inspiration.

To prove CP violation in the Early Universe, it would be interesting to look for other primordial parts of the Universe, e.g. primordial gravitational waves or a primordial magnetic field. The latter is of particular interest as it has been theorized as the cause of the extragalactic magnetic field (EGMF). If the EGMF is a primordial magnetic field, it means that it was created during or shortly after the inflation process. It has been stretched out and deformed as the Universe continuously expands. In perspective of the length of the Universe, it looks turbulent, but at a length scale of a typical distance between galaxies, e.g. ~ 1 Mpc, the field might be coherent. This length scale is the correlation length of the magnetic field and could determine when such a magnetic field was created, i.e. during or after the inflation process. The correlation length would not prove CP violation by itself. However, it defines where the magnetic field can be considered homogeneous, which is necessary to understand the other parameters of the EGMF, i.e. field strength and polarization. By observing very high energy (VHE) γ -rays from a point source, e.g. a blazar, it is possible to probe the EGMF along different lines of sights. This provides independent samples of the EGMF. Now, if one would add up all probed parts of the EGMF and there was a clear overweight of left- or right-handed polarization, it would be a clear sign of CP violation in the Early Universe. In fact, Tashiro et al. have done a study where they predict a left-handed polarization of the cosmological magnetic field [4], assuming that the field is helical. The EGMF might be different along each line of sight, and the distance a photon travels would probably consist of many correlation lengths, which yields many possibilities of the parameters of the EGMF. Hence, the helicity

of the total EGMF could be anywhere in between fully left-handed polarization and fully right-handed polarization.

Probing extragalactic γ -ray point sources could be very interesting for particle physics and Early Universe cosmology. Assuming the EGMF is helical, the polarization of the field could prove CP violation in the Early Universe. In order to distinguish different polarization of the EGMF, it is crucial to know which signals to look for in the γ -ray sky. A Monte Carlo program simulating the physical processes between a point source and Earth could provide results to cross-reference with detector data. This way, the detector specialists would know what to expect for any given polarization, correlation length and field strength of the EGMF, for any desired source.

1.2 APPROACH

This thesis will be about the development of the program ELMAG [5]. ELMAG is a Monte Carlo program for the simulation of electromagnetic cascades initiated by VHE γ -rays and electrons interacting with the extragalactic background light (EBL). The primary γ -rays interact with the EBL by pair production and produce secondary charged particles, which again interact with the EBL to produce lower energetic γ -rays. The charged particles will be deflected by the EGMF, which distorts the observed sky image of the point source. By extending the program to simulate electromagnetic cascades in the three-dimensional space, and also accounting for a turbulent EGMF, theoretical predictions for expected sky images will be available. The results from ELMAG would depend on the correlation length, polarization and field strength of the EGMF. Then, by cross-referencing simulated sky images with observations from detectors on Earth, e.g. Fermi, it could be possible to infer further constraints on the parameters of the EGMF.

The next step in the program is to develop routines for implementing a turbulent magnetic field and simulating the three-dimensional cascade. For solving the differential equation of the Lorentz force in a turbulent magnetic field, a precise numerical algorithm is needed. Considering this is a Monte Carlo program, the numerical solver also has to be computing efficient. An adaptive stepsize Runge-Kutta solver will be used. The numerical solver will be tested extensively to ensure that the correct normalization is being used, and more importantly, that the implementation is done appropriately concerning the other routines in the program. This will be done by simulating the trajectory of non-cascading charged particles in turbulent and uniform magnetic fields.

This thesis will also be a standalone presentation of the complete program. Thus, including the theory of particle physics, generation of a turbulent magnetic field, and description of routines from the old version of ELMAG that has not been changed in this release.

1.3 OBJECTIVE

The main objectives in this thesis was:

- To implement a turbulent magnetic field and choose an appropriate numerical solver. The solver was tested against analytic formulae for charged particle propagation in both turbulent and uniform magnetic fields, to provide sufficient proof that the numerical routine works as expected.
- To change the stack and all other affected routines in the program, to take into account the three-dimensional evolution of the cascade.
- To employ the new Monte Carlo program, and test it against results from other similar programs.
- To produce sky images of the blazar 1ES +229+200, and test for polarizations in the EGMF.

1.4 STRUCTURE OF THE THESIS

The thesis will start by defining some basic terminology in astroparticle physics, and explaining the necessary theoretical background for the EBL and EGMF in chapter 2. Thereafter, in chapter 3, the fundamental particle physics needed to understand and calculate particle interactions with the EBL will be presented. How to implement the particle physics theory into the program will also be described. The end of chapter 3 will present an analysis of extragalactic interactions, which will introduce how a TeV point source could have a GeV halo by indirect deflection from the EGMF. This gives motivation for chapter 4, which starts by describing the numerical routine of implementing a helical turbulent magnetic field into the program. Considering the EGMF is turbulent, the trajectory of a charged particle cannot be solved analytically. Hence, in chapter 4 a detailed analysis of what numerical solver to use will be presented. After providing all the necessary theory to understand extragalactic interactions and how to make computational predictions of an electromagnetic cascade and deflection, the program will be presented in chapter 5. The core routines of the program and an example file for inputs/outputs will be explained in this chapter. The chapter also includes a final section with some necessary formulae to analyze and interpret the results. Finally, in chapter 6, the results from the simulations done with the newly developed program will be presented. The main results will be simulations done on the blazar 1ES 0229+200, where different polarization of the EGMF will be tested.

CHAPTER 2

THEORETICAL BACKGROUND

In this chapter the necessary theoretical background and terminology for the thesis will be introduced. First, in section 2.1 a brief explanation of some relevant terminology used in astroparticle physics will be presented. Second, in section 2.2, a short description of the Standard Model of cosmology will be given. Then, in section 2.3, blazars, how they work and are detected, and their importance in VHE γ -ray astronomy will be presented. An introduction of the EBL together with the CMB will be presented in section 2.4, then the theory of a primordial magnetic field resulting in the EGMF is explained in section 2.5. The importance in this chapter will be to understand the consequences of relics from the Early Universe.

2.1 TERMINOLOGY

In this thesis it will be essential to know the definition of words that are frequently used in astroparticle physics. The Early Universe refers to the time between inflation and recombination. Primordial is used to describe something that has existed since the Early Universe, e.g. a primordial field is a field that was generated in the Early Universe and still exists, or a primordial black hole would be a black hole made shortly after the inflation process. Extragalactic is commonly used to define something outside the Milky Way Galaxy, but in this thesis, it will primarily refer to the extragalactic magnetic field or the extragalactic background light, i.e. the magnetic field or background light in between galaxies. Correlation length is a term that will be used frequently throughout the thesis. A turbulent field can be considered as a slowly varying function at some distance scale, which defines the field's correlation length.

2.2 STANDARD MODEL OF COSMOLOGY

The Standard Model of cosmology is the model used to describe the evolution of the Universe after the inflation process. When Penzias and Wilson determined the existence of the CMB

from 1963 to 1964, it became widely accepted that the Universe started in a hot, dense state. Different models were made to explain how the expansion evolved after this state. These models are often referred to as Big Bang models, as they illustrate the Universe starting in a dense state and expanding to what is observable today. This gave rise to the question of how the Universe expands. In 1998 it was observed that the Universe is expanding at an accelerating pace [6], which strongly favored the so-called Λ CDM-model. Further observations also supported the Λ CDM-model, hence it became the commonly used Standard Model of cosmology. Λ refers to the dark energy, and CDM is the acronym for cold dark matter. This is because the model provides a description of a universe which mainly consists of dark energy and dark matter. However, the model does not yet completely explain why the Universe has an excess of matter compared to antimatter, thus the continuous search for indications of CP violation in the Early Universe.

2.3 BLAZAR

A few percent of all galaxies are characterized by a compact and exceptionally luminous central region, so bright that it outshines the rest of the galaxy. These objects are galaxies that host a so-called Active Galactic Nucleus (AGN). AGNs probably consist of a supermassive spinning black hole in the center, surrounded by an accretion disk. An accretion disk is formed when a black hole is constantly supplied with mass. When the gravitational energy is released from the accretion disk, jets perpendicular to the spin axis are formed. This must happen before matter in the accretion disc reaches the event horizon of the black hole. The jets emit photons in the energy regime from radio to more than TeV γ -rays, characterizing a detection of an AGN. These objects are some of the most important extragalactic cosmic ray (CR) sources and are believed to be the origin of the most energetic CRs observed on Earth. Little is known about the acceleration mechanism, but observation of VHE γ -rays directly from AGNs have been made. [7]

Quasar is the name of the most luminous AGNs. The name originates from quasi-stellar radio source as it was first detected in the radio regime. To detect a quasar the jet would have to point towards the Earth within a small angle. Only then would it be possible to measure the flux of electromagnetic wavebands emitted from the object, which is important to categorize the AGN. In this case, it is crucial to determine whether the AGN is radio-loud or radio-quiet. To check if it is radio-loud, the following inequality must hold

$$f_{5\text{GHz}} \geq f_B, \tag{2.1}$$

where $f_{5\text{GHz}}$ and f_B correspond to the flux of photons in radio at 5 GHz and the optical band respectively. Most quasars are radio-quiet, and thus of no interest in this report, but about 10 – 15 % emit radiation that satisfies Eq.(2.1), which makes them radio-loud. A radio-loud quasar with a jet pointing towards Earth is called a blazar, and is assumed to be the object accelerating particles to the highest observed energies. This makes blazars very interesting and important for both cosmic rays and γ -ray astronomy, especially since blazars are the vast majority of the observed high energy photon sources. It is easy to determine the source of a photon because the photon does not experience deflection from electromagnetic fields on its

path. For CRs (mostly protons), which are charged particles, the accumulated deflection from magnetic fields can be significant, and one would need a good magnetic map to backtrack the path, thus it is difficult to determine its origin. However, in this thesis, only the photons are of importance.

A blazars spectral energy distribution can further categorize it. Typically for blazars is a two-peaked distribution with one peak in the lower frequency regime, e.g. radio to UV, and a second in the high-frequency regime, e.g. X-ray to γ -ray. When categorizing the blazar one looks at the lower energy band and at what frequency ν_S the energy flux peaks. The frequency at this peak defines the blazar as Low-Energy peaked or high-energy peaked, given by $10^{13} \text{ Hz} < \nu_S^{\text{peak}} < 10^{14} \text{ Hz}$ and $10^{15} \text{ Hz} < \nu_S^{\text{peak}}$, respectively. One of the brightest sources in the extragalactic sky is Markarian 421 (Mrk 421). Mrk 421 is a High-Energy peaked blazar at redshift $z \approx 0.03$. It has been measured with almost all Imaging Atmospheric Cherenkov Telescopes (IACTs), and identified as a TeV emitter [8].

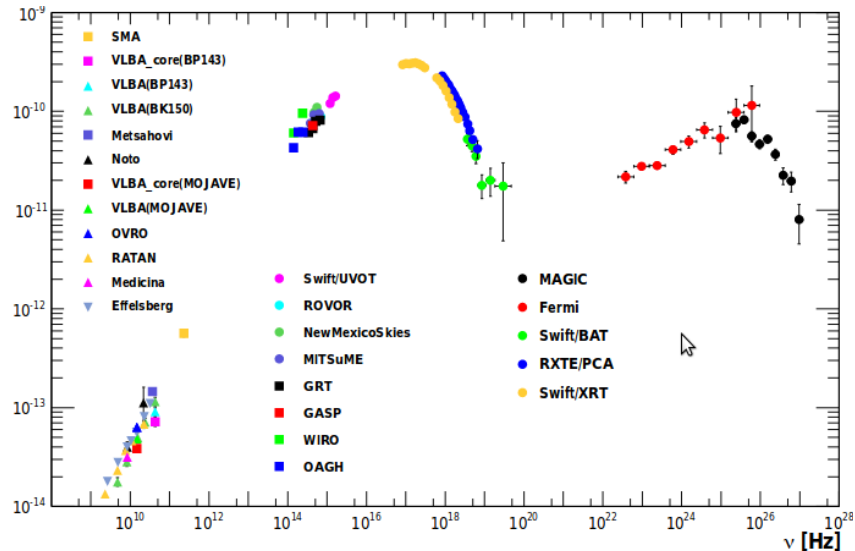


Figure 2.1: Spectral energy distribution of Mrk 421 averaged over all the observations taken during the multifrequency campaign from 2009 January 19th to 2009 June 1st [8]. The graph is a plot of the energy flux compared to the frequency. It clearly shows two peaks of energy flux. The lower frequency peak $\nu_S^{\text{peak}} > 10^{15} \text{ Hz}$ makes it a Radio-Loud blazar. IACTs, e.g. MAGIC, are used to detect γ -rays at higher energies.

The frequency ν , on the x -axis of Figure 2.1, can be related to a photon's energy by the formula

$$E = h\nu, \quad (2.2)$$

where h is the Planck constant. Notice in Figure 2.1 that there is no exposure in the regime $5 \cdot 10^{19} \text{ Hz} \lesssim \nu_S \lesssim 10^{22} \text{ Hz}$. This is not because the blazar does not emit photons in this interval, but because current detectors have a poor sensitivity at these frequencies. The interval has proven to be of critical consequence to the question of whether electrons or protons are the cause of the VHE γ -rays. Also, it would be crucial to have a good sensitivity here, if one wants to detect a lower energetic photon halo from the blazar.

2.4 EXTRAGALACTIC BACKGROUND LIGHT

There is an observed background of electromagnetic radiation, consisting of every photon emitted since the Early Universe. These photons are emitted by planets, stars, dust and AGNs integrated over all time after the decoupling of the photons. The most important parts of this background are the CMB and the EBL. The EBL consists of electromagnetic background radiation in the optical and infrared regime. Sometimes it also includes the CMB, but in this thesis, it will not. To understand how cosmic rays traverse the Universe it is important to know about the EBL. The EBL interacts with baryonic matter and other photons, and the probability of these interactions are described by the cross sections of the processes. This implies that when observing VHE γ -rays from an extragalactic source, the distance might be big enough for the γ -ray to interact with the EBL. To predict the consequences of such interactions it is crucial to know the abundance of the EBL at all wavelengths.

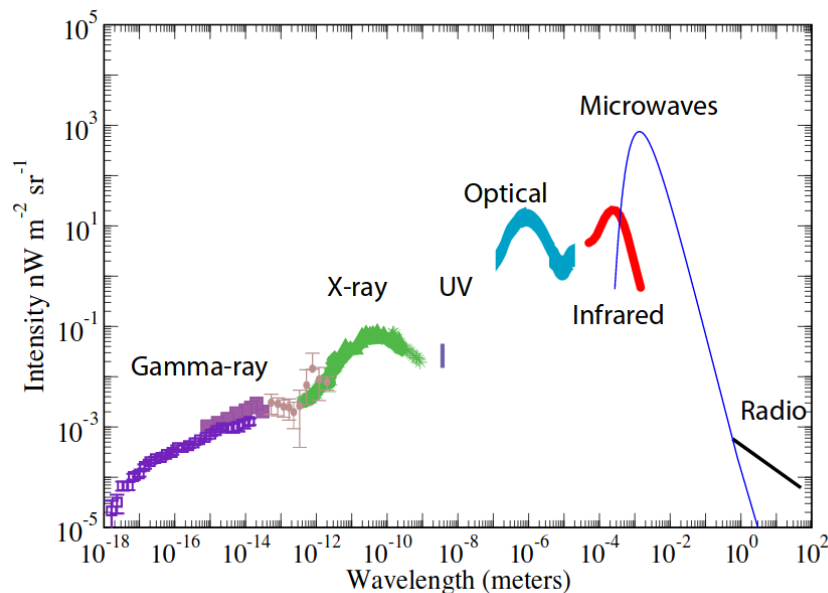


Figure 2.2: Measured intensity of all electromagnetic background radiation as a function of the wavelength. The line marked "Microwaves" is the CMB and is measured with the highest accuracy; $\sim 1\%$. The EBL consists of the radiation in the optical and infrared regime ($10^{-7} \text{ m} \leq \lambda \leq 10^{-4} \text{ m}$). The optical regime has low resolution due to the Zodiacal light foreground [9].

The wavelength of a photon on the x-axis in Figure 2.2 can be related to its energy by

$$E = h \frac{c}{\lambda}, \quad (2.3)$$

where h is the Planck constant, c is the speed of light and λ is the wavelength. The cosmic optical background (COB), $\lambda \approx 10^{-6} \text{ m}$, is the most crucial part of the EBL, considering observations of photon emission from blazars. Figure 2.2 shows a large uncertainty in the measurements of the EBL in this range, which stems from disturbance by the Zodiacal light. The Zodiacal light is photons from the Sun scattered by interplanetary dust. It is important to

measure the COB accurately, as the photons with energies of 10 GeV to 10 TeV are sensitive to interaction with the EBL in this regime.

Cosmic Microwave Background

The cosmic microwave background is all photons radiated at the decoupling of the photons in the Early Universe. The measurement of the radiation relic was one of the winning arguments in favor of the Λ CDM-model. Today, the radiation is redshifted as a consequence of the expansion of the Universe, thus resulting in radiation on the length scale of microwaves. From Figure 2.2 it is clear that the CMB is by far the most abundant background radiation. Although it is very abundant, it has little impact on current observations of cosmic rays, as the energy of a primary particle must be huge to create a sizable cross section with a CMB-photon. However, it results in an upper bound on CR energies, namely the GZK cutoff. If a proton has an energy $E \gtrsim 5 \cdot 10^{19}$ eV, it will produce pions with the CMB, thus providing an energy cutoff for CRs from extragalactic sources.

2.5 PRIMORDIAL MAGNETIC FIELD

Magnetic fields are present everywhere in the Milky Way Galaxy. The Earth has its own magnetic field, a star has its own stellar magnetic field and even a galaxy has a magnetic field. While the Earth has a magnetic field in the order ~ 0.5 G, the underlying magnetic field in a galaxy is around $1 - 10 \mu\text{G}$. This means that wherever a charged particle moves in the Galaxy, it is affected with a force from at least a μG magnetic field. Magnetic fields at astronomical scales, from solar systems up to galaxy clusters, are widely accepted to be a product of amplified weaker magnetic fields [10]. This amplification can happen through different processes, e.g. gravitational collapses. However, short distance magnetic fields can dissipate their energy into particle motion. This means that magnetic fields on the length scale of the Earth and stars have a relatively short lifetime. On the other hand, a weak magnetic field on the distance scale of the order of the distance between galaxies will not have the time or field strength to dissipate its energy into plasma motion, thus giving it a lifetime of the age of the Universe [10]. This magnetic field is called the extragalactic magnetic field because it would also reside in between galaxies.

The EGMF cannot be a product of the amplified magnetic fields described above as it exists on a too large distance scale. In addition, there are no other known sources that might be responsible for the creation of such a field, resulting in the theory of its creation in the Early Universe. The EGMF could be a primordial magnetic field, that has been affected by fields from the creation and explosion of astronomical objects, together with being diluted through the expansion of the Universe. As mentioned in section 1.1 the EGMF has a correlation length (L_c), which defines the distance scale the field can be considered coherent. The correlation length would determine whether the primordial magnetic field was made during or after the inflation process. When comparing L_c to the Hubble length (L_{Hubble}), $L_c \gg L_{\text{Hubble}}$ indicates a creation during the inflation process, while $L_c \ll L_{\text{Hubble}}$ indicates a creation after the inflation process (during phase transition). Given that the EGMF is made from a primordial

magnetic field, it is possible to set theoretical constraints on the strength of the field, e.g. $B \leq 10^{-8}$ G, or it would not be possible to form galaxies [11].

Assuming $L_c \ll L_{\text{Hubble}}$, the EGMF could either be created in the electroweak phase transition (EWPT) or the quantum chromodynamics phase transition (QCDPT). Both transitions lead to boundaries for the relation between the EGMF's correlation length L_c and strength B .

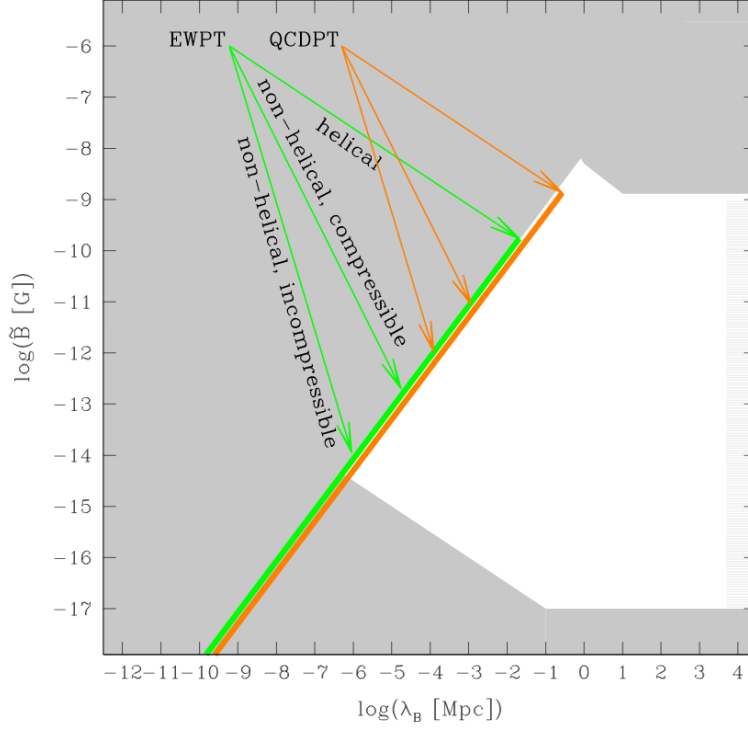


Figure 2.3: The evolution of the primordial magnetic field B (\tilde{B}) and L_c (λ_B) for helical fields and for non helical compressible and incompressible flows. Upper boundaries for EWPT and QCDPT are indicated. The plot is taken from Durrer and Neronov's review paper [10].

The theoretical boundaries of the primordial magnetic field are visualized in Figure 2.3. An EGMF that was generated during EWPT will be considered here, as CP violating processes can occur in the electroweak sector of the Standard Model of particle physics. Also, the helical case for the magnetic field is of interest, as this thesis investigates a helical EGMF. Assuming the EGMF originated in the EWPT, the radiation-dominated epoch is of significance. Thus, the primary process determining the evolution of the magnetic fields comes from magnetohydrodynamic turbulence. Durrer and Neronov [10] present a derivation of freely decaying turbulence in the radiation-dominated epoch. Following the derivation, the power spectrum for a helical magnetic field grows for $L_c > \lambda_B$. The arrangement of the green line (EWPT) in Figure 2.3 corresponds to the largest processed eddy for the magnetic field at the recombination of the Universe

$$\tilde{B} \simeq 10^{-8} \left(\frac{L_c}{1 \text{ Mpc}} \right) \text{ G}. \quad (2.4)$$

However, the correlation length of the magnetic field will evolve during the matter-dominated epoch. Also, including interactions with intergalactic medium over time, it is ambitious to

define the properties of the current EGMF as a strict line in the parameter space of \tilde{B} and λ_B . As mentioned above, the EGMF would not be amplified by interactions with intergalactic magnetic fields. Therefore, Eq. (2.4) works excellent as an upper boundary for the properties of an EGMF generated during EWPT

$$\tilde{B} \lesssim 10^{-8} \left(\frac{L_c}{1 \text{ Mpc}} \right) \text{ G}. \quad (2.5)$$

The derivations done by Durrer and Neronov are based on an order-of-magnitude analysis, which is excellent for making a qualitative understanding of the EGMF. However, the nonlinear co-evolution of the magnetic field and the plasma has been omitted, which means that Figure 2.3 should be interpreted with care. For example, many theorists use a EGMF with strength $10^{-17} \text{ G} \leq \tilde{B} \leq 10^{-13} \text{ G}$ and a correlation length $L_c \simeq 1 \text{ Mpc}$.

The EGMF would exist everywhere in the Universe but is called extragalactic in reference to "in between" galaxies, because it can only be observed in this area. To detect a magnetic field this weak, it must be observed where no other magnetic fields are present, in addition to observing it at extragalactic distances. Even though the field is very weak, charged particles would be deflected when they traverse enormous distances. That being told, the trick would be to observe these deflected particles. A theory that might prove the existence of the EGMF is that a VHE γ -ray interacts with the EBL, creating an electron-positron pair, which over vast distances gets deflected by the EGMF. After some time the charged particles interact with other photons from the EBL, producing photons with an energy and momentum detectable on Earth. If this occurs, the signal detected on Earth could be a TeV point source, with a GeV halo.

CHAPTER 3

SCATTERING ON THE EXTRAGALACTIC BACKGROUND LIGHT

The Universe is opaque to VHE γ -rays, i.e. photons at certain energies will interact with the extragalactic background at a distance scale way below the distances between galaxies. These photons will produce an electron-positron pair through pair production. The charged particles will again scatter on the background photons, and might produce more VHE γ -rays. The latter scattering process is referred to as inverse Compton (IC) scattering, as it does the opposite of Compton scattering. As many photons, electrons and positrons are involved in such a process, this is called an electromagnetic cascade. To track the theoretical behavior of such a cascade, it is crucial to know some basics of quantum field theory (QFT) and particle physics, which will be presented in section 3.1. To implement the theory into the program, some approximations have to be assumed. These approximations, together with computing efficient shortcuts and models for the EBL will be presented in section 5.1. Finally, a brief analysis of extragalactic interactions will be presented in section 3.3. Extragalactic interactions refers here to the pair production and IC scattering on the EBL, in addition to alleged deflection in the EGMF.

3.1 STANDARD MODEL OF PARTICLE PHYSICS

“Elementary particle physics addresses the question, ‘What is matter made of?’ at the most fundamental level - which is to say, on the smallest scale of size. It’s a remarkable fact that matter at the subatomic level consists of tiny chunks, with vast empty spaces in between. Even more remarkable, these tiny chunks come in a small number of different types, which is replicated in astronomical quantities to make all the ‘stuff’ around us.”
- David J. Griffiths [12]

The Standard Model of Particle Physics describes subatomic particles and how they interact. With the use of quantum field theory, it illustrates the fundamentals of quantum

electrodynamics, quantum chromodynamics and the electroweak theory. It is a truly brilliant model and has time upon time been used to predict outcomes that have proved to be shockingly accurate after experimental tests, e.g. the Higgs boson. Particle physics is used to calculate cross sections, i.e. interaction probabilities. In this report, only some of the basics of QED will be introduced. All formulae will be presented in natural units, i.e. $\hbar = c = 1$.

First, the general formalism of QED will be introduced, thereafter a brief calculation of electron-positron pair production from VHE γ -rays and EBL will be produced. Finally, the impact of IC scattering is explained.

3.1.1 Feynman Diagrams - QED

In QFT and particle physics, Feynman diagrams are used to illustrate the mathematics. A diagram consists of external lines representing the particles before and after an interaction. In addition, a diagram has connecting lines between vertices, called propagators. Each fermion line has an arrow, defined by the Stückelberg-Feynman representation of matter and antimatter, i.e. antimatter can be interpreted as matter moving backward in time. The arrow of time points rightwards on the horizontal axis, thus matter will have an arrow pointing to the right, while antimatter will point to the left. Further, all lines and vertices, together with the Feynman rules, are used to calculate the amplitude and cross section of an interaction. Calculating first the amplitude is necessary to find the final cross section. This is what the Feynman diagrams illustrate, as the calculations from a Feynman diagram result in the amplitude of the interaction. Then, the cross section of an interaction defines the probability interaction happening, thus being fundamental in particle physics.

The interaction part of the QED Lagrangian density \mathcal{L}_{int} is given by

$$\mathcal{L}_{\text{int}} = -ie\bar{\Psi}\gamma_{\mu}A^{\mu}\Psi, \quad (3.1)$$

where A^{μ} represents a photon and Ψ a fermions. Moreover, e is the coupling constant of QED, i.e. the charge of an electron, and γ_{μ} represents the gamma matrices. From Eq. (3.1) it follows that each vertex in QED must connect a photon line and two fermion lines, one with an arrow pointing towards and one away from the vertex.

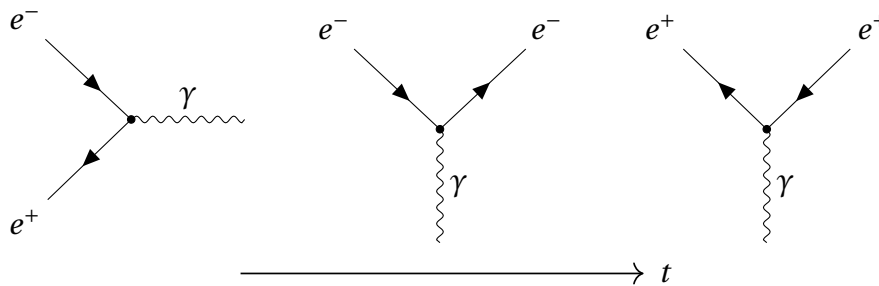
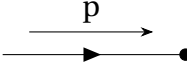
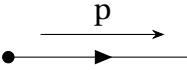
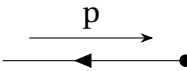
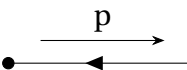
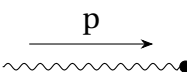
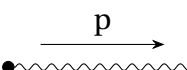
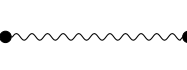
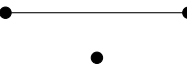


Figure 3.1: Three different QED Feynman diagrams illustrating the interpretation of Eq. (3.1) and how a vertex is illustrated. Time is defined to the right on the horizontal axis.

Figure 3.1 contains simple one-vertex diagrams to give an illustration of how one can construct QED vertices. Once this is understood, one can move on to create more intricate

diagrams. To calculate the cross section of an interaction it is important first to draw a correct Feynman diagram. The rules on how to convert Feynman Diagrams into a formula for the amplitude, are assembled to form the Feynman Rules of QED, listed in Table 3.1. A rigorous derivation of the Feynman rules can be achieved from QFT, but will not be done here as it is not within the scope of this thesis.

Table 3.1: The Feynman Rules of QED [13].

Initial-state particle:	$u(p)$	
Final-state particle:	$\bar{u}(p)$	
Initial-state antiparticle:	$\bar{v}(p)$	
Final-state antiparticle:	$v(p)$	
Initial-state photon:	$\epsilon_\mu(p)$	
Final-state photon:	$\epsilon_\mu^*(p)$	
Photon propagator:	$-\frac{ig_{\mu\nu}}{q^2}$	
Fermion propagator:	$-\frac{i(\gamma^\mu q_\mu + m)}{q^2 - m^2}$	
QED vertex:	$-ie\gamma^\mu$	

It is now possible with the help of Table 3.1 to calculate the amplitude of Feynman diagrams. First, it is necessary to assign four-momenta and polarization vectors to the fermions and photon respectively. When evaluating the Feynman diagram, start from an external fermion leg that is pointing away from a vertex, i.e. an initial antiparticle or a final particle. Then, include the vertices and follow the fermion line until it ends in an external leg pointing toward a vertex, i.e. an initial fermion or a final anti fermion. When a path is followed through, include the photon at the end, whether it is a propagator or an external leg.

3.1.2 Pair Production

Pair production is when two photons create a fermion pair, e.g. electron and a positron. The kinematics is given by

$$\gamma(k_1, \epsilon_1) + \gamma(k_2, \epsilon_2) \rightarrow e^+(k, r) + e^-(p, s), \quad (3.2)$$

where k_1 , k_2 , k and p represent the four-momentum of each particle, r and s represent the spin of the fermions, and ϵ_1 and ϵ_2 is the polarization of the photons.

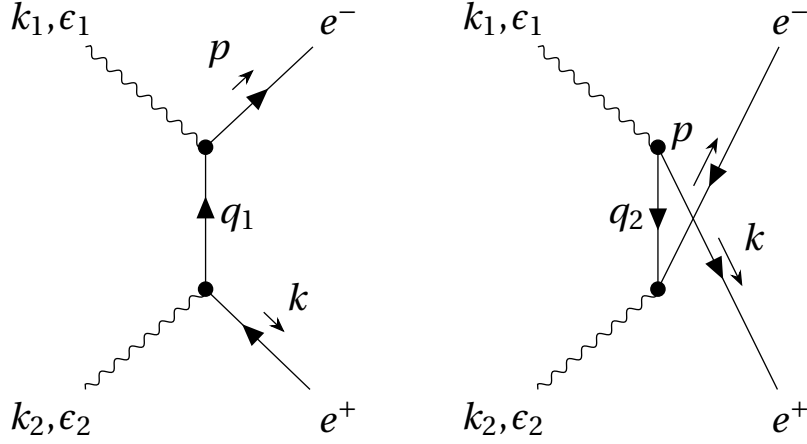


Figure 3.2: Tree level diagrams of electron/positron pair production from two photons.

There exist two tree level Feynman diagrams illustrated in Figure 3.2, corresponding to the kinematics in Eq. (3.2). Both diagrams contribute to the amplitude of the interaction. In this scenario, the total amplitude \mathcal{M} is given by

$$\mathcal{M} = \mathcal{M}_1 + \mathcal{M}_2, \quad (3.3)$$

where \mathcal{M}_1 is the contribution from the diagram on the left, and \mathcal{M}_2 from the diagram to the right. The Feynman Rules give

$$i\mathcal{M}_1 = \bar{u}(p)(-ig_e\gamma^\mu) \frac{i(q_1 + m)}{q_1^2 - m^2} (-ig_e\gamma^\nu) v(k) \epsilon_1^\mu(k_1) \epsilon_2^\nu(k_2), \quad (3.4)$$

with $q_1 = k_2 - k = p - k_1$. The second contribution can be obtained by swapping the two photons

$$i\mathcal{M}_2 = \bar{u}(p)(-ig_e\gamma^\mu) \frac{i(q_2 + m)}{q_2^2 - m^2} (-ig_e\gamma^\nu) v(k) \epsilon_1^\nu(k_1) \epsilon_2^\mu(k_2), \quad (3.5)$$

with $q_2 = k_1 - k = p - k_2$. Further, the squared amplitude is given by

$$|\mathcal{M}|^2 = |\mathcal{M}_1|^2 + |\mathcal{M}_2|^2 + 2\Re\{ \mathcal{M}_1 \mathcal{M}_2^* \}. \quad (3.6)$$

The rest of the calculation is a cumbersome process, thus only the main techniques will be mentioned. The three terms in Eq. (3.6) can be treated separately. First, the spin-average is calculated by summing over initial polarization and averaging over final spin. Then it can be shown by using the Ward Identity [14, p. 160, Eq. 5.79] together with Eq. (3.3), Eq. (3.4) and Eq. (3.5) that the completeness relation for real photons can be used. Finally, Casimirs Trick [12, p. 249-254] together with trace techniques is used. By using crossing symmetry, one can obtain the result of $|\mathcal{M}_2|^2$ from the calculations of $|\mathcal{M}_1|^2$. Thereafter, repeat the process on the third term. This will result in the same amplitude as for electron-positron pair annihilation into photons [14, p. 168, Eq. 5.105], but with different four-momentum variables

$$\langle |\mathcal{M}|^2 \rangle = 2e^4 \left[\frac{k \cdot k_1}{k \cdot k_2} + \frac{k \cdot k_2}{k \cdot k_1} + 2m^2 \left(\frac{1}{k \cdot k_2} + \frac{1}{k \cdot k_1} \right) - m^4 \left(\frac{1}{k \cdot k_2} + \frac{1}{k \cdot k_1} \right)^2 \right]. \quad (3.7)$$

From Eq. (3.7) the cross section of pair production can be found. Dwek and Krennrich [15] use

$$\sigma_{\gamma\gamma} = \frac{3\sigma_T}{16} (1 - \beta^2) \left[2\beta(\beta^2 - 2) + (3 - \beta^4) \ln \frac{1 + \beta}{1 - \beta} \right], \quad (3.8)$$

to estimate the attenuation of photons from AGNs, where σ_T is the Thomson scattering cross section and

$$\beta \equiv \sqrt{1 - \frac{\epsilon_{\text{th}}}{\epsilon}}. \quad (3.9)$$

In Eq. (3.9) ϵ is the energy of the low energetic photon, and ϵ_{th} is the threshold energy for achieving a pair production, given by

$$\epsilon_{\text{th}} = \frac{2m^2}{E_\gamma(1 - \cos\theta)}. \quad (3.10)$$

Here E_γ is the energy of the energetic γ -ray, and θ is the angle between the photons when evaluated in the laboratory frame of reference. By solving Eq. (3.9) and Eq. (3.10), and noting that $\sigma_{\gamma\gamma}$ is maximum for $\beta \simeq 0.7$ in Eq. (3.8), one finds that the energy resulting in the highest cross section E_γ^{max} is given by

$$E_\gamma^{\text{max}} = \frac{2m^2}{0.51 \cdot \epsilon(1 - \cos\theta)}. \quad (3.11)$$

In the laboratory frame the EBL will be isotropically distributed, thus θ will be arbitrary. To find the true $E_\gamma^{\text{max}}(\epsilon)$ it is necessary to integrate Eq. (3.8) over θ for each E_γ . By inserting $\epsilon \simeq 1$ eV, $m = 511$ MeV and $\theta = \pi/2$ into Eq.(3.11), one gets $E_\gamma^{\text{max}} \simeq 1$ TeV, which fits well with the calculations from other articles, e.g. [16].

3.1.3 Inverse Compton Scattering

IC scattering is the interaction where a charged particle interacts with a lower energetic photon and produces a more energetic photon. The kinematics are the same as in normal Compton scattering, but with the constraint that the energy of the final electron (k^0) is bigger than the energy of the initial electron (p^0),

$$e^-(p, s) + \gamma(k_1, \epsilon_1) \rightarrow e^-(k, r) + \gamma(k_2, \epsilon_2). \quad (3.12)$$

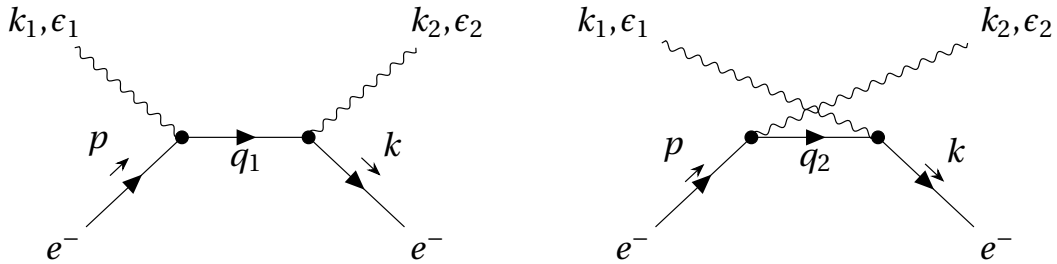


Figure 3.3: Tree level diagrams of IC scattering. The diagrams are the same as the ones for regular Compton scattering, but with the criteria $k^0 > p^0$.

By observing that the diagrams in Figure 3.3 are almost the same as in Figure 3.2, just rotated 90 degrees clockwise, one can conclude that IC scattering and pair production are related by crossing symmetry. Then it is possible to calculate the amplitude by making the following substitutions in Eq. (3.7):

$$p \rightarrow k \quad k \rightarrow -p \quad k_1 \rightarrow -k_2 \quad k_2 \rightarrow k_1.$$

The amplitude now becomes

$$\langle |\mathcal{M}|^2 \rangle = 2e^4 \left[\frac{p \cdot k_2}{p \cdot k_1} + \frac{p \cdot k_1}{p \cdot k_2} + 2m^2 \left(\frac{1}{p \cdot k_1} - \frac{1}{p \cdot k_2} \right) + m^4 \left(\frac{1}{p \cdot k_1} - \frac{1}{p \cdot k_2} \right)^2 \right]. \quad (3.13)$$

Using Eq. (3.13), it can be shown that the IC scattering cross section for high energy behavior in the center-of-momentum frame [14, p. 164, Eq. 5.96] becomes

$$\begin{aligned} \sigma_{\text{IC}} &= \frac{2\pi\alpha^2}{s} \log \frac{s}{m^2} \\ &= \frac{3m^2}{4s} \sigma_T \log \frac{s}{m^2}. \end{aligned} \quad (3.14)$$

Here α is the fine structure constant, and s is the center of mass energy squared Mandelstam variable¹, which in this case is given by $s = (p + k_1)^2$. In the center-of-momentum frame the kinematics is given by $k_1 = (\omega, 0, 0, -\omega)$ and $p = (E, 0, 0, \omega)$, where $E^2 = \omega^2 + m^2$. This gives

$$s = 2\omega^2 + m^2 + 2\sqrt{\omega^2 + m^2}\omega, \quad (3.15)$$

where ω is the energy of the photon.

3.2 MODELING OF ELECTRON-PHOTON INTERACTIONS

The routines presented in this section are also presented in the first release of the program ELMAG by Kachelrieß et al. [5]. The calculations made here will be a reproduction of the first two sections in the Chapter "*Modelling of the cascade process*". They are presented here as well, to provide a standalone presentation of the program.

Pair Production

In terms of the model in the program, it is useful to change the variable dependency of $\sigma_{\gamma\gamma}(\beta) \rightarrow \sigma_{\gamma\gamma}(s)$, where s is the center of mass energy squared Mandelstam variable. In this case, using Eq. (3.9) and Eq. (3.10) s becomes

$$s = 2 E_\gamma \epsilon (1 - \cos\theta) = \frac{4m_e^2}{1 - \beta^2}. \quad (3.16)$$

¹Described in Appendix A

Introducing the density of the EBL as a modeled function of energy E_γ and redshift z ($n_\epsilon = n_\epsilon(E_\gamma, z)$), the program can accurately simulate the rate of cascade interactions. There exist many fits to model the EBL. In this particular case the "best fit" EBL model from Kneiske and Dole [17] is used to define n_ϵ , but n_ϵ can, in general, be defined by any desired EBL-model. When knowing the EBL-density, the interaction rate between a VHE γ -ray and the density of the background photons is connected to the pair production cross section from Eq. (3.8) by

$$\begin{aligned} R_\gamma(E_\gamma, z) &= \frac{1}{2} \int_0^\infty dE n_\epsilon(E, z) \int_{-1}^1 d\mu (1 - \mu) \sigma_{\gamma\gamma}(s) \Theta(\epsilon - \epsilon_{\text{th}}) \\ &= \frac{1}{8E_\gamma^2} \int_{s_{\min}}^{s_{\max}(E_\gamma)} ds s \sigma_{\gamma\gamma}(s) I_\gamma\left(\frac{s}{4E_\gamma}, z\right). \end{aligned} \quad (3.17)$$

Here $\mu \equiv \cos\theta$ and the Heaviside step function $\Theta(\epsilon - \epsilon_{\text{th}})$ is used to implement the pair production energy threshold. The integration limits are given by the pair production threshold $s_{\min} = 4m_e^2$ and $s_{\max} = 4E_\gamma \epsilon_{\max}$, where $\epsilon_{\max} = 14$ eV is the high energy cutoff for the EBL. Also, there has been introduced an auxiliary function

$$I_\gamma(E_{\min}, z) = \int_{E_{\min}}^{\epsilon_{\max}} \frac{dE}{E^2} n_\epsilon(E, z). \quad (3.18)$$

The program will initiate a pair production according to the probability distribution of s . First, the program samples the value s logarithmically in the interval $[s_{\min}, s_{\max}]$, then the choice is accepted based on the probability proportional to s multiplied with the integrand of Eq. (3.17). For a chosen s , the energy fraction per produced secondary will be calculated by the corresponding differential cross section

$$\frac{d\sigma_{\gamma\gamma}(s, y)}{dy} \propto \frac{1}{y} \left[\frac{y^2}{1-y} + 1 - y + \frac{1-\beta^2}{1-y} - \frac{(1-\beta^2)^2}{4y(1-y)^2} \right] / [1 + 2\beta^2(1-\beta^2)], \quad (3.19)$$

giving the lowest energy secondary particle an energy fraction y , and the other an energy fraction $1 - y$.

Inverse Compton Scattering

The secondary charged particles interact steadily with background photons. To speed up the computations, the program calculates secondary photons only as a discrete interaction above the desired energy threshold $E_\gamma \geq E_{\text{th}}$. Photons emitted through IC scattering below this threshold are excluded from the continuing cascade. However, the energy loss of the continuous soft photon emission is taken into account as energy loss for the charged particle propagating without emitting $E_\gamma \geq E_{\text{th}}$. The interaction rate for IC scattering can be calculated in a similar manner as for pair production

$$\begin{aligned} R_e(E_e, z) &= \frac{1}{2} \int_0^\infty dE n_\gamma(E, z) \int_{-1}^1 d\mu (1 - \beta\mu) \sigma_{\text{IC}}(s, \epsilon) \Theta(s - s_{\min}(\epsilon)) \\ &= \frac{1}{8\beta E^2} \int_{s_{\min}(\epsilon)}^{s_{\max}(E_e)} ds (s - m_e^2) \sigma_{\text{IC}}(s, \epsilon) I_\gamma\left(\frac{s - m_e^2}{2E_e(1 + \beta)}, z\right). \end{aligned} \quad (3.20)$$

Here ϵ is given by the relation $\epsilon = E_{\text{th}}/E_\gamma$, $s = m_e^2 + 2E_\gamma E(1 - \beta\mu)$ and E_e is the initial energy of the charged particle. The integration limits are defined as $s_{\text{min}}(\epsilon) = m_e^2/(1 - \epsilon)$ and $s_{\text{max}} = m_e^2 + 2E_\gamma \epsilon_{\text{max}}(1 + \beta)$, where $\epsilon_{\text{max}} \simeq 14$ eV still is the high energy cutoff of the EBL. The auxiliary function I_γ is still defined by Eq. (3.18). The Compton scattering cross section from Eq. (3.14) integrated above the threshold ϵ becomes

$$\begin{aligned} \sigma_{\text{IC}}(s, \epsilon) &= \frac{3}{4} \sigma_T y_{\text{min}} \frac{y_{\text{max}} - y_{\text{min}}}{1 - y_{\text{min}}} \left[\frac{\ln(y_{\text{max}}/y_{\text{min}})}{y_{\text{max}} - y_{\text{min}}} \left(1 - \frac{4y_{\text{min}}(1 + y_{\text{min}})}{(1 - y_{\text{min}})^2} \right) \right. \\ &\quad \left. + \frac{4(y_{\text{min}}/y_{\text{max}} + y_{\text{min}})}{(1 - y_{\text{min}})^2} + \frac{y_{\text{max}} + y_{\text{min}}}{2} \right], \end{aligned} \quad (3.21)$$

where $y_{\text{min}} = m_e^2/s$ and $y_{\text{max}} = 1 - \epsilon$. These values also serve as the minimal and maximal values for the secondary charged particle. This interaction rate is in the discrete case of IC scattering, while it is also essential to account for the energy loss from emittance of the photons with energy $E_\gamma < E_{\text{th}}$. Consequently, this is justified by the formula for energy loss per unit distance for $E_\gamma < E_{\text{th}}$

$$\begin{aligned} \frac{dE_{\text{IC/th}}}{dx}(s, \epsilon) &= \frac{3}{4} \sigma_T y_{\text{min}} \frac{1 - y_{\text{max}}}{1 - y_{\text{min}}} \left[\left(\frac{\ln(1/y_{\text{max}})}{1 - y_{\text{max}}} - 1 \right) \left(1 - \frac{4y_{\text{min}}(1 + 2y_{\text{min}})}{(1 - y_{\text{min}})^2} \right) \right. \\ &\quad \left. + \frac{1}{6} (1 - y_{\text{max}}) (1 + 2y_{\text{max}}) \frac{2y_{\text{min}}(1 + 2y_{\text{min}}/y_{\text{max}})(1 - y_{\text{max}})}{(1 - y_{\text{min}})^2} \right]. \end{aligned} \quad (3.22)$$

In the same manner as for the case of pair production, the center of mass energy squared Mandelstam variable s is sampled logarithmically in the range $[s_{\text{min}}(\epsilon), s_{\text{max}}(E_e)]$. The probability of acceptance is then s multiplied with the integrand of Eq. (3.21). For the given s , the energy fraction of the secondary particles are sampled by the differential cross section

$$\frac{d\sigma_{\text{IC}}(s, y)}{dy} \propto \frac{1}{y} \left[\frac{1 + y^2}{2} - \frac{2y_{\text{min}}(y - y_{\text{min}})(1 - y)}{y(1 - y_{\text{min}})^2} \right], \quad (3.23)$$

where y is the energy fraction obtained by the charged particle, which leaves the energy fraction $1 - y$ for the IC scattered photon. It is worth noting that the program will discard the charged particle or the photon, if $yE_e < E_{\text{th}}$ or $(y - 1)E_e < E_{\text{th}}$ respectively.

3.3 ANALYSIS OF EXTRAGALACTIC INTERACTIONS

By using Eq. (3.8) and Eq. (3.14), it is possible to estimate at what energies the Universe is opaque to the propagation of γ -rays. In Figure 2.1 the most energetic particle that has been observed is approximately of the frequency $\nu = 5 \cdot 10^{26}$ Hz, which by Eq. (2.2) gives an energy of ~ 2 TeV. Photons of this energy can produce electron-positron pairs through pair production with photons from the EBL. From Figure 2.2 it is clear that the abundance of the EBL shows two distinct peaks, except from the CMB. One peak at $\lambda_1 \simeq 10^{-6}$ m in the optical regime and the other at $\lambda_2 \simeq 10^{-4}$ m in the infrared regime, which by using Eq. (2.3) results in $\epsilon_{\text{EBL1}} = 1.24$ eV and $\epsilon_{\text{EBL2}} = 1.24 \cdot 10^{-2}$ eV.

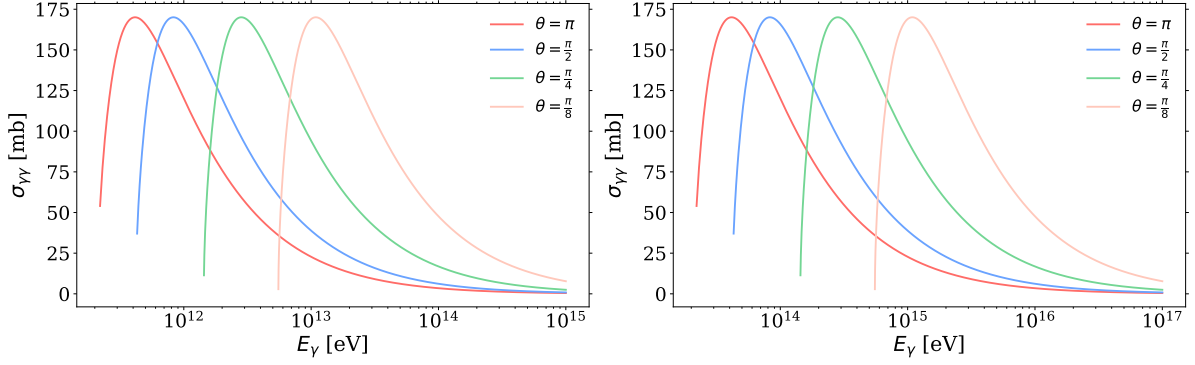


Figure 3.4: The pair production cross section of a VHE γ -ray interacting with the EBL. Graphs have been made by using (3.8). The cross section is a function of the energy of the VHE γ -ray. The graph plots for different angles. On the left is the cross section for interaction with the Cosmic Optical Background, while on the right for the Cosmic Infrared Background. θ is the angle between the momentum directions of the γ -ray and the photon from the EBL. Each line has a sharp cutoff on the left, this is due to the necessary energy and momentum conservation in a pair production ($\beta^2 > 0$ in (3.9)).

Figure 3.4 shows cross section curves as a function of the VHE γ -ray, with each line representing an angle between the momentum directions of the VHE γ -ray and the photon from the EBL. The panel on the left is for γ -ray interaction with ϵ_{EBL1} , and the one on the right for interactions with ϵ_{EBL2} . The cross sections $\sigma_{\gamma\gamma}$ are represented in units of mb ($1 \text{ mb} \equiv 10^{-27} \text{ cm}^2$). Figure 3.4 indicates that $\lim_{\theta \rightarrow 0} E_{\gamma}^{\text{max}} = \infty$, which is consistent with Eq. (3.11). When looking at photons interacting with an angle $\theta > \pi/4$, it is clear that their maximum cross section is in the TeV area. Due to the uniform distribution of the EBL as a function of θ , it follows that approximately 3/4 of the EBL at wavelength $\lambda = 10^{-6} \text{ m}$ are sensitive to pair production with TeV γ -rays. The EBL in the infrared regime is sensitive to photons two orders of magnitude higher. The CMB is the most abundant background radiation, and has a higher intensity than the optical and infrared radiation, down to $\lambda \simeq 10^{-2} \text{ m}$. Extrapolating the results from Figure 3.4 imply that γ -rays with energy $E_{\gamma} \simeq 10^{16} \text{ eV}$ are sensitive to pair production with the CMB at this wavelength.

Having a relatively abundant EBL for wavelengths $10^{-6} \text{ m} \leq \lambda \leq 10^{-2} \text{ m}$ means that the Universe is opaque to photons with the energy $10^{12} \text{ eV} \leq E_{\gamma} \leq 10^{16} \text{ eV}$. It is also worth noting that the abundance of cosmic rays also photons follows a strict power law for the flux as a function of energy $\mathcal{F} \propto E^{-\alpha}$, where $2 < \alpha < 3$ depending on the energy regime. Nevertheless, this means that γ -rays with energy $E_{\gamma} > 10^{16} \text{ eV}$ are extremely rare. Then, a somewhat simplified analysis implies that the Universe is opaque to the propagation of γ -rays with energy $E_{\gamma} \gtrsim 10^{12} \text{ eV}$. The attenuation length of VHE γ -rays (D_{γ}) can be approximated by the same formula used by Neronov and Vovk [18]

$$D_{\gamma} \simeq 80 (E_{\gamma}/10 \text{ TeV})^{-1} \text{ Mpc}. \quad (3.24)$$

When the VHE γ -ray and EBL makes an electron-positron pair, the charged particles will be heavily boosted in the momentum direction of the γ -ray, i.e. having the same direction as

the γ -ray. The energetic electrons and positrons can again interact with the EBL through IC scattering, i.e. that a lower energetic photon is absorbed while a higher energetic photon is emitted by the electron or positron. By this process, the charged particles produce a shower of HE γ -rays, which is in the energy range 100 GeV [18]. From Eq. (3.14) and Eq. (3.15) it is clear that in the high energy limit, i.e. $\omega \gg m$, the cross section becomes smaller as the photon energy becomes higher, thus providing an energy suppression for IC energized photons.

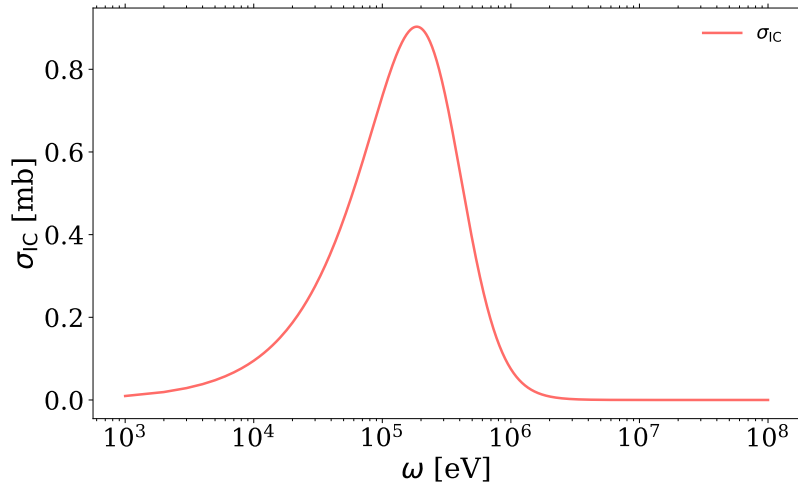


Figure 3.5: The cross section of IC scattering in the center-of-momentum frame. ω is the momentum of both the initial photon and initial fermion. In the case of the photon it is the energy, and is plotted as an energy, hence the unit eV. The graph is produced from Eq. (3.14) as a function of ω given in Eq. (3.15).

Figure 3.5 shows a peak at $\omega \approx 10^5$ eV which is an energy much higher than that of the most abundant EBL. On the other hand, remember that (3.14), and also Figure 3.5, refers to an interaction happening in the center-of-momentum frame. When a VHE electron and a background photon interacts in the center-of-momentum frame, the frame will be heavily boosted in the direction of the electron momentum, thus blue-shifting the background photon. The energy of the photon in the new frame of reference might reside in the regime where the cross section peaks. This is a calculation that could be interesting to do but will be omitted for now, due to the already given result from Neronov and Vovk [18]. Neronov and Vovk also state that leptons lose energy to IC scattering on a distance scale

$$D_e \approx 3.24 \cdot 10^{-2} (E_e/10\text{TeV})^{-1} \text{ Mpc}, \quad (3.25)$$

i.e. a 1 TeV electron has an average travel length of 10^{24} cm ≈ 0.324 Mpc before it interacts via IC scattering. In Eq. (3.25) E_e is the energy of the parent charged particle. It is clear from Eq. (3.24) and Eq. (3.25) that the attenuation length of VHE charged particles are much shorter than for γ -rays.

As briefly mentioned in section 2.5, a result proving the existence of an EGMF could be the detection of a TeV point source with a GeV halo. Considering Eq. (3.24) and Eq. (3.25), a point source could produce a cascade where the lower energetic charged particles first obtain more

deflection by the Lorentz force, and secondly have a longer traversed length in the magnetic field, hence being even more deflected. Lower energetic particles produces lower energetic IC scattered photons. Thus, the pattern should have a sharp peak of VHE γ -rays in the middle, with a halo where the energy rapidly decreases with the distance to the peak (point source). The relation in Eq. (3.25) provides a lower energy bound for the charged particles liable for the halo because lower energetic particles have a mean free path larger than the distance to Earth. In the case of Mrk 421, $E_e = 1$ GeV would be a lower bound because an electron with this energy would have a mean free path $D_e \simeq 320$ Mpc, which is around three times longer than the distance between Mrk 421 and Earth. The energetic electrons and positrons will also lose energy in a magnetic field through synchrotron radiation, which will be derived in section 5.1.

The three parameters of the EGMF considered in this thesis are the correlation length, field strength and polarization. Different configurations of these parameters can result in similar halos from the point source, e.g. a very weak uniform magnetic field could produce similar results as a very turbulent stronger magnetic field. In the uniform field, the charged particles would be slightly deflected in the same direction until IC scattering occurs. In the case of a turbulent field, the fermions would undergo a stronger deflection, but in different directions of each correlation length, thus resembling a random walk. With the correct relative strengths and correlation length, both scenarios would produce results that have the same mean deflection angle, but probably different variances. At the same time, other properties could also produce a similar pattern, e.g. a magnetic field with strength and correlation length respectively in between those mentioned above. This means that to determine the parameters of the EGMF one would need high sensitivity in the observations, in addition to good statistics, preferably of many different sources.

A definite detection of the EGMF would be excellent, but still not a proof of its formation. The objective is to determine whether it is formed as a helix, which could prove CP-violation in the Early Universe. If a correlation length defines the length where the magnetic field can be slowly varying, then the length scale of where the EGMF can be considered a helix must be many times, possibly several orders, bigger. Therefore, the next question would be; on what length scales can the EGMF be considered a helix? Probably even more statistics would be necessary to find proof of these helices. Both more statistics and more accurate theoretical predictions are needed, thus the further development of ELMAG is necessary.

CHAPTER 4

MODELING AND DEFLECTION IN THE EXTRAGALACTIC MAGNETIC FIELD

The EGMF was described in subsection 2.5. One hypothesis is that the EGMF is turbulent on a large distance scale. However, in terms of some model, this distance scale can be arbitrary for now, because the goal is to create such a turbulent magnetic field for any normalized distance. In the Friedmann-Robertson-Walker universe, the Universe is isotropic, which means that it is reasonable to assume the EGMF also is isotropic. Knowing the correlation length of the magnetic field and the root mean square value of its strength, one can create a three-dimensional turbulent isotropic magnetic field, resembling the real EGMF. In practice, this turbulent EGMF serves as a continuous version of a cubic cell spaced homogeneous magnetic field with a randomized vector orientation. The model for generating such a magnetic field will be presented in section 4.1.

Still letting the distance scale of turbulence be arbitrary, the magnetic field would, by the Lorentz force, invoke deflections on charged particles that are not analytically solvable. This means a precise numerical routine is necessary. Due to the field's turbulence and unpredictability, it could be strong in some regions, and weak in other regions. Strong regions would require a smaller stepsize, while weak regions would allow for a bigger step size, for the equivalent numerical resolution. Solving such a differential equation, evolving erratic in space, is the perfect objective of a full-fledged adaptive stepsize solver. This numerical routine will be presented in section 4.2.

4.1 GENERATION OF A TURBULENT MAGNETIC FIELD

Assuming the EGMF is helical and on average isotropic in space, the field can be modeled based on the computational algorithm described by Jakopii et al. [19]. Also, the correlation length of such an EGMF follows the theory from Harari et al. [20]. In general, an arbitrary

turbulent magnetic field can be described by a superposition of Fourier modes

$$B_j(\mathbf{r}) = \int \frac{d^3k}{(2\pi)^3} B_j(\mathbf{k}) e^{i(\mathbf{k}\mathbf{r} + \phi_j(\mathbf{k}))}, \quad (4.1)$$

having a random Gaussian profile with zero mean. Here \mathbf{k} is the wave vector of each mode j , \mathbf{r} is the position in Euclidean space and $\phi_j(\mathbf{k})$ are the random phases. For the turbulent magnetic field to resemble an isotropic EGMF, it requires an isotropic and homogeneous distribution of the turbulence. The computational way of making it so, is by summing over all Fourier modes, with each mode being logarithmically spaced in from \mathbf{k}_{\min} to \mathbf{k}_{\max} , oriented in a random three-dimensional direction. The power spectrum from \mathbf{k}_{\min} to \mathbf{k}_{\max} is defined by the spectral index γ , letting the energy distribution of the magnetic field follow $E(k_j) \propto B^2(k_j) \propto k^{-\gamma}$. The computational way of generating a turbulent magnetic field following Eq. (4.1) is presented by Jakoppi et al., which in Euclidean space becomes

$$\mathbf{B}(\mathbf{r}) = \sum_{j=1}^{n_k} B(k_j) [\cos \alpha_{k_j} \hat{\mathbf{e}}_{x'} \pm i \sin \alpha_{k_j} \hat{\mathbf{e}}_{y'}] e^{i(k_j \hat{\mathbf{e}}_{z'} + \beta_j)}, \quad (4.2)$$

where the term in square brackets defines the mode's polarization vector, the exponential term defines the field in $\hat{\mathbf{e}}_{z'}$ -direction with phase shift β_j , and n_k are the total number of modes for generating the superposition of the magnetic field. $B(k_j)$ is the amplitude for mode j and is given by the root mean square value (B_{rms}) of the field strength

$$B^2(k_j) = B_{\text{rms}}^2 k_j^{-\gamma} \frac{(\gamma - 1) k_{\min}^{\gamma-1}}{1 - (k_{\min}/k_{\max})^{\gamma-1}}, \quad (4.3)$$

which in turn compiles the magnetic field to normalize according to $\langle |\mathbf{B}(\mathbf{x})|^2 \rangle = B_{\text{rms}}^2$. Note that also here it is required that $k_{\min} \leq k_j \leq k_{\max}$. Each mode in Eq. (4.2) is multiplied with the rotation matrix

$$R(\theta_j, \phi_j) = \begin{bmatrix} \cos \theta_j \cos \phi_j & \cos \theta_j \sin \phi_j & -\sin \theta_j \\ -\sin \phi_j & \cos \phi_j & 0 \\ \sin \theta_j \cos \phi_j & \sin \theta_j \sin \phi_j & \cos \theta_j \end{bmatrix}, \quad (4.4)$$

to make the magnetic field random in the three-dimensional unprimed coordinate space ($\mathbf{r}_{3\text{D}}' = R(\theta, \phi) \mathbf{r}_{3\text{D}}$).

For every mode j , the values α_{k_j} , β_j , θ_j and ϕ_j are given by a uniform randomization

$$\begin{aligned} 0 &\leq \alpha_{k_j} \leq 2\pi, \\ 0 &\leq \beta_{k_j} \leq 2\pi, \\ 0 &\leq \phi_j \leq 2\pi, \\ 0 &\leq \theta_j \leq \pi, \end{aligned}$$

in addition to the random \pm sign in Eq. 4.2. The \pm sign decides the helicity (h) of the magnetic field. $0 \leq h \leq 1$, with $h = 1$ when the sign is $+$ in all cases, giving a completely right-handed polarization of the turbulent magnetic field. If $h = 0$, the sign is $-$ in all cases and the turbulent magnetic field will be completely left-handed polarized.

When n_k is sufficiently large, the magnetic field will be isotropic. Assuming the magnetic field is now isotropic, the correlation length L_c of a turbulent magnetic field as defined above becomes

$$L_c = \frac{L_{\max}}{2} \frac{\gamma - 1}{\gamma} \frac{1 - (L_{\min}/L_{\max})^\gamma}{1 - (L_{\min}/L_{\max})^{\gamma-1}}, \quad (4.5)$$

with $L_{\min} = 2\pi/k_{\max}$ and $L_{\max} = 2\pi/k_{\min}$ [20].

The turbulent magnetic field is generated by specifying the desired root mean field strength B_{rms} and the desired power spectrum from k_{\min} to k_{\max} with spectral index γ . The power spectrum of the magnetic field provides the specification of the field's correlation length L_c by Eq. (4.5). At every point \mathbf{r} the magnetic field will be generated by Eq. (4.2), based on the initialized random parameters α_{k_j} , β_{k_j} , ϕ_j , θ_j and the \pm sign for all modes $j \in [0, n_k]$. The helicity of the magnetic field is of great interest when considering the fundamental parameters of the EGMF, because it might imply CP violation in the Early Universe.

It should also be emphasized that the turbulent magnetic field described in this section models a field comparable to the sum of magnetohydrodynamic eddies from the radiation-dominant epoch, described by Durrer and Neronov [10].

4.2 DEFLECTION IN A TURBULENT MAGNETIC FIELD

When considering the deflection of charged particles in magnetic fields, the Lorentz force equation is fundamental

$$\frac{d\mathbf{p}}{dt} = q (\mathbf{E} + \mathbf{v} \times \mathbf{B}), \quad (4.6)$$

where q is the charge of the propagating particle, with velocity \mathbf{v} in the electric field \mathbf{E} and magnetic field \mathbf{B} . In the case of this thesis, there is no electric field ($\mathbf{E} = \mathbf{0}$). However, the particle is highly relativistic, thus Eq. (4.6) must be generalized to hold in the relativistic case. The momentum of a relativistic particle is

$$\mathbf{p} = \gamma_L m \mathbf{v}, \quad (4.7)$$

where m is the mass of the particle and γ_L is the Lorentz factor $\gamma_L \equiv 1/\sqrt{1 - (v/c)^2}$, with c being the speed of light in vacuum. Due to no electric field, thus conservation of kinetic energy, the acceleration \mathbf{a} of the particle originates solely from the magnetic field. Realizing that $m\mathbf{a} = \frac{d\mathbf{p}}{dt}$, one can obtain the equation for acceleration by combining Eq. (4.6) and Eq. (4.7)

$$\mathbf{a} = \frac{\pm e}{3.336 \cdot 10^{16}} \frac{[\text{eV}]}{E} \frac{\boldsymbol{\beta} \times \mathbf{B}}{[\text{G}]} \text{ m/s}^2. \quad (4.8)$$

Here E is the energy of the particle expressed in units of [eV], \mathbf{B} is in units of [G], and $\boldsymbol{\beta} \equiv \mathbf{v}/c$ is the unitless relative velocity to the speed of light in vacuum (c). The value e is now -1 for an electron or +1 for a positron. To generalize Eq. (4.8) further, one could also multiply by a factor Z , defining how many elementary charges a particle consists of. However, in this thesis, only electrons and positrons are of interest, thus $Z = 1$. Also, the Larmor radius (R_g) becomes

$$R_g = 1.081 \cdot 10^{-3} \beta_\perp \frac{E}{10^{18} [\text{eV}]} \frac{[\text{G}]}{B} \text{ pc}, \quad (4.9)$$

with β_{\perp} being the relative velocity perpendicular to the magnetic field.

In both pair production and IC scattering, the produced particles have a momentum distribution. However, above a certain energy threshold, the momentum distribution will be heavily forward peaked, so that one can assume the secondary particles inherits the exact velocity from the parent particle. In turn, energies below this threshold will have a Larmor radius many orders of magnitude beneath the traveled distance and possibly the correlation length of the EGMF. Having $R_g < L_c$ can result in a contained particle, much like the magnetic bottle effect, hence the program will discard such a particle. This means that all particles of interest for the program have a heavily forward peaked orientation vector, which in turn means that the deflection does not arise from the scattering processes, but develops from the Lorentz force on charged particles in the turbulent magnetic field.

When a charged particle undergoes deflection in a turbulent magnetic field, the total deflection angle for propagated distance D can be approximated by an analytic function. In the case of propagation through the EGMF, the relevant case will be in the limit $D \gg L_c$. Due to the turbulence of the magnetic field, the charged particle will now undergo deflection described by diffusion in angle, i.e. a three-dimensional random walk in D for each step resembling a small deflection at length scale L_c . In many previous papers, e.g. the paper from Elyiv et al. [21], it is frequent to model the turbulent EGMF with constant strength and a random three-dimensional orientation, spaced in cubic cells with sides equal to the correlation length L_c . In such a turbulent field, the analytic deflection angle for $D \gg L_c$ becomes

$$\Theta \simeq \frac{\sqrt{DL_c}}{R_g}, \quad (4.10)$$

in units of radians [22]. However, in the case of this report, a continuous turbulent magnetic field is used, and Eq. (4.10) must be corrected by a factor $\sqrt{2/9}$. This can be tested by cross-referencing with the equation used by Miralda-Escudé and Waxman [23] for deflections in a turbulent intergalactic magnetic field

$$\Theta \simeq 0.025^{\circ} \sqrt{\frac{D}{L_c}} \frac{L_c}{10 \text{ Mpc}} \frac{B_{\text{rms}}}{10^{-11} \text{ [G]}} \frac{10^{20} \text{ [eV]}}{E}, \quad (4.11)$$

where E is the energy of the particle. Miralda-Escudé and Waxman's theory holds well enough in this case for extragalactic magnetic fields as well, considering both fields are generated by continuous turbulence. Inserting Eq. (4.9) into Eq. (4.11) results in a corrected version of Eq. (4.10)

$$\Theta \simeq 27.3^{\circ} \frac{\sqrt{DL_c}}{R_g}. \quad (4.12)$$

It is straight forward to check that Eq. (4.10) and Eq. (4.12) give approximately the same result when accounting for the correction factor and radians \rightarrow degrees. It is also worth noting that in the case of $D \ll L_c$, the deflection angle is approximated by

$$\Theta \simeq 27.3^{\circ} \frac{D}{R_g}, \quad (4.13)$$

which can be derived from Eq. (4.9).

The turbulent magnetic field is in general slowly varying on the scale of its correlation length. However, the magnetic field will be unpredictable on scales larger than the correlation length, e.g. a weak and uninteresting part of the field might extend over several correlation lengths, or only extend over one correlation length. Due to the turbulence and unpredictability of the magnetic field, a full-fledged adaptive stepsize solver for the Lorentz force differential equation is a good fit. The adaptive stepsize routine is based on the embedded Runge-Kutta formulae from Fehlberg, corrected with the Cash-Karp parameters for more efficient computing time [24]. The numerical solver will automatically vary its stepsize according to the magnetic field's turbulence and relative strength. In this way, the solver will be faster in the uninteresting parts of the EGMF and exact in the more challenging parts of the EGMF.

The routines used to solve the Lorentz force differential equations are taken from "*Numerical recipes*" [24, ch. 16.2] and complete a full-fledged ordinary differential equation (ODE) solver with adaptive stepsize control using a fifth and fourth order Runge-Kutta method. In general, the solver works as a standalone program, with calls to only one external routine, which is specific for the differential equation needed to be solved. In this case, the external routine uses Eq. (4.8) to find the acceleration of the particle at each step in the solver. The solver consists of three routines: one that controls the input/outputs, one that controls the current and next stepsize in the solver and one that solves the differential equation through a call to the external function. Also, the latter routine uses the Cash-Karp parameters to both solve the ODE and estimate the local truncation error by using a fifth and fourth order embedded Runge-Kutta method. The second routine then checks if the local truncation error is smaller than the desired threshold. If not, it estimates a new smaller stepsize for the solver to retry, until the solver manages to solve the path according to the desired error threshold. The second routine will then output to the first routine at what stepsize it was able to solve the path and an estimated next stepsize. This way, the stepsize will get smaller when the desired threshold error is surpassed, and the stepsize increases when the estimated error is much lower than the threshold. The first routine will then advance to the next step with an initial stepsize equal to the estimation from the previous step. This loop goes on until the particle reaches the propagation length, or the maximum number of steps has been reached, which can be the case when $B_{\text{rms}} \geq 10^{-10}$ G. The first routine of the numerical solver would output to the program if the maximum number of steps were reached, which will make the program discard the associated particle.

The solver requires an initial stepsize, which is set to be $L_c/10^3$ to make sure the solver does not converge to a stepsize too big to notice the actual turbulence for both the fifth and fourth order Runge-Kutta method. There is also a minimum stepsize. Although it could in practice be zero, it is set to $L_c/10^8$ to avoid diverging to an infinitely small stepsize, thus making a faster decision to discard an uninteresting particle. Besides, a very small stepsize would lead to an unnecessary precise calculation being very time intensive. The solver is provided with a maximum number of steps, which has been set to 100 000. The maximum number of steps could be increased further if it is desirable to calculate for lower energies or a stronger magnetic field. However, one should be careful with increasing it too much, as

there is a danger of using a substantial amount of computing time on uninteresting particles, e.g. particles trapped inside a magnetic bottle. If the solver reaches the maximum number of steps, it will discard the particle. The maximum number of steps has been increased to be able to solve stronger and more turbulent fields. The last parameter that needs to be specified is the local truncation error threshold ε . A too big ε would lead to imprecise numerical results of the ODE, while a too small ε would be very computationally intensive. The ε depends on the total traveled distance within the magnetic field and the deflection per length, i.e. $\varepsilon \rightarrow \varepsilon(D, R_g)$.

The desired value of ε has been found by simulating deflection in a turbulent magnetic field with particles of constant energy and no scattering. First, initializing a turbulent isotropic magnetic field - as described in section 4.1 - with correlation length L_c . Then, assigning a propagation length D and a Larmor radius R_g as a function of L_c . Before making an empirical suggestion for the value of ε , it is necessary to test if the numerical solver works as expected in comparison to Eq. (4.12). This has been done using $\varepsilon = 10^{-7}$, which is a stringent truncation error threshold. Different values of the spectral index γ of the magnetic field from Eq. (4.3) have been tested. The most important values of the spectral index are the so-called Kolmogorov turbulence, Kraichnan turbulence, and Bohm turbulence, respectively referring to the spectral indices $\gamma = 5/3$, $\gamma = 3/2$ and $\gamma = 1$. Table 4.1 summarizes the correlation length for the three scenarios of the power spectrum for the turbulent magnetic field.

Table 4.1: The table shows three different γ -values for the spectral index in the turbulent magnetic field. By Eq. (4.5) the table gives the correlation lengths in the limit $L_{\max} \gg L_{\min}$.

Name	γ	$L_{\max} \gg L_{\min}$
Kolmogorov	5/3	$L_c = L_{\max}/5$
Kraichnan	3/2	$L_c = L_{\max}/6$
Bohm	1	$L_c = L_{\min}$

First, only magnetic fields with no helicity, i.e. $h = 1/2$ were tested. All simulations are presented as the root mean square value of the same particle in 100 different magnetic fields, with the respective error bar.

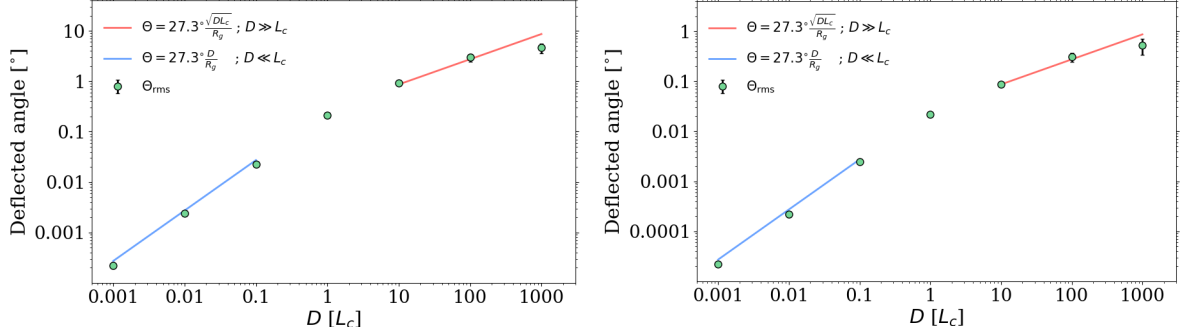
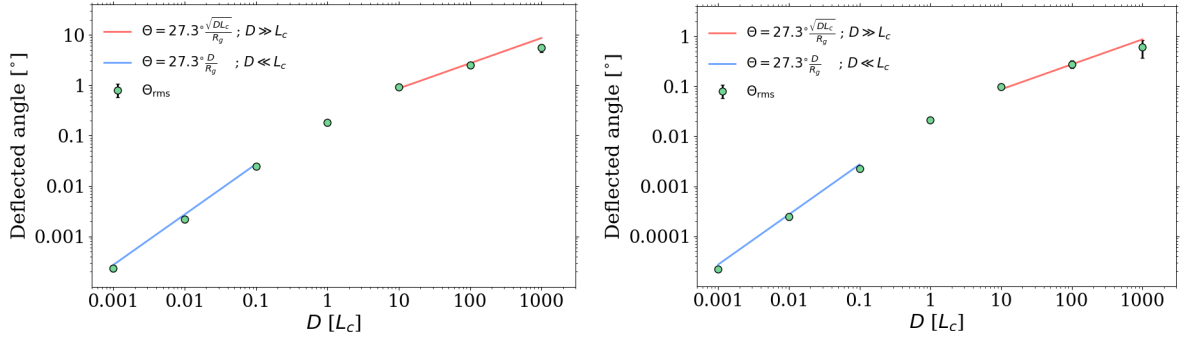
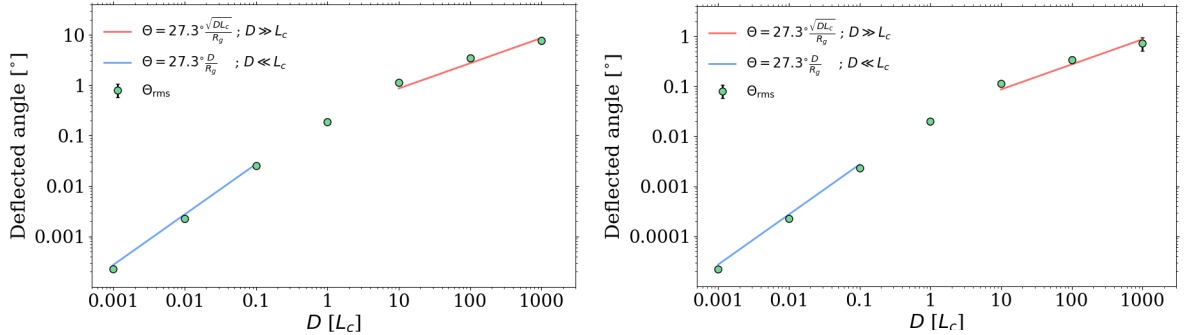

 Deflection angle in a Kolmogorov turbulent magnetic field ($\gamma = 5/3$).

 Deflection angle in a Kraichnan turbulent magnetic field ($\gamma = 3/2$).

 Deflection angle in a Bohm turbulent magnetic field ($\gamma = 1$).

Figure 4.1: Simulated deflected angles in turbulent magnetic fields with different spectral indices, as a function of propagated distance D . The panels on the left are for a Larmor radius $R_g = 100 L_c$, and the ones on the right are for $R_g = 1000 L_c$. The red and blue lines are the analytic functions for the expected deflection angle, respectively Eq. (4.12) and Eq. (4.13).

Figure 4.1 presents deflection simulations in Kolmogorov, Kraichnan and Bohm turbulence with a Larmor radius $R_g = 100 L_c$ (panels on the left) and $R_g = 1000 L_c$ (panels on the right). The green data points are the simulated results, while the red and blue lines are the analytic functions from Eq. (4.12) and Eq. (4.13). For testing purposes, the truncation error threshold is here set to $\varepsilon = 10^{-7}$ to make sure the deflection calculations are accurate. The simulations are overall in good agreement with the expected deflection, with just a few

minor deviations at large propagated distances D . The error bars seem to be bigger for larger D , which makes sense considering $D \gg L_c$ resembles a random walk, resulting in a bigger variance for the total deflected angle. For simulations of $D = 1000 L_c$, the panels on the right seem to have a slightly better agreement with the analytic expectation than the ones on the left. This is due to the fact that the Larmor radius is bigger than in the panels on the left. Then, the expected deflection angle is $\Theta \simeq 1^\circ$ (instead of $\Theta \simeq 10^\circ$) which holds much better for the small angle approximation. No polarization of the magnetic field have been used, i.e. $h = 1/2$. The deflection formulae should also hold for turbulent fields with polarization.

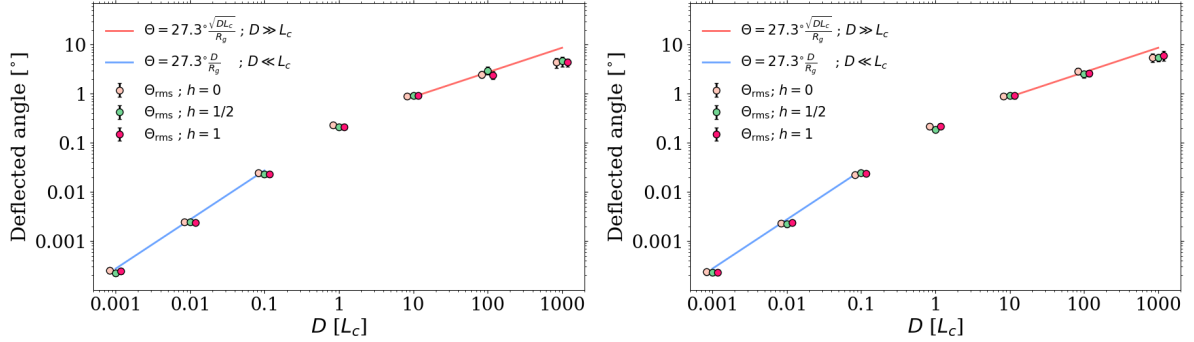


Figure 4.2: Plots including helicity of the turbulent magnetic fields. Both plots are with a Larmor radius $R_g = 100 L_c$. The left panel is for Kolmogorov turbulence, and the right is for Kraichnan turbulence.

Figure 4.2 shows that the analytic formulae also hold for right-handed and left-handed polarization of the turbulent magnetic field ($h = 1$ and $h = 0$ respectively). Note that h could have any value from zero to one, but is here only tested in the limits of a fully polarized fields.

It is crucial to decide a reasonable truncation error threshold for the solver. Too big ε might result in wrong accumulated deflection angles, while a too small ε will be very inefficient. When deciding the value of ε , the analysis is done for $D \gg L_c$ because this is the critical area for the solver to be precise. Various values of ε have been tested in the same turbulent magnetic fields

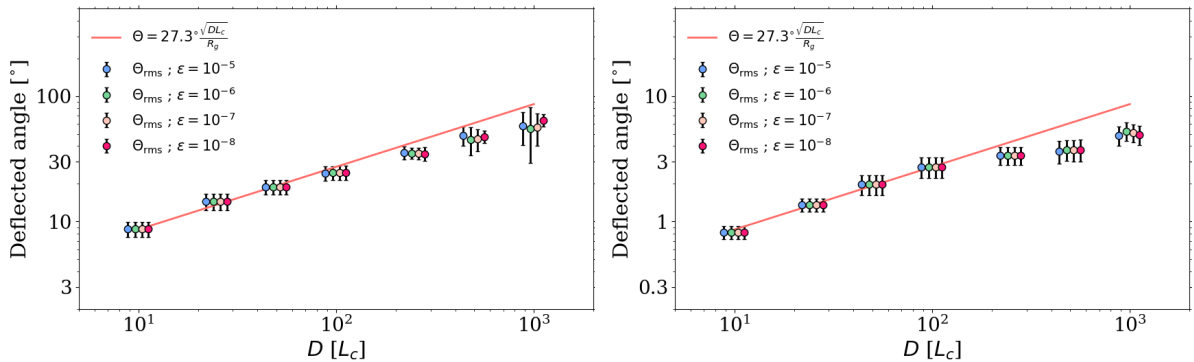


Figure 4.3: Plot of charged particles in same magnetic fields using different values for the local truncation error threshold ε . Left panel is for $R_g = 10 L_c$, while the panel on the right is for $R_g = 100 L_c$.

Figure 4.3 shows simulated results of charged particle deflection in a turbulent magnetic

field for different values of ε . The figure on the left is for $R_g = 10 L_c$, and the figure on right is for $R_g = 100 L_c$. Every cluster of error bars has been simulated over the same distance D and with the same turbulent magnetic fields. However, the threshold error ε for each step in the numerical solver is different for each error bar inside the cluster. The results are spread out on the x-axis for easier evaluation. For larger D and smaller R_g , the ε should be corrected accordingly. Nevertheless, this is of little importance, because in the case of this thesis, the typical interaction length is several orders lower than the general correlation length. Besides, R_g has a lower limit, which will let the program discard a particle before ε needs to be modified. Choosing $\varepsilon = 10^{-5}$ is more than accurate enough for the propagation in a turbulent magnetic field $D \leq 100 L_c$. The relative error between using $\varepsilon_5 = 10^{-5}$ and $\varepsilon_8 = 10^{-8}$ for $D = 100 L_c$ and $R_g = 10 L_c$, is $\Theta_{\varepsilon_5}/\Theta_{\varepsilon_8} = 1 + \mathcal{O}(10^{-3})$. It can be argued that in the case of this thesis, one could even use $\varepsilon = 10^{-4}$, or chose a dynamic value for ε based on L_c and R_g . However, both cases have been tested and do not improve the computing time notably. Choosing $\varepsilon = 10^{-5}$ is accurate enough and still very time competitive.

In this section, the numerical solver for the deflection in a turbulent magnetic field has been presented. The solver has been chosen based on its advantage on both precision and speed. The adaptive stepsize routine performs excellently for turbulent fields. It is warmly recommended by "*Numerical Recipes*" [24] and has been tested to provide excellent results compared to analytic formulae. For the case of this thesis, the numerical solver should use the initial parameters listed in Table 4.2.

Table 4.2: Summary of initial parameters for the numerical solver.

Variable definition	Value
Initial stepsize	$L_c/10^3$
Minimum allowable stepsize	$L_c/10^8$
Truncation error threshold	10^{-5}
Maximum number of steps	100 000

One of the main objectives in this thesis was to update the program ELMAG to calculate a three-dimensional cascade in a turbulent magnetic field. In this chapter, the complete program will be presented. First, in section 5.1, the modeling of the cascade will be qualitatively presented. This section will refer to the theory of particle physics needed to calculate cross sections, and give a qualitative understanding of how the major routines work. Second, in section 5.2 all files, and the most important routines will be described. Further, in section 5.3, example files of how to give input and construct output from the program will be explained. Finally, some necessary theory for the generated results will be presented in section 5.4. The program is written in Fortran, mainly with the syntax from the Fortran 90 release. All files, routines, functions and variables of the program will be presented in typewriter font, e.g. ELMAG, to easier identify the names used in the program. Note also that D was used as the length propagated by a charged particle inside a turbulent magnetic field in section 4.2. Henceforth, D will be defined as the length from a source to the Earth.

5.1 MODELING OF THE CASCADE

The two first paragraphs in this section are describing the modeling of scattering with the EBL and the weighted sampling process. These models have not been changed since the previous release, and are the same sections as presented by Kachelrieß et al. [5]. They are presented here as well, to complete a standalone demonstration of the program.

Interaction of photons and electrons/positron with the EBL

The theory of scattering on the EBL was derived in chapter 3. In section 3.2 the functions and threshold used in the program for modeling of the interactions were presented. This is used to compute the next interaction point of every particle, when to discard particles and the energy fractions left to secondary particles. The interaction rates R_γ and R_e from Eq. (3.17) and Eq. (3.20) are used to compute the traveled length before next interaction point. The threshold of $E_\gamma > E_{\text{th}}$ excludes uninteresting particles and secondaries calculations. As the

program speeds up its computations by omitting calculations of IC scattering for secondary photons beneath this threshold, it corrects for the relevant energy loss by Eq. (3.22). Finally, the energy fraction of the secondary particles is decided by Eq. (3.19) and Eq. (3.23) for pair production and IC scattering respectively.

Weighted sampling

The produced secondary particles are subject to a weighted sampling procedure. A secondary particle carrying the energy fraction y of the parent energy is discarded with the probability $(1 - y^{\alpha_{\text{sample}}})$, or added with the probability $y^{\alpha_{\text{sample}}}$ to the stack. Depending on the choice of the sampling parameter ($0 \leq \alpha_{\text{sample}} \leq 1$) either all the secondaries are kept in the cascade ($\alpha_{\text{sample}} = 0$) or only some representative ones. In particular, one secondary per interaction is retained on average for the value $\alpha_{\text{sample}} = 1$. As compensation, each particle in the cascade acquires a weight w which is augmented after each interaction as $w \rightarrow w/y^{\alpha_{\text{sample}}}$.

The optimal value of α_{sample} depends on the typical energy of the injected photons and the desired output.

Stacking

The stack holds all secondary particles that have yet to be calculated. At each loop, the lowest energy particle is extracted from the stack and traced further in the cascade process. The stack holds non-constant critical parameters defining each particle. As mentioned above, the weight of the particle is redefined through $w \rightarrow w/y^{\alpha_{\text{sample}}}$ at each interaction. Thus it must be conserved for each particle in the stack. The other parameters, are the particle's energy e_0 , its current redshift z , charge iq , total traveled distance s , the time delay dt , and finally the three-dimensional position- and velocity vector y (six-dimensional vector). The two new variables in this release is s and y . Calculating the final time delay of each particle can be done by knowing the total traveled distance s when the particle reaches the sphere of length D (in the program this length is the parameter $rcmb$). However, dt must also be included in the stack to account for the kinematic time delay when the particle is massive. y is inherited from the respective parent particle, and is used in the numerical routine for solving the Lorentz force ODE.

Turbulent magnetic field and angular deflection

As the secondary charged particles traverse the Universe, they are influenced by the EGMF. The EGMF in this program is a turbulent magnetic field with a correlation length in the order $L_c \approx 1$ Mpc, but can be chosen to any desired value. The field is generated based on the description from section 4.1, with a strength $10^{-13} \text{ G} \leq B_{\text{rms}} \leq 10^{-16} \text{ G}$. Because the magnetic field is turbulent, the trajectory of the particle needs to be calculated accurately. Also, computationally intensive algorithms are undesirable, which makes the fifth order Runge-Kutta adaptive stepsize solver from section 4.2 a great choice for this program.

Synchrotron radiation

The charged particle also emits synchrotron radiation. This happens when it undergoes acceleration perpendicular to the velocity. The formula for the total power radiated from any particle is given by Liénard's generalization of the Larmor formula [25, p. 463, Eq. 11.73]

$$P = \frac{\mu_0 q^2 \gamma^6}{6\pi c} \left(a^2 - \left| \frac{\mathbf{v} \times \mathbf{a}}{c} \right|^2 \right). \quad (5.1)$$

Here μ_0 is the magnetic permeability in vacuum, q the charge of the particle, c the speed of light, and \mathbf{v} and \mathbf{a} the velocity and acceleration of the particle respectively. Eq. (5.1) holds in both the relativistic and non-relativistic limit.

In the case where \mathbf{a} is perpendicular to \mathbf{v} , the particle is deflected in a circular motion. This is called synchrotron radiation, and one will get

$$\left(a^2 - \left| \frac{\mathbf{v} \times \mathbf{a}}{c} \right|^2 \right) = a^2 \left(1 - \frac{v^2}{c^2} \right) = a^2 \gamma^2,$$

which makes Eq. (5.1) reduce to

$$P_{\text{sync}} = \frac{\mu_0 q^2 a^2 \gamma^4}{6\pi c}. \quad (5.2)$$

The radiation is emitted in a cone with an opening angle defined by $\phi \sim 1/\gamma$, i.e. that a highly relativistic particle will emit radiation parallel to the velocity.

To increase computational efficiency synchrotron energy losses of the charged particles are accounted for in the continuous energy loss approximation. In this program this is done by using the interpolation formula from Baier et al. [26],

$$\frac{dE}{dx} \simeq \frac{m_e^2 \chi^2}{[1 + 4.8(1 + \chi) \ln(1 + 1.7\chi) + 3.44\chi^2]^{2/3}}, \quad (5.3)$$

with $\chi = (p_{\perp}/m_e)(B/B_{\text{cr}})$, where p_{\perp} denotes the momentum perpendicular to the magnetic field and $B_{\text{cr}} = 4.14 \cdot 10^{13}$ G the critical magnetic field.

Angle delay

In the program, one can initialize the blazar jet opening angle Θ_{jet} , and the jet offset Θ_{obs} . The opening angle Θ_{jet} is related to the blazar's individual Lorentz bulk factor (Γ) through $\Theta_{\text{jet}} = \Gamma^{-1}$. The Earth is defined at the Origin in the xy -plane and at a distance D in z -direction, independent of Θ_{obs} . Θ_{obs} defines the initial velocity of each particle. The particle will be traced until it reaches a distance $> 0.999D$ from the Origin, i.e. $\sqrt{x^2 + y^2 + z^2} > 0.999D$. After that, it will be projected onto the sphere of radius D . Letting f denote the fraction that each final velocity component (v_x, v_y, v_z) has to be multiplied with to reach the sphere, the equation that remains to be solved is

$$D^2 = (x + v_x f)^2 + (y + v_y f)^2 + (z + v_z f)^2, \quad (5.4)$$

where (x, y, z) is the final position. Solving Eq. (5.4) for f and choosing the lowest absolute value of the two solutions, gives the correction factor to the final position $(x, y, z) \rightarrow (x + f, y + f, z + f)$. By defining the Earth at the position as described above, one can now require that

$$\Theta_{\text{jet}} \geq \arctan \frac{\sqrt{x^2 + y^2}}{z}, \quad (5.5)$$

where (x, y, z) is the corrected final position. If Eq. (5.5) holds, the particle track can be rotated to hit the Earth and still be initiated from inside the jet. It is worth noting that Eq. (5.5) works independently of Θ_{obs} . Doing the calculations this way is much more computing efficient than first initializing particles randomly inside the jet, and then recording only the ones that hit the Earth.

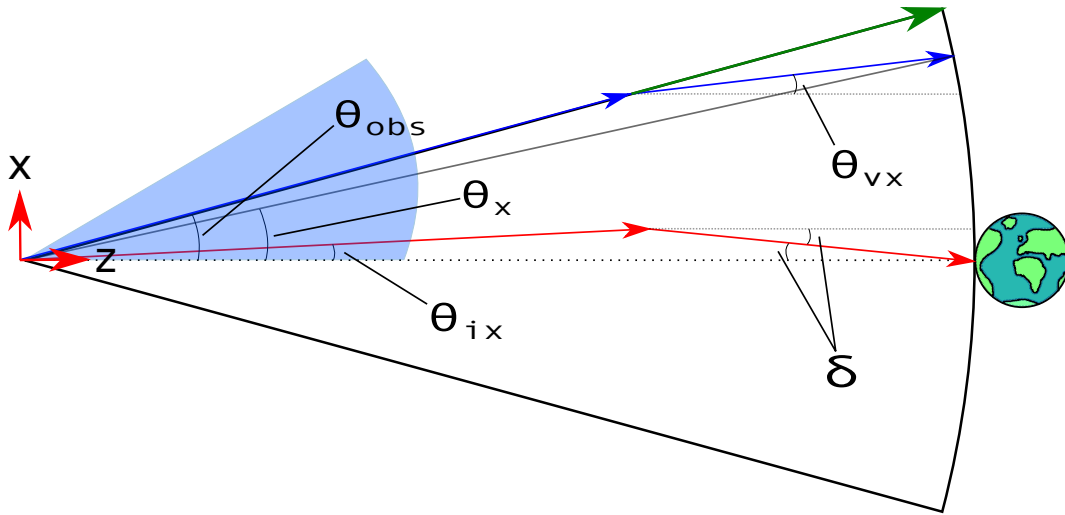


Figure 5.1: Sketch of particle calculation with a blazar jet misalignment by $\Theta_{\text{obs}} = \Theta_{\text{jet}}$ towards Earth. The green arrow represents the initial starting velocity (center of the jet). The blue arrows represent the tracking of the initial particle. Last, the red arrows represent the rotated path of the initial particle, projected to hit the Earth. The blue cone represents the blazar jet.

Figure 5.1 visualizes how the rotation in the two-dimensional space of the xz -plane is done. The green arrow represents a particle track initialized at $\Theta_{\text{obs}} = \Theta_{\text{jet}}$ with no deflection. The blue arrows visualize a deflected track, with the red arrows representing the deflected track rotated to hit the Earth. As is clear from the figure, the red arrows are initiated inside the jet. The arc tangent to the Earth, is the possible outcome for the blue arrows to end, and where the two-dimensional version of Eq. (5.5) ($-\Theta_{\text{jet}} \leq \Theta_x \leq \Theta_{\text{jet}}$) still holds, assuming deflection in y -direction is zero.

The observed angle δ is in general defined by $\delta \rightarrow \delta(\Theta_{\text{vx}}, \Theta_x)$, where $\Theta_{\text{vx}} = \arctan \frac{v_x}{v_z}$ and $\Theta_x = \arctan \frac{x}{z}$. However, the routine is also modified to include the angle Θ_{ix} , which is used to find the angle of the initial particle from the jet center. This makes it possible to include a weighted particle distribution inside the jet. To find Θ_{ix} , one has to mirror Θ_x over the axis defined by $\Theta_{\text{obs}}/2$. This results in the equation $\Theta_{ix} = \Theta_{\text{obs}} - \Theta_x$. Observing that the triangle made by the Origin and the two red arrows is the same as the triangle made by the Origin and

the two blue arrows, one can calculate δ by knowing Θ_{obs} , Θ_{vx} and Θ_{ix} . The formula becomes $\delta = \Theta_{\text{vx}} + (\Theta_{\text{ix}} - \Theta_{\text{obs}})$.

Cosmology

The connection between redshift z , comoving distance r and light-travel time t calculated for a flat Friedmann-Robertson-Walker universe with $\Omega_{\Lambda} = 0.7$ and $\Omega_m = 0.3$ is contained in the file `redshift.f`.

5.2 PROGRAM STRUCTURE

In this section a presentation of all the files in the program will be given. The most critical routines will be described in detail, to give a better understanding when reading the code. In section 5.1, it was explained that the program calculates a particle trajectory until it reaches the sphere of radius D . Then, by rotating the path of the particle to hit the Earth and checking if the starting velocity resides within the jet, the program determines if the particle should be discarded. For the convenience of explanation: reaching the sphere of distance D , is henceforth referred to as reaching the Earth.

The complete program is distributed among the files `modules204.f90`, `bturb.f90`, `user204.f90`, `init203.f90`, `elmag204.f90`, `aux202.f90` and `dgl_numrec.f`, in addition to `main_sp204.f90` and `main_mpi204.f90`. The two latter files are the routines to execute the program, respectively a single processor simulation and an mpi-simulation. The file `modules204.f90` contains the definition of internal variables, mathematical and physical constants; for standard applications of the program no changes by the user are needed. The file `bturb.f90` contains the subroutines for generating the turbulent magnetic field according to the description in section 4.1. The file `user204.f90` contains all the input/output routines developed by the user for the desired task. This file is where the user can modify the parameters of the magnetic field, the desired number of particles to simulate, observed output grid, different models for the EBL, energy distribution spectrum etc. and works as the true main-file of the program. `user204.f90` calls `init203.f90` to initialize the desired EBL-model. Data files of the used EBL backgrounds and the cosmological evolution of the universe are provided in the directory `Tables`. They are read by the subroutines `init_EBL(myid)`, `init_arrays(myid)` and the function `aintIR(E,z)` inside the file `init203.f90`. Then the function `w_EBL_density_tab(emin,zz)` tabulates the weighted background photon density I_{γ} defined in Eq. (3.18), followed by the tabulation of the interaction rate in the the subroutine `rate_EBL_tab(e0,zz,icq)`.

The routines within the file `dgl_numrec.f` are from "*Numerical Recipes*" [24, Ch. 16.2], and completes a full-fledged ODE solver with adaptive stepsize control using a fifth- and fourth order Runge-Kutta method. In general, `dgl_numrec.f` works as a standalone program, with calls to only one external routine `derivs`, which is specific for the ODE needed to be solved. Within `dgl_numrec.f` it is possible to change the maximum number of steps for the solver to take, defined in Table 4.2. For a detailed explanation of the routines in the file, please see section 4.2. The inputs/outputs from the subroutine `odeint` will be discussed below in

the paragraph about subroutine `propagate`.

A general description of how the modeling of the cascade is done was provided in section 5.1. The subroutines and functions necessary for the electromagnetic cascade modeling are located in the file `elmag204.f90`, which constitute the core of the program. Now in more detail, each of the subroutines and functions of `elmag204.f90` will be presented:

- subroutine `cascade(icq,e00,weight0,z_in)`
Follows the evolution of the cascade initiated by a photon ($icq = 0$) or an electron/positron ($icq = \pm 1$) injected at redshift z_in with energy $e00$ and weight $weight0$ until all secondary particles have energies below the energy threshold $ethr$, or have reached the Earth. The routine will also discard particles that are deflected more than a certain threshold, which is currently set to having a negative velocity component in z -direction.
- subroutine `propagate(y,x,e0)`
Calculates the trajectory of a charged particle in the turbulent magnetic field by calling `odeint(y,nvar,0,x,eps,h1,hmin,nok,nbad,derivs,rkqs,tf)` located in the file `dgl_numrec.f`. The routine initialize the numerical solver with the parameters from Table 4.2, where $h1$ is the initial stepsize, $hmin$ is the minimum allowable stepsize and eps is the local truncation error threshold. The particle is tracked for the interaction length x , with y containing the particle's position and velocity ($[x, y, z, v_x, v_y, v_z]$), where $nvar = 6$ is the number of elements in y . The outputs nok and $nbad$ are the number of good and bad (but retried and fixed) steps taken. The inputs `derivs` and `rkqs` are external routines that will be called from inside `odeint`. The output `tf` is a customization to the original numerical solver from "*Numerical Recipes*" [24]. It is a logical variable set to `.false.` if the solver reaches the maximum number of steps before reaching interaction length x . If this happens, the particle will be discarded. After y undergoes deflections in the numerical solver, the absolute value of the particle's velocity components might be slightly different from 1. Thus, y is normalized by the subroutine `normalizer(y)`.
- subroutine `normalizer(y)`
Normalizes the velocity components of y so that the absolute value is 1. This is a security measure, originally implemented to make sure no particles reach the Earth with negative time delay.
- subroutine `derivs(x,y,dydx)`
Is the external subroutine called from `odeint`, as a part of the numerical solver. The input x is of interest if the magnetic field changes with time, but is for now avoided. The routine inputs the position and velocity of the particle in the six-vector y , and outputs its derivatives $dydx$. The three first values of $dydx$ are simply the three last values of y in their respective order. The last three elements of $dydx$ are obtained by solving Eq. (4.8). The magnetic field is found by calling the routine `generate_B(s, Omega)`, where s is the position vector of y and Ω is the three-dimensional magnetic field at position s . The routine `generate_B` uses the initialization done in the `bturb.f90` file to generate the isotropic magnetic field Ω at point s .

- subroutine `angle_delay_3d(y, e0, s, thetax, thetay, dt, w2)`
Determines the time-delay `dt` and the observation angle in the two-dimensional plane from the perspective of a detector on Earth (sky image). For more details on how the calculations are done, see the paragraph *Angle Delay* in section 5.1. The outputs `thetax` and `thetay` are analogous to the δ -value in figure 5.1 for the observed angles in respectively the xz -plane and the yz -plane. The output variable `w2` is the weighting variable accounting for a non-uniform jet distribution. It is calculated by calling the subroutine `jet_distribution(the_s, w2)`, where the desired jet distribution profile is specified.
- subroutine `angle_delay_1d(e0, xx, the, theta, dt)`
Determines the time-delay `dt` and the observation angle `theta` from the root mean square cascade deflection angle `the` and the last interaction point `xx`. This routine is only toggled when using the old program structure.
- subroutine `interaction(y, e0, zz, weight, s, dt, icq, ierr)`
Handles one interaction with background photons. In the case of `icq=0` the routine determines the center of mass energy `sgam` of the reaction via a call to `sample_photon`, then distributes the energy fraction of the secondaries by calling `zpair(sgam)`. For `icq=1` or `-1`, the subroutine determines `sgam` via a call to `sample_electron(e0, zz, sgam)` and the energy fractions are distributed by calling `zics(e0, sgam)`. The secondaries are then stored in the stack by calling the subroutine `store_particle`. They inherit all variables except the energy from their respective parent particle.
- subroutine `store_particle(y, e0, zz, ze, weight, s, dt, icq)`
Decides if a produced secondary is stored using weighted sampling; if yes, it adds the secondary to the array event and re-orders the array according to the particle energies.
- subroutine `get_particle(y, e0, zz, weight, s, dt, icq)`
Reads the secondary particle with the lowest energy out of the array event and reduces `jcmb` by one. The variables in this routine are all the critical variables for continuing the cascade of secondaries. `get_particle` is called by `cascade` to develop the cascade further from each interaction point, until the cascade vanishes beneath the energy threshold or reaches the Earth.
- subroutine `sample_photon(e0, zz, sgam, ierr)`
Determines the center of mass energy `sgam` of an interaction at redshift `zz` for pair production.
- subroutine `sample_electron(e0, zz, sgam, ierr)`
Determines the center of mass energy `sgam` of an interaction at redshift `zz` for IC scattering.
- double precision function `w_EBL_density(emin, zz)`
Calculates the weighted background photon density I_γ defined in Eq. (3.18).
- double precision function `int_length(e0, zz, icq)`
Finds the length traveled before next interaction with EBL photons.

- double precision function `sigpair` and `sigics(e0,sgam)`
Calculate the pair production and IC scattering cross section respectively.
- double precision function `zpair(sgam)` and `zics(e0,sgam)`
Determine the energy distribution in pair production and IC scattering respectively.
- double precision function `zsigics(e0,sgam)`
Calculates the cross section times energy lost below the chosen threshold in IC scattering.
- double precision function `zloss(e0,zz)`
Interpolates the integrated energy loss due to emission of photons below the desired threshold energy.
- double precision function `rate_bb(e0,zz,icq)`
Interpolates the interaction rates R_γ or R_e on EBL photons.
- double precision function `eloss(e0,begmf)`
Calculates the synchrotron losses according to Eq. (5.3).
- double precision function `themf(e0,begmf)`
Determines the deflection angle in a uniform EGMF.

The file `aux202.f90` contains auxiliary functions, e.g. the random number generator `psran` from "*Numerical Recipes*" [27].

5.3 EXAMPLE INPUTS/OUTPUTS

The file `user204.f90` is an example file for the input/output subroutines which should be developed by the user for the desired task. The program is distributed with the file discussed in this section. The output routines are inspired by the sky image brightness profiles of high energy blazars presented by Neronov et al. [28]. The point spread function (PSF) used for visualization is left for the detector specialists to specify more accurately, but for now a homogeneous distribution within an angular containment radius of 95 % is used.

5.3.1 Input parameters and variables

The input for the program is contained in the file `user204.f90`. The input variables specified in the module `user_variables` are: the choice to use the old program by setting `old_calc = 1`, what EBL-model (`model`) to use, the number of injected particles (`nmax`), the jet opening angle of the source in degrees (`th_jet`), the jet offset angle in x -direction towards Earth in degrees, the sampling parameter `a_smp`, the energy threshold `ethr` (E_{th}) for Compton scattering, and the maximal photon energy `egmax`. The last two parameters also serve as minimal and maximal energy in the energy spectra produced as output. In particular, `ethr` should not be much lower than 1 GeV, which is the default value in the program.

The variables in module `bfield_parameters` defines how the construction of the magnetic field is done. These are: if the magnetic field should be constant (`model_b=1`) or turbulent (`model_b=2`), how many modes the turbulent field should be generated by (`n_k`), the root mean square value of the magnetic field (`B_rms`), the power law fluctuations (`alpha`), the minimum and maximum value of the wave vectors of the generated modes `k_min` and `k_max` and the helicity `h` of the generated modes. The latter is a `double` between 0 and 1, where `h= 1` makes all modes right-handed, `h= 0` makes all modes left-handed and `h= 0.5` makes them 50 : 50. There is also a default value of the magnetic field's coherence length (`L_c`), which will be changed according to Eq. (4.5) if the magnetic field is turbulent. It is also worth noting that `B_rms` and the default value of `L_c` are the only variables of significance in this module when the magnetic field is chosen to be constant or `old_calc = 1`.

The file also contains the module `user_result`, where time bins, angle bins and parameters for plotting are specified. These define the vectors and matrices where all the results will be stored. Also, the module contains two counters `n_reg` and `n_kc`, which respectively counts the number of detected photons and the number of unresolved paths (that are then discarded) in the numerical solver.

In subroutine `user_main(myid,nmax)` the initial redshift `z` and the particle type `icq` of the injected particles is fixed.

```
z = 0.10d0                                ! initial redshift
do nl=1,nmax
  call initial_particle(e0,weight)         ! generate initial energy
  icq = 0                                  ! (0 - gamma, +-1 - e+-)
  call cascade(icq,e0,weight,z)           ! starts EM-cascade
enddo
```

The subroutine `initial_particle(e0,weight)` chooses the energy and the weight of one initial particle in the energy range [`emin`, `egmax`] according to a desired power law.

As mentioned in subsection 5.1 the program can now take into account a jet distribution profile. The desired distribution function can be specified in the subroutine `jet_distribution(the_s,w_jet)`, where the input `the_s` is the starting angle from the jet center, and the output `w_jet` is the applied weighting defined by the jet distribution. In the release, the distribution is set to be Gaussian profile, with

$$w_{\text{jet}} = \exp(-\text{the_s}^2/\text{th_jet}^2).$$

When initiating the cascade using the MPI routine, the program will initialize a set of all the random parameters needed for the generation of the helical turbulent magnetic field. Because the routines are internal for each processor, using MPI will by default track particles in different magnetic fields for every processor. This is fixed by only initializing the turbulent field on the root processor, and then casting the random variables to the parallel processors. Thereby all processors track particles in the same magnetic field. The file `main_mpi204.f90` takes care of this by `CALL MPI_BCAST`,

```
CALL MPI_BCAST(ca,n_k,MPI_DOUBLE_PRECISION,0,MPI_COMM_WORLD,ierr)
```

Here `ca` is one of the arrays containing the random variables, and `n_k` is the range of the array (which in this case is the number modes for the turbulent magnetic field).

5.3.2 Output

After a particle is traced through the cascade process, it is stored in the module `user_result` by the subroutine `register(e0, thex, they, weight, dt, icq)`. The three-dimensional array storing the brightness profile from the blazar is `anobs(n_bint, n_binx, n_biny)`, and depends on the parameters `n_bint`, `n_binx`, `n_biny`, `n_bind`, and `shiftx`. These parameters are respectively the number of time bins for the time delay, the number of bins in x -direction and in y -direction, number of bins per degree, and how many degrees the grid is shifted in x direction. For a brightness profile split into five time bins, with a resolution of 30 bins per degree, ranging in the intervals $-6^\circ \leq \Theta_x \leq 12^\circ$ and $-6^\circ \leq \Theta_y \leq 6^\circ$, one can use the parameters; `n_bint=5`, `n_binx=541`, `n_biny=361`, `n_bind=30` and `shiftx=3`.

To take into account the typical characteristics of a detector the program uses the same PSF as from Dolag et al. [29]

$$\vartheta_{95} \simeq 1.68^\circ (E/1 \text{ GeV})^{-0.77} + 0.2^\circ \exp(-10 \text{ GeV}/E), \quad (5.6)$$

where E is the particle energy and ϑ_{95} is the angular containment radius of 95 %. This function is an analytic approximation of the measured PSF from Fermi-LAT. Above 300 GeV the typical PSF from a Cherenkov Telescope is used, i.e. $\vartheta_{95} = 0.11^\circ$. The function `thereg_en(e0)` in the program returns the value of ϑ_{95} .

Each particle is mapped into the array `anobs`, through the subroutine `psf_spread(e0, thex, they, weight, dt)`. Here, the size of the time delay bins are defined; 1: $0 < \tau < 10^5$, 2: $10^5 \leq \tau < 10^6$, 3: $10^6 \leq \tau < 3 \cdot 10^6$, 4: $3 \cdot 10^6 \leq \tau < 10^7$ and 5: $\tau = 0$, with τ denoting the time delay and all in units of yr. This subroutine calls `thereg_en(e0)`, and distributes the brightness homogeneously in the disk of angular radius ϑ_{95} from point `(thex, they)`. The other mapping routines from the previous program are also present in this release.

All output data arrays exist in two versions, e.g. `anobs(n_bint, n_binx, n_biny)` and `anobs_tot(n_bint, n_binx, n_biny)`. Using MPI [30], the former arrays contain the result of a single processor, which are summed into `anobs_tot(n_bint, n_bint, n_biny)` by call `MPI_REDUCE`,

```
n_array = n_bint*n_binx*n_biny
call MPI_REDUCE(anobs,anobs_tot,n_array,MPI_DOUBLE_PRECISION,MPI_SUM,0,
               MPI_COMM_WORLD,ierr)           ! sum individual arrays spec
```

Finally, the subroutine `user_output(n_max, n_proc)` writes the complete data arrays with the results to the files contained in the subdirectory `Output`. The results from `anobs_tot` will be written to the subdirectory `AngRes` within `Output`.

The files `angle_matrix1` to `angle_matrix4` contain the normalized surface brightness for the time bins 1 to 4. At energies $E_\gamma < 1$ GeV ϑ_{95} grows big, and already at $E_\gamma \simeq 0.1$ GeV, it becomes $\vartheta_{95} = 9.8^\circ$. This is a huge variance, especially considering the use of a homogeneous distribution within the angular radius. Therefore, all sky image simulations have been restricted to only evaluate cascade particles of $E_\gamma > 1$ GeV, which is defined earlier as the energy threshold E_{th} .

5.4 ADDITIONAL THEORY FOR INTERPRETING THE RESULTS

As mentioned in section 5.3 the program is made to allow any user to specify their own desired inputs and outputs. In this thesis, the program has mainly been used to produce surface brightness images around the Blazar 1ES 0229+200. A qualitative analysis of constraints to the parameters of the EGMF, the time delay τ of the expanding halo and energy distribution of the jet will be presented.

5.4.1 Qualitative Analysis

Based on the attenuation length equations from section 3.3 and the angular deflection equations in section 4.2, one can do a qualitative analysis of the particle trajectory to predict constraints on the parameters of the EGMF.

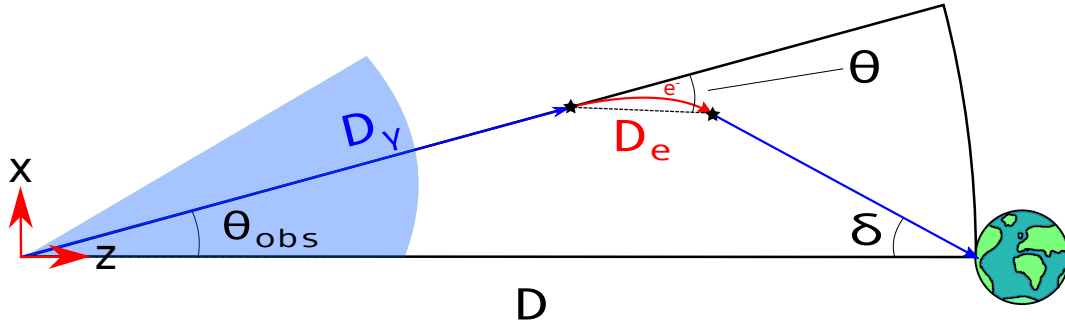


Figure 5.2: Qualitative sketch of particle track from source to the Earth. The blue arrows represent a photon, while the red arrow represents an electron. The particle is initiated with a misalignment angle Θ_{obs} .

Figure 5.2 shows a possible cascade process from source to the Earth. The particle first makes pair production with EBL after a length D_γ , and then the secondary electron IC scatters a photon after length D_e , which can be observed from at an angular distance δ away from the point source. Assuming now that the energy of the primary photons is $E_{\gamma_0} = 1$ TeV, the attenuation length of the photon becomes $D_\gamma \simeq 800$ Mpc by Eq. (3.24). The particle then splits its energy in half giving the electron $E_e = 0.5$ TeV. The attenuation length of the electron is then $D_e \simeq 0.65$ Mpc by Eq. (3.25). For a given correlation length of the magnetic field, either Eq. (4.12) ($D_e \gg L_c$) or Eq. (4.13) ($D_e \ll L_c$) can be used to calculate the deflected angle Θ . Calculating Θ leads to finding the observed angle δ . Now, assuming that δ is small and that Θ can be approximated to the angle between the velocity of the primary photon and the velocity of the IC scattered photon, δ becomes

$$\delta = \Theta(B_{\text{rms}}, L_c) - \Theta_{\text{obs}}. \quad (5.7)$$

A measurement of δ provides a measurement of $\Theta(B_{\text{rms}}, L_c)$ by Eq. (5.7), and thus yields constraints on the parameters of the EGMF, i.e. B_{rms} and L_c . Many assumptions have been made in this subsection. However, the qualitative understanding persists, but a lot of statistics would be needed to provide credible constraints.

5.4.2 Time Delay

Considering the vast distance between the source and Earth, the time delay of secondary particles can be large. For the given jet opening angle Θ_{jet} and the jet misalignment angle Θ_{obs} , the time delay can be approximated by

$$\tau \simeq \frac{D}{2c} \delta (\Theta_{\text{jet}} + \Theta_{\text{obs}}), \quad (5.8)$$

where D is the distance to the source, and δ is the angular distance from the point source in the sky image [28]. For the Blazar 1ES 0229+200, the distance is $D \simeq 540$ Mpc. Now, it would be preferable to express τ in units of yr and the angles in units of degrees, which reduces Eq (5.8) to

$$\tau \simeq 6.7 \cdot 10^6 \left[\frac{\delta}{5^\circ} \right] \left[\frac{\Theta_{\text{jet}} + \Theta_{\text{obs}}}{5^\circ} \right] \text{ yr}. \quad (5.9)$$

Eq. (5.9) is excellent to use for qualitative understanding of time delay in cascades from TeV-sources, but should however be taken with care when comparing with results from ELMAG. The equation is based on first order cascades and uses the approximated deflection angle from Eq. (4.12) and Eq. (4.13). The program, on the other hand, also accounts for pair production from secondary photons in addition to calculating the exact deflection of each particle.

5.4.3 Energy Distribution

Different sources are expected to have different energy distributions. Neronov et al. [28] uses a monochromatic primary γ -ray beam with energy $E_{\gamma_0} = 1$ TeV. This is not a realistic case but is used to give a good qualitative analysis of how a sky image might look.

The program uses many similar programming routines as the program developed by Elyiv et al. [21], which makes a comparison between results from the two programs a good verification that this program works as expected. Elyiv et al. uses an energy distribution

$$E_{\gamma_0}^2 dN_{\gamma_0}/dE_{\gamma_0} \propto \exp(-E_{\gamma_0}/E_{\text{max}}), \quad (5.10)$$

with an exponential cutoff at $E_{\text{max}} = 300$ TeV.

The main results in this thesis are simulations of the Blazar 1ES 0229+200. The previous release of ELMAG was used to do calculations in the paper by Dolag et al. [29]. For this source, the energy distribution is estimated to be

$$E_{\gamma_0}^2 dN_{\gamma_0}/dE_{\gamma_0} \propto E^{1/3}, \quad (5.11)$$

with a sharp cutoff at $E_{\text{max}} = 20$ TeV.

The main objective of this thesis was to make the program routines to work for a cascade in a three-dimensional turbulent EGMF. It can now calculate the cascade of an arbitrary source, with any desired parameters of the jet and parameters of the EGMF. The program is thus the main result of this thesis. However, in this chapter various tests of the program will be presented. In section 6.1 results from the new program will be compared to results from the old program. This section will also justify the need for a switch to use the old routines within the new program. In section 6.2 motivational tests of the program will be presented, where a produced surface brightness profile will be compared to another similar program. The program can now produce sky images from VHE γ -ray sources. Some examples will be presented in section 6.3, where also the results will be compared to expected time delay patterns. Simulations with various parameters of the EGMF will be presented and discussed, and polarization of the EGMF will be evaluated. Finally, in section 6.4, some recommendations for future work on the program will be presented.

6.1 COMPARISON TO OLD PROGRAM

By setting `model_b = 1` the program generates a uniform magnetic field. The strength of the field is still determined by `B_rms`, which in this section is set to $B = 10^{-17}$ G. Using the default value of `L_c`, the new program will now initiate a cascade with the same external properties as the old program.

The program initiate photons at redshift $z = 0.14$ following the energy distribution from Eq. (5.11). The jet opening angle is $\Theta_{\text{jet}} = 6^\circ$, with zero misalignment towards the Earth, i.e. $\Theta_{\text{obs}} = 0^\circ$. The objective of this section is to compare some of the outputs from the new and the old program, simulating with the same external parameters.

In the figures of this section all panels on the left are spectra from simulations with the new program, while panels on the right are spectra from the old program. The spectra visualize the flux $\mathcal{F} \propto E^2 dN/dE$ for a randomly chosen normalization, as a function of the arrival energy of the particle E_γ .

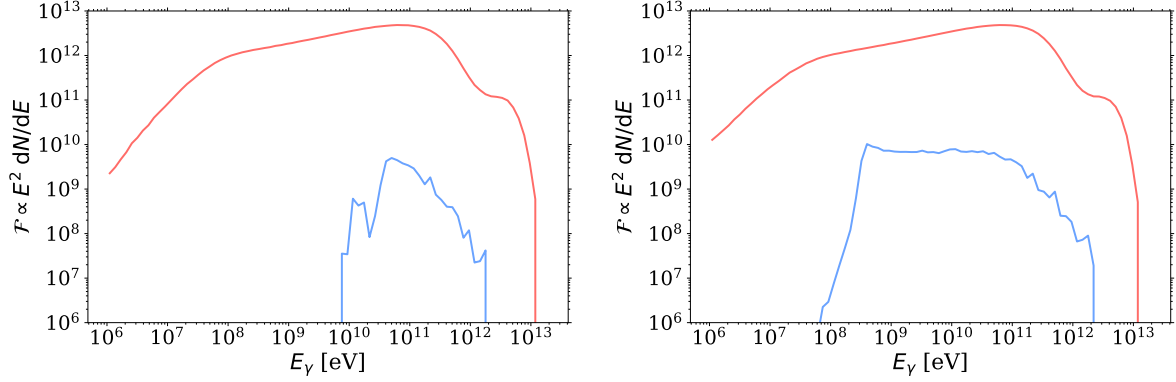


Figure 6.1: Simulations from the new (left) and old program (right). Red line is the observed photon spectrum inside the angular containment radius ϑ_{95} from the PSF in Eq. (5.6). Blue line is the observed electron/positron spectrum.

Figure 6.1 shows the photon spectrum (red line) and the observed electron/positron spectrum (blue line). While the photon spectrum is more or less intact for energies $E_\gamma > 10^8$ eV, the electron/positron spectrum seem to be broken off at energies $E_e < 5 \cdot 10^{10}$ eV. As mentioned in section 5.2, the new program will discard particles that have been deflected more than certain threshold angle. In this routine, the threshold is when a particle has a negative velocity component in z -direction. The Larmor radius R_g of relativistic particle was given in Eq. (4.9), and scales as $R_g \propto E$, i.e. that lower energy particles will be discarded with higher frequency. A 10 GeV particle has a Larmor radius of $R_g = 1.081$ Mpc in this magnetic field. A non-interacting charged particle around this energy will be confined within the field and discarded from the program after a travel length πR_g . Seeing that the more energetic part of the charged particle spectrum fits well compared to the old program, it is reasonable to assume that the drop in abundance at lower energies is because of the new feature; discarding particles deflected more than a given threshold angle.

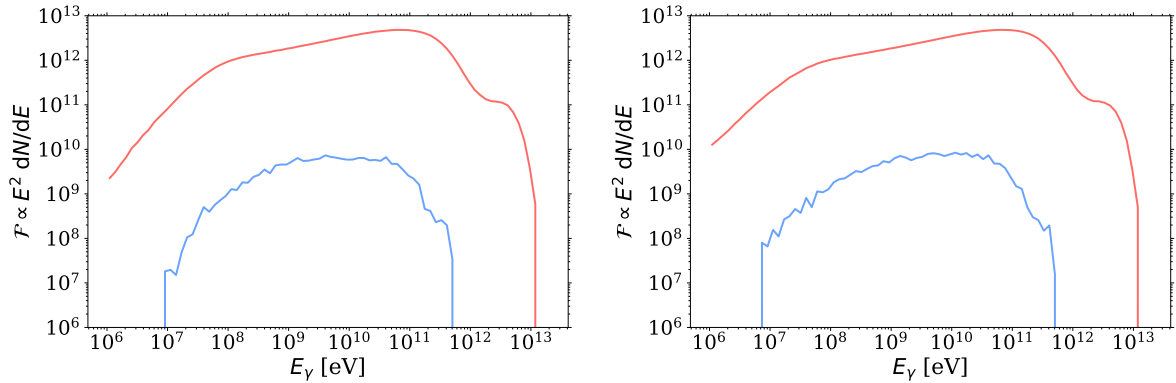


Figure 6.2: Simulations from the new (left) and old program (right). The blue line represent photons detected outside the angular containment radius ϑ_{95} , while the red line is the spectrum inside.

Figure 6.2 shows the observed spectrum inside (red line) and outside (blue line) the

angular containment radius ϑ_{95} from Eq. (5.6). The results from both programs are in good agreement. However, for lower energies ($E_\gamma < 10^8$ eV), the result from the new program shows a slightly lower abundance both inside and outside the angular containment radius. This is also consistent with the new program's feature of discarding photons at a given deflected angle. As argued for Figure 6.1, charged particles with lower energies will be discarded by the new program. Charged particles at these energies would also (if not discarded) make a contributions to the abundance of photons with energy $E_\gamma \lesssim 10^8$ eV through IC scattering.

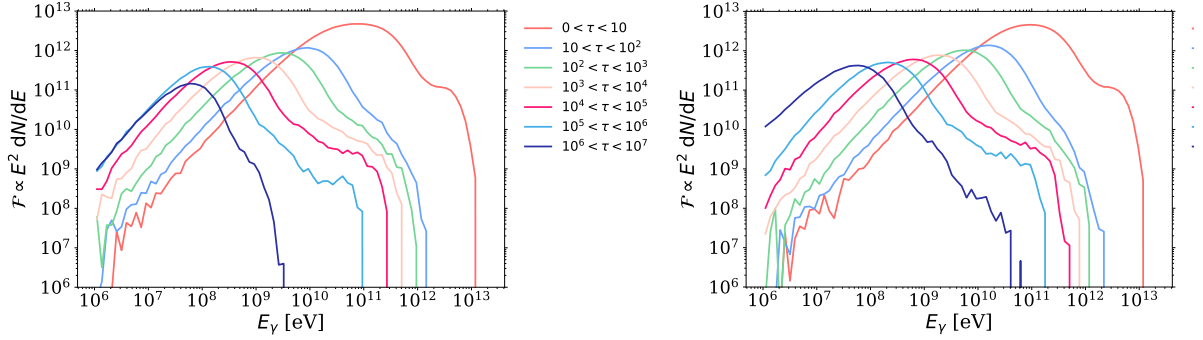


Figure 6.3: Simulations from the new (left) and old program (right). Photon spectrum split into time bins of arrival time after the first (non-interacting) photons. τ is in units of yr.

The photon spectrum inside the angular containment radius ϑ_{95} from Figure 6.2 can be split into epochs for arrival time after the first photon (time delay). Figure 6.3 shows these epochs. The first four epochs, i.e. $\tau \leq 10^4$ yr are in good agreement for both programs, but the last two seem to have a significant drop in abundance for the new program. This is also consistent with the new program's feature of discarding photons at a given deflected angle. The time delay origins from a more violent deflection in the magnetic field. A smaller Larmor radius, deflects a particle more, i.e. a bigger time delay. From Eq. (4.9) it is evident that $R_g \propto E_\gamma$, which means that a lower energetic parent particle will produce photons with more time delay. Since the new program will discard more of the lower energetic particles, it will also show a lower abundance for the more time delayed epochs.

Overall the new program compares well to the previous program when using a uniform magnetic field. The small differences come from the new feature of discarding particles above a given threshold deflection angle. The threshold is crucial to the efficiency of the program, as it now solves the three-dimensional path of each particle. Besides, particles deflected more than the threshold would never reach the Earth and are thus of little interest for further calculations. The new program is made to track the three-dimensional path inside a turbulent magnetic field. As mentioned in section 5.2, the resolution of a detector drops severely for $E_\gamma < 1$ GeV. This is also evident from the PSF function in Eq. (5.6), which increases for lower energies. When visualizing a theoretical sky image energies of $E_\gamma > 1$ GeV is of interest. At these energies the new program fits almost perfectly compared to the old program, which is a great indication that the new program works as expected.

6.1.1 Old Program Implementation

To make the new program a complete version of ELMAG it should be able to make the previous calculations from the old program as well. Because the new three-dimensional tracking does not make an accurate calculation for low energies, the old program is still contained within the new program. One can easily use the new program with the old routines by setting `old_calc = 1`. The desired correlation length and strength of the uniform magnetic field are defined by `L_c` and `B_rms` respectively.

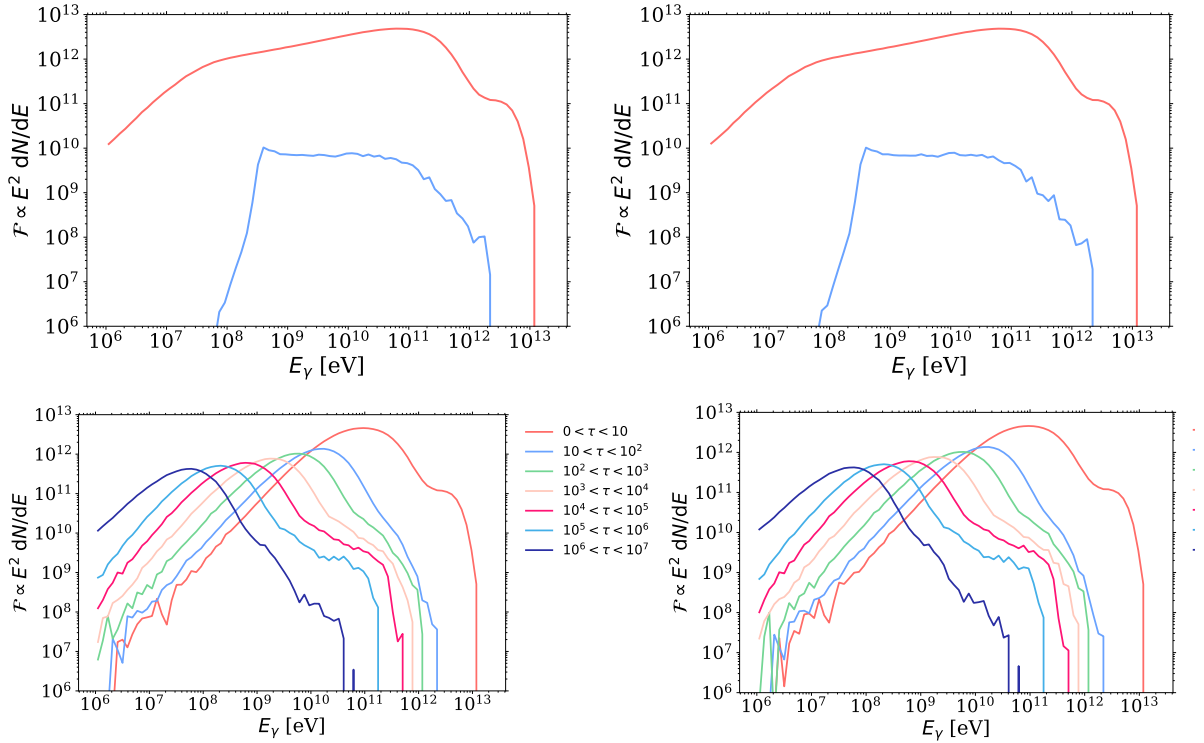


Figure 6.4: Comparison of old routines in new program (panels on the left) and the old program (panels on the right). Upper figures are the photon spectra inside the angular containment radius ϑ_{95} (red lines), and the electron/positron spectra (blue lines). Lower figures are the photon spectra split into epochs τ in unit of yr.

The panels on the left in Figure 6.4 shows spectra from the new program using the old routines. The panels on the right are the same as presented in section 6.1 for the old program. The panels on the left are more or less equal to the panels on the right, which means that the implementation of the old routine into the new program has been successful.

6.2 TESTS OF THE NEW PROGRAM

During the development of the program, routines have frequently been tested to make sure implementations have been done correctly. In section 4.2 some results were presented to

derive the necessary parameters for the numerical solver. However, the results from Figure 4.2 also proved that the complete numerical solver works according to Eq. (4.12) and Eq. (4.13) in Kolmogorov, Kraichnan and Bohm turbulence for any polarization of the magnetic field. An even simpler test would be to verify the Larmor radius from Eq. (4.9) in a uniform magnetic field.

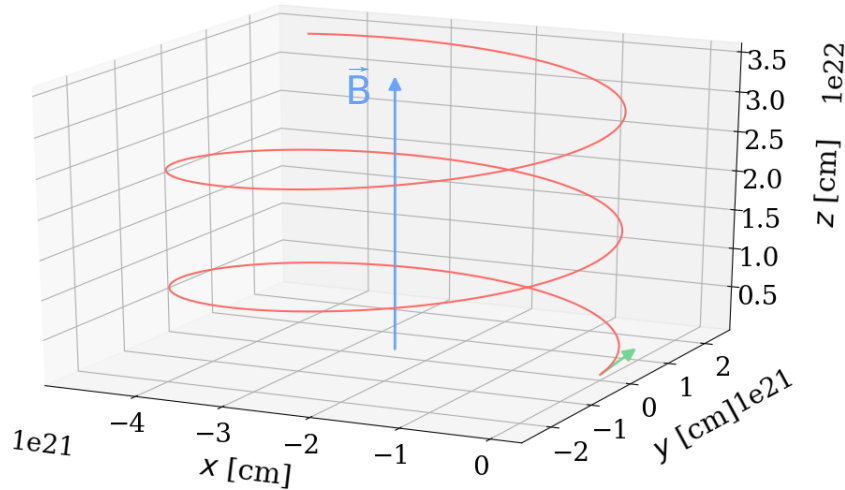


Figure 6.5: Helical motion of a charged particle in a uniform magnetic field. The initial velocity of the particle (green arrow) is $v_x = 0$ and $v_y = v_z = \sqrt{1/2}c$. The magnetic field (blue arrow) points in z -direction. Red line is the particle trajectory.

Figure 6.5 shows the motion of a charged particle in a uniform magnetic field. Letting \mathbf{B} (blue arrow) point in the z -direction and the initial velocity be $v_y = v_z = \sqrt{1/2}c$ (green arrow), gives a helical motion (red line) for the charged particle. The energy of the particle is 10^{13} eV and the magnetic field is $B = 10^{-11}$ G, which by using $\beta_{\perp} = 1/\sqrt{2}$ in Eq. (4.9) gives a Larmor radius $R_g = 2.359 \cdot 10^{21}$ cm. This Larmor radius fits excellent with the radius of the circle in the helix in Figure 6.5, which means that the numerical solver works as expected when solving the differential equation Eq. (4.8).

The program has been compared to results from Elyiv et al. [21], which uses similar numerical routines. Using Markarian 421 as an example, with $D = 120$ Mpc and a primary photon energy E_{γ_0} according to Eq (5.10). The only notable difference between the two programs is the model for the magnetic field. Elyiv et al. use a magnetic field with constant field strength, divided into cubic cells of length 1 Mpc, where the magnetic field is oriented in a random direction for each cell. This program uses the continuous turbulent magnetic field as described in section 4.1 with a correlation length of 1 Mpc.

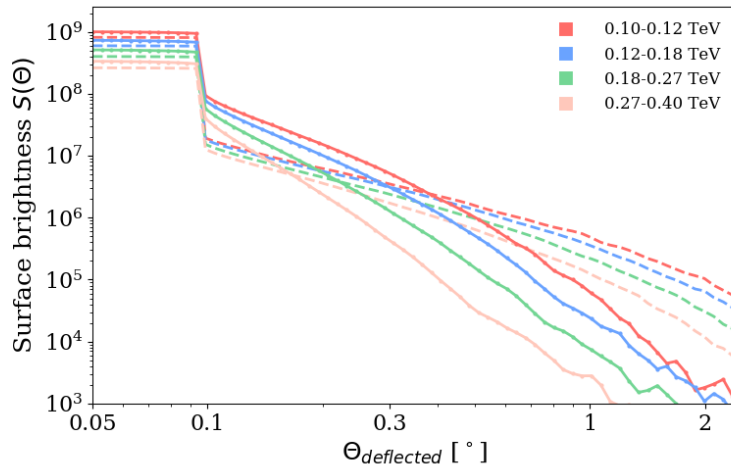


Figure 6.6: Surface brightness as a function of deflection angle for photons following the emission distribution from Eq. (5.10). The energy bins are sorted according to the energy of the detected photons. The dotted line is deflection in a turbulent magnetic field with $B_{\text{rms}} = 10^{-14}$ G, while the solid line is for $B_{\text{rms}} = 10^{-15}$ G.

Figure 6.6 is normalized to the same values as Figure B.1 from the paper of Elyiv et al., for better comparison. Each bin is normalized according to its size. The plateau from 0.05° to 0.1° is due to the homogeneous distribution within Fermi-LAT's point spread function, which in this case is set to have a constant angular containment radius $\vartheta_{\text{PSF}} \simeq 0.1^\circ$. The figures are in good agreement considering the drop from the plateau and the surface brightness relative to each bin. However, this figure seems to have a slightly more gradual decline than the one presented by Elyiv et al. Based on only analyzing the difference between the magnetic fields, it is peculiar that the decline does not have an opposite effect in this case. As implicitly mentioned in section 4.2 the magnetic field that Elyiv et al. use will deflect charged particles a factor $\sqrt{9/2}$ more than in the case of a continuous turbulent magnetic - this is also evident from Eq. (4.10) and Eq. (4.12) - which means that one would expect a steeper decline in Figure 6.6 than in Figure B.1. However, the more gradual slope is a rather small difference, which might also originate from different routines used for simulating interaction length, pair production and IC scattering.

6.3 SKY IMAGES

In this section, the main results from program simulations will be presented. The sky image plots are inspired by the article from Neronov et al. [28]. However, a direct comparison between results in this thesis and the results from Neronov et al. should be taken with care. Neronov et al. uses the cell spaced EGMF, described in section 4.2, with a correlation length of several Mpc. Also, they use a monochromatic energy distribution of primary γ -rays at $E_{\gamma_0} = 1$ TeV. Seeing that the magnetic field investigated in this report is of helical configuration, one should be careful of selecting a correlation length bigger than 1 Mpc. In fact, as is clear from Figure 2.3 and as argued by Durrer and Neronov [10], a helical EGMF

should have parameters in the area $10^{-4} \text{ Mpc} \lesssim L_c \lesssim 1 \text{ Mpc}$ and $10^{-13} \text{ G} \lesssim B_{\text{rms}} \lesssim 10^{-10} \text{ G}$. Nevertheless, the interpretation of Figure 2.3 should be done with care, and as argued in section 2.5, reasonable values for simulations are $L_c \simeq 1 \text{ Mpc}$ and $10^{-16} \text{ G} \leq B_{\text{rms}} \leq 10^{-13} \text{ G}$, using Eq. (2.5) from Durrer and Neronov as the upper boundary for the parameters of the EGMF.

The source considered here is the blazar 1ES 0229+200. It exists at redshift $z \simeq 0.14$, i.e. $D \simeq 540 \text{ Mpc}$. The Blazar has a Lorentz bulk factor $\Gamma = 10$, i.e. $\Theta_{\text{jet}} \simeq 6^\circ$. In the simulations the sampling parameter is set to $a_{\text{smp}} = 0$, to obtain varied statistics on the two-dimensional sky image. Two analyses of theoretical results from the the source will be presented. First, the time delay of secondaries will be considered by splitting the surface brightness sky image into the time bins listed in Table 6.1. Remember that τ refers to the time delay after the first non-interacting photon of a cascade reaches the Earth. The non-interacting photons ($\tau = 0$) are excluded in all figures presented in this section. This is because it is desirable to only visualize the effect from deflection by the EGMF, and as is evident from the plateau in Figure 6.6 the non-interacting photons outshines the secondary photons.

Table 6.1: List of time bins used in the simulations of the band images.

Time bin	Time delay
1	$0 \text{ yr} < \tau < 10^5 \text{ yr}$
2	$10^5 \text{ yr} \leq \tau < 10^6 \text{ yr}$
3	$10^6 \text{ yr} \leq \tau < 3 \cdot 10^6 \text{ yr}$
4	$3 \cdot 10^6 \text{ yr} \leq \tau < 10^7 \text{ yr}$

Also, the helicity of the EGMF will be evaluated. This is one of the critical investigations, as a difference between sky images for deflection in right-handed and left-handed turbulent magnetic fields would be a step closer to proving CP violation in the Early Universe. Only the cases of fully polarized fields will be considered, even though the field would probably never be fully polarized in one direction.

All following figures in this section are band images with a relative surface brightness profile. White color represents the brightest part of γ -ray sky, while black color represents a fraction 10^{-3} of the brightest point in each plot. All figures are presented with the color map that defines the surface brightness. All simulations use a magnetic field with Kolmogorov turbulence, which is generated by 100 modes with $k_{\text{max}} = 100 k_{\text{min}}$.

Figure 6.7 shows the sky image of a monochromatic emission at 1 TeV split into the epochs from Table 6.1, chronologically from the left. The source is located at the Origin of the angular axes, and has a jet pointing directly towards the Earth. All particles in this simulation are propagating in the same TMF, existing of equally many right-handed and left-handed modes (no helicity). The first epoch is more or less isotropic in the observed band image. This is evident from Eq. (5.9). If the time delay τ is known, one can use the equation to find the angular distance from the point source to the most luminous part of of the sky image. In Table 6.2 the expected angular offset brightness are listed for each epoch. For time bin 1, the angular distance is too small to be noticed in the figure. Besides, as argued in section 6.1, the lower energetic particles responsible for the most of the observable time delayed photons are

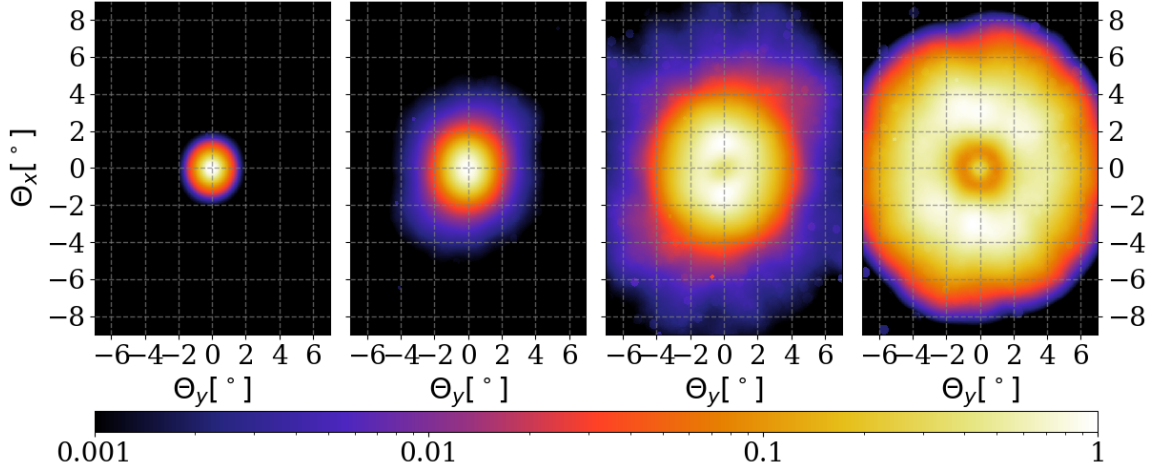


Figure 6.7: Band image of the sky region around a blazar with monochromatic emission spectrum of $E_{\gamma_0} = 1$ TeV. From the left; time bin 1, 2, 3 and 4. The simulations are done with $\Theta_{\text{obs}} = 0^\circ$, and $B_{\text{rms}} = 10^{-15}$ G.

less abundant than that of the higher energetic particle. This follows from more diffusion of lower energetic particles, thus a lower probability of reaching the Earth, which is also obvious from Figure 6.6. Time bin 2 should have a barely noticeable angular offset, but for no misalignment of the jet and a relatively big angular containment radius from the PSF, it is not visible in Figure 6.7. For time bin 3 and 4 the misalignment of the brightness profile becomes rather obvious. Time bin 3 has its brightest point around $\sim 1.5^\circ$, and time bin 4 has its brightest point around $\sim 3.5^\circ$. These values of δ are slightly below that of average time delay within their bin size. However, this might follow from a bigger contribution in abundance from less time delayed particles, i.e. the correct interpretation of a time bin's δ -value should be at a lower value of τ than the average.

Table 6.2: Expected angular brightness offset from Eq. (5.9), using $\Theta_{\text{jet}} = 6^\circ$ and $\Theta_{\text{obs}} = 0^\circ$.

Time bin	Average time delay	δ
1	$5 \cdot 10^4$ yr	$\simeq 0.03^\circ$
2	$5.5 \cdot 10^5$ yr	$\simeq 0.34^\circ$
3	$2 \cdot 10^6$ yr	$\simeq 1.24^\circ$
4	$6.5 \cdot 10^6$ yr	$\simeq 4.04^\circ$

As already mentioned in subsection 5.4.2, the equation for time delay Eq. (5.9) should be taken with care when comparing to simulated results. However, the formula seem to fit surprisingly well when simulating a monochromatic initial γ -ray spectrum at $E_{\gamma_0} = 1$ TeV. This is a clear sign that the program works as expected.

Also, it would be interesting to observe how the time delay equation perform for a jet that is misaligned towards the Earth, and for different values of B_{rms} .

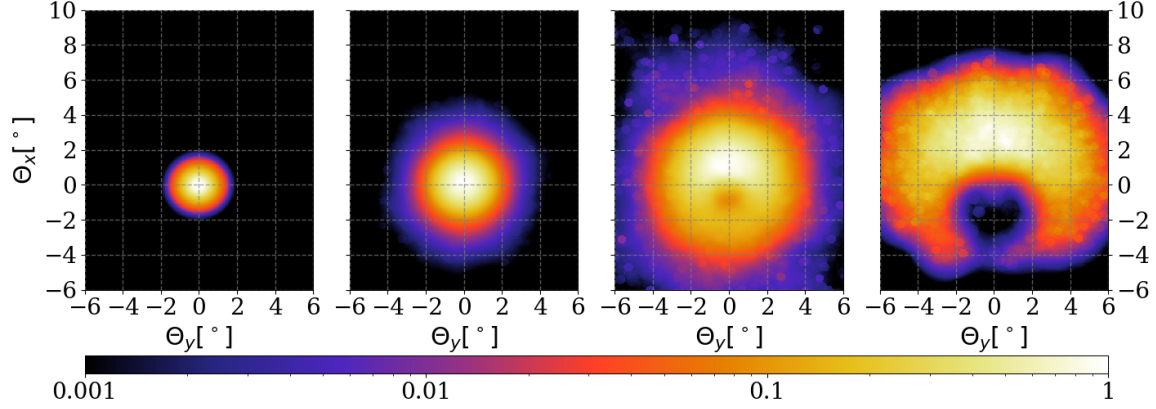


Figure 6.8: Band image of the sky region around a blazar with monochromatic emission spectrum of $E_{\gamma_0} = 1$ TeV. From the left; time bin 1, 2, 3 and 4. The simulations are done with $\Theta_{\text{obs}} = \frac{1}{2}\Theta_{\text{jet}} = 3^\circ$, and $B_{\text{rms}} = 10^{-16}$ G.

Figure 6.8 shows the surface brightness band image around the source for particles interacting with an EGMF of $B_{\text{rms}} = 10^{-14}$ G and a jet misalignment $\Theta_{\text{obs}} = 6^\circ$. By Eq. (5.9) δ also depends on Θ_{obs} , which means that for the numerical values of δ in Table 6.2 to hold in this case, they have to be multiplied by a factor $2/3$. One can now barely notice a small angular shift in time bin 2. When observing the blue surface band, it stretches further in positive Θ_x -direction than in negative Θ_x -direction, i.e. a minor shift in the angular intensity. Moreover, time bin 3 and 4 now has their brightest spots at respectively $\sim 1^\circ$ and $\sim 2.5^\circ$, which is more or less consistent with the results from Figure 6.7 when accounting for the factor $2/3$.

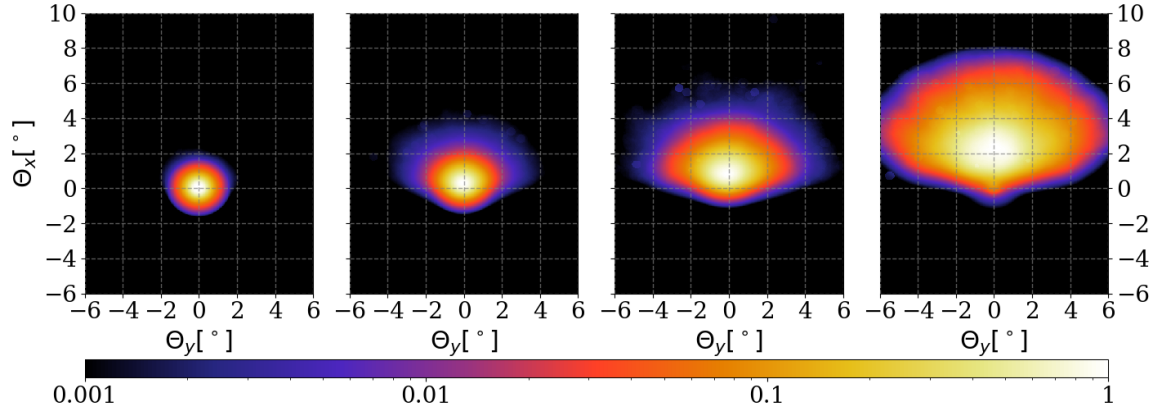


Figure 6.9: Band image of the sky region around a blazar with monochromatic emission spectrum of $E_{\gamma_0} = 1$ TeV. From the left; time bin 1, 2, 3 and 4. The simulations are done with $\Theta_{\text{obs}} = \Theta_{\text{jet}} = 6^\circ$, and $B_{\text{rms}} = 10^{-14}$ G.

Figure 6.9 shows the surface brightness band image around the source, for particles being deflected by an EGMF of $B_{\text{rms}} = 10^{-14}$ G. The source has a jet misalignment $\Theta_{\text{obs}} = 6^\circ$. For the numerical values of δ in Table 6.2 to hold in this case, they have to be multiplied by a factor $1/2$. One can now notice a small angular shift in time bin 2. All surface bands are slightly shifted in positive Θ_x -direction. However, the expected angular distance from the source is

now $\delta \simeq 0.17^\circ$, which is too small for the PSF to separate this signal from the Origin. Also, the brightness profile for time bin 1 and 2 in this figure is more or less consistent with the brightness profiles in Figure 6.7 and Figure 6.8, when accounting for the factor 1/2.

Dolag et al. [29] uses the energy distribution function from Eq. (5.11). For the simulations done here, the energy distribution will also follow Eq. (5.11), with a sharp cutoff at $E_{\max} = 20$ TeV and a minimum energy cutoff at $E_{\min} = 1$ GeV. All simulations are done with the magnetic field strength $B_{\text{rms}} = 10^{-13}$ G, $B_{\text{rms}} = 10^{-14}$ G, $B_{\text{rms}} = 10^{-15}$ G and $B_{\text{rms}} = 10^{-16}$ G, and for both left-handed and right-handed polarization. They are also done with the same set of random parameters for the magnetic field for each polarization. The correlation length of the magnetic field is $L_c \simeq 1$ Mpc for all simulations. A uniform jet distribution will be used. The power spectrum of the magnetic field is still for Kolmogorov turbulence. However, it should be emphasized that any desired power spectrum for $\gamma > 0$ can be used, which was motivated in section 4.2.

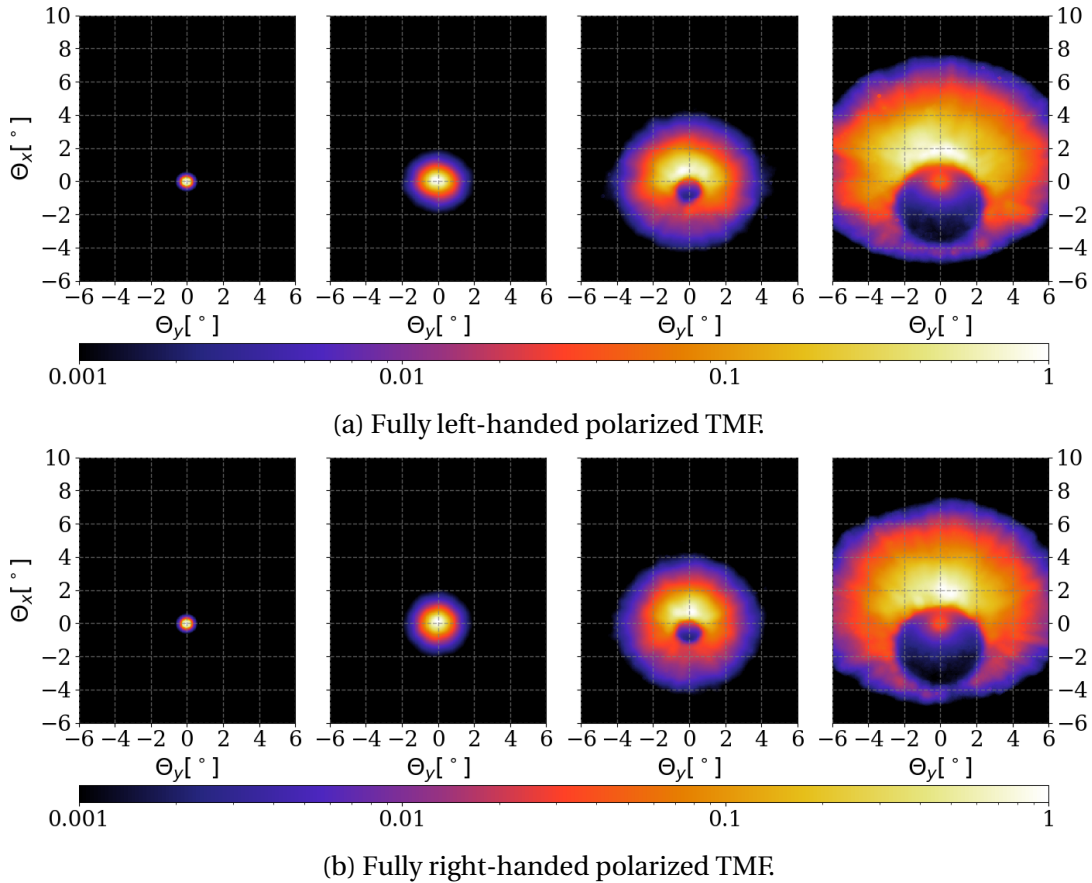


Figure 6.10: Band image of the sky region around a blazar emitting photons according to the energy distribution in Eq. (5.11). From the left; time bin 1, 2, 3 and 4. The simulations are done with $\Theta_{\text{obs}} = \frac{1}{2}\Theta_{\text{jet}} = 3^\circ$, and $B_{\text{rms}} = 10^{-14}$ G.

Figure 6.10 shows the sky images around the source for both boundaries of the polarization in a magnetic field with field strength $B_{\text{rms}} = 10^{-14}$ G. Here, like in Figures 6.7 – 6.9 the sky images are split into the epochs from Table 6.1 to more clearly visualize a small

difference from the polarization of the fields. In Figure 6.10a the field is left polarized, while in Figure 6.10b the field is right polarized. Time bin 1 cannot be analyzed for this field strength, as there has not been enough deflection in this epoch. It is expected for completely isotropic magnetic fields that the band images should be symmetric over the Θ_x -axis. However, in time bin 2, 3 and 4 the band images are slightly asymmetrical over this axis. The band images also seem to be differently transformed for the chosen helicity of the magnetic field.

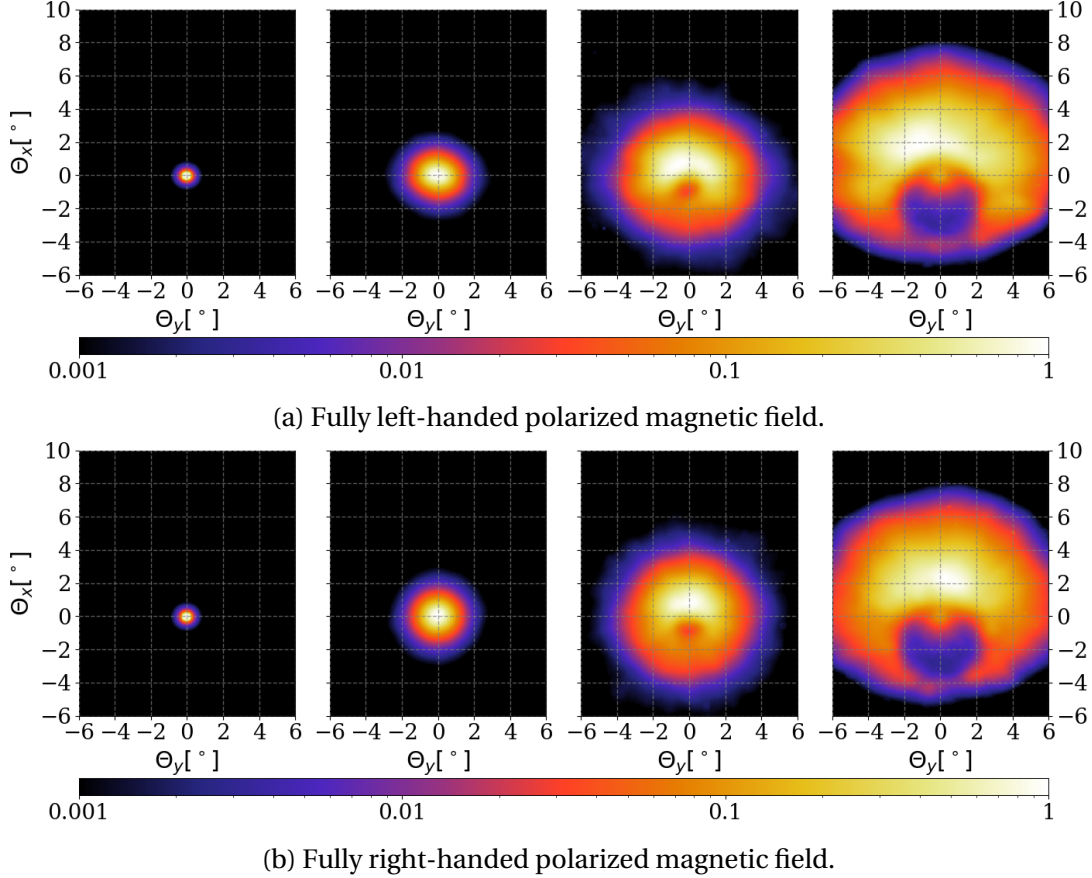


Figure 6.11: Band image of the sky region around a blazar emitting photons according to the energy distribution in Eq. (5.11). From the left; time bin 1, 2, 3 and 4. The simulations are done with $\Theta_{\text{obs}} = \frac{1}{2}\Theta_{\text{jet}} = 3^\circ$, and $B_{\text{rms}} = 10^{-15}$ G.

Figure 6.11 shows the same band images as Figure 6.10, but for a weaker magnetic field. The band images show that the surface brightness actually has a broader detectable dispersion for the weaker field. This can be understood by looking at Figure 6.6, which shows that the surface brightness is larger for $B_{\text{rms}} = 10^{-15}$ G than for $B_{\text{rms}} = 10^{-14}$ G, when considering surface brightness above $\sim 10^{-3}$ of the maximal value. Thus, in this case, it is easier to distinguish the left- and right-handed polarization when evaluating the sky image in a weaker field. The deformations of the band image is clearly different for the left-handed magnetic field in Figure 6.11a and the right-handed magnetic field in Figure 6.11b. The deformation is also present in Figure B.2 and Figure B.3, which are band images from simulations done with $B_{\text{rms}} = 10^{-13}$ G and $B_{\text{rms}} = 10^{-16}$ G respectively. However, these

results have to be taken with care as the simulations were run with only one set of random parameters for each polarized field. To be able to make a reliable conclusion from such results, a large amount of different sets of random parameters for each polarization must be tested. Nevertheless, the simulations show that the polarizations of the magnetic fields can be distinguished by observing the sky image. Therefore, it would be interesting to test for many different parametrizations of the polarized magnetic fields, and perhaps find a consistent difference between the left-handed and the right-handed polarized field.

Assuming that the Earth resides within the jet, it is most probable that the Earth is in the outermost region of the opening angle. This can easily be derived from the geometrical cross section of the jet, which gives $dN_{\text{source}}/d\Theta_{\text{obs}} \propto \Theta_{\text{obs}}$. Therefore, it would be beneficial to run simulations where $\Theta_{\text{obs}} = \Theta_{\text{jet}}$.

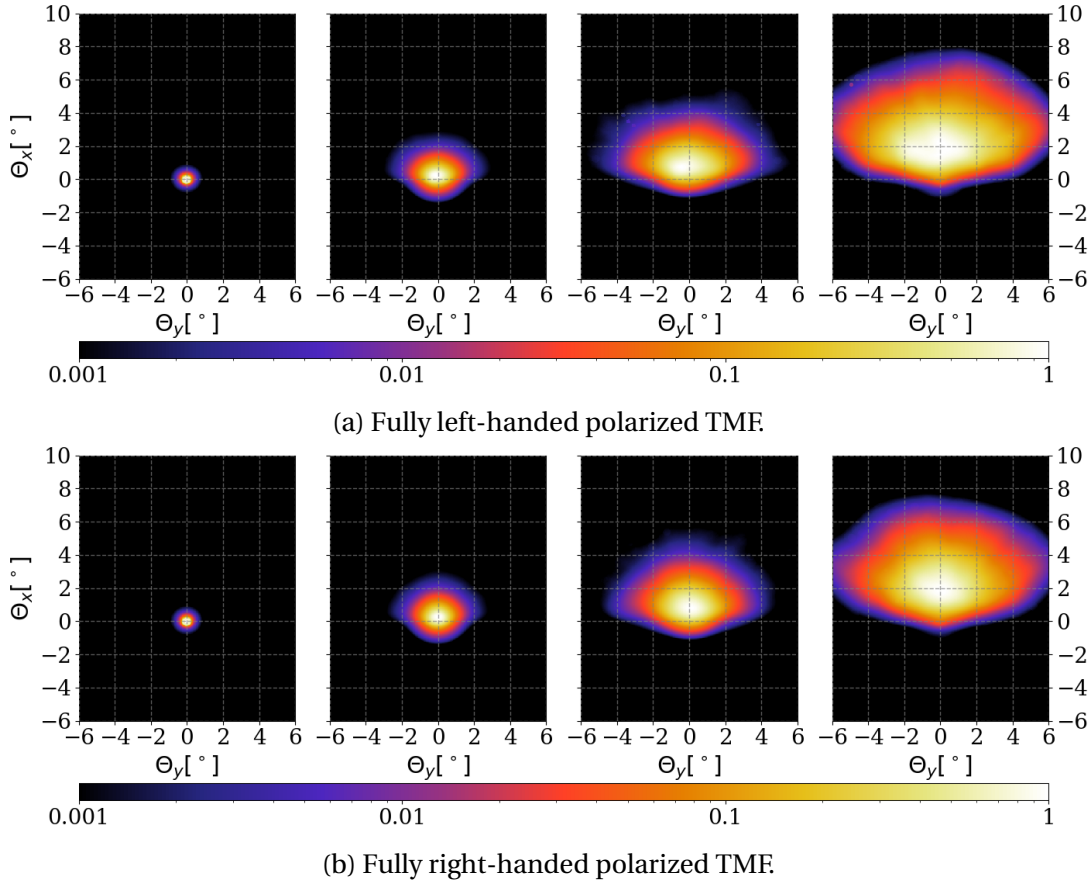


Figure 6.12: Band image of the sky region around a blazar emitting photons according to the energy distribution in Eq. (5.11). From the left; time bin 1, 2, 3 and 4. The simulations are done with $\Theta_{\text{obs}} = \Theta_{\text{jet}} = 6^\circ$, and $B_{\text{rms}} = 10^{-15}$ G.

Now, only changing the misalignment angle $\Theta_{\text{obs}} = 3^\circ \rightarrow \Theta_{\text{obs}} = 6^\circ$, the sky images from Figure 6.11 will look like the sky images in Figure 6.12. The difference between the images from a left-handed polarized field in Figure 6.12a and from a right-handed polarized field in Figure 6.12b becomes more apparent. The band images in Figure 6.12a are more stretched out in Θ_y -direction, while in Figure 6.12b the band images are more stretched out in Θ_x -direction.

This is also the case when running simulations for magnetic field strength $B_{\text{rms}} = 10^{-13}$ G, $B_{\text{rms}} = 10^{-14}$ G and $B_{\text{rms}} = 10^{-16}$ G shown in Figure B.4 – B.6 respectively. Once again, this might solely depend on the initial magnetic field randomization, thus more simulations are needed to give a clear conclusion on what sky images to expect for different polarizations of the magnetic field. It should also be noted that using only 100 modes for generating the magnetic field might be too few. To ensure an isotropic field, it should be considered using 200 or more modes.

Now, adding a Gaussian distribution to the primary γ -ray jet, with weight according to $w = \exp(-\Theta_s^2/\Theta_{\text{jet}})$, where Θ_s is the angle between the initial momentum of the primary photon and the center of the jet.

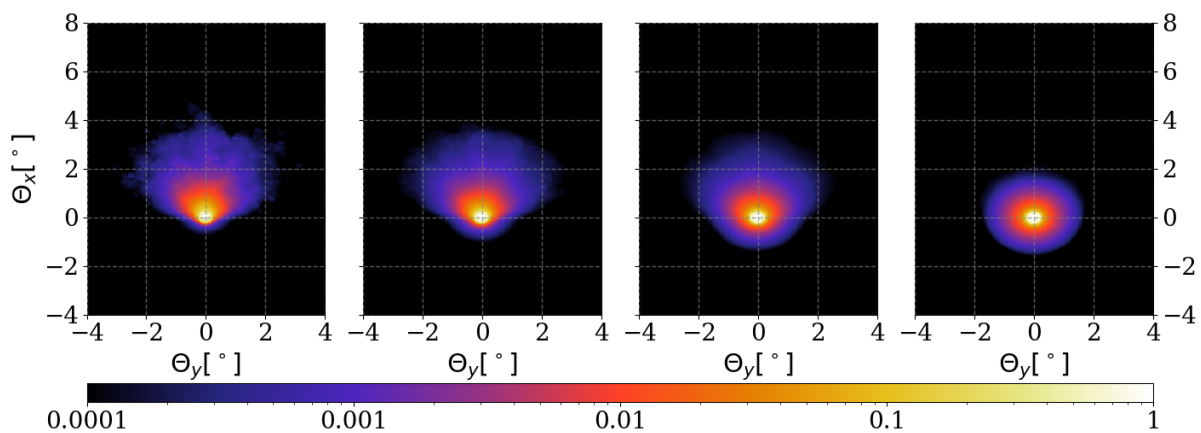


Figure 6.13: Band image of the sky region around a blazar integrated over time. Source emitting photons according to the energy distribution in Eq. (5.11) and with a Gaussian jet distribution profile. From the left; using a magnetic field with strength $B_{\text{rms}} = 10^{-13}$ G, $B_{\text{rms}} = 10^{-14}$ G, $B_{\text{rms}} = 10^{-15}$ G and $B_{\text{rms}} = 10^{-16}$ G. The simulations are done with $\Theta_{\text{obs}} = \Theta_{\text{jet}} = 6^\circ$, and with right-handed polarization.

In Figure 6.13 the brightness has been integrated over all epochs to visualize the expected image from a steady emitting source. Note that the figure is still excluding the non-interacting photons. As the lifetime of an AGN is in the order $T_{\text{AGN}} \simeq 10^7$ yr [28], these sky images would be relevant when observing a dead TeV blazar. From the left, Figure 6.13 shows the sky image for a magnetic field strength $B_{\text{rms}} = 10^{-13}$ G, $B_{\text{rms}} = 10^{-14}$ G, $B_{\text{rms}} = 10^{-15}$ G and $B_{\text{rms}} = 10^{-16}$ G. Comparing the sky images in Figure 6.13 with data from Fermi and IACTs, e.g. HESS or MAGIC, it could be possible to set a lower boundary on the strength of the EGMF. This boundary would be for a turbulent helical EGMF with correlation length $L_c \simeq 1$ Mpc.

As argued in section 3.3, a different configuration of correlation length and field strength for the EGMF might also fit the detection. Therefore, constraints on the EGMF must be evaluated in the parameter-space of L_c and B_{rms} of the EGMF, like in Figure 2.3. By doing so, the possible configurations of the EGMF can be constricted further than the already theoretical boundaries from Durrer and Neronov [10]. With the development of a new IACT, the Cherenkov Telescope Array, hopefully more statistics on VHE γ -rays reaching the atmosphere of the Earth will be available. The generalization of the Monte Carlo program ELMAG makes it possible to easily calculate sky images for any desired source, i.e. statistics from different

sources can be accumulated and compared to set boundaries on the parameters of the helical EGMF.

A helicity of the EGMF could prove CP violation in the Early Universe, which would be astonishing results, considering it might reconcile the Standard Model of particle physics and the Standard Model of cosmology. The results from ELMAG should also be evaluated in comparison to other theories, e.g. the analysis presented by Tashiro et al. [4]. They consider signals on the γ -ray sky that originates from the alleged same point source. Each photon can be backtracked based on the attenuation lengths from Eq. (3.24) and Eq. (3.25), and a geometrical representation similar to Figure 5.2. By knowing the energy of each photon, they assume that the highest energy photon is representing the jet center of the blazar. Now, using three energy bins, and arranging them by energy accordingly $E_1 < E_2 < E_3$, Tashiro et al. present the statistics formula

$$Q(E_1, E_2, E_3, R) = \frac{1}{N_3} \sum_{k=1}^{N_3} \boldsymbol{\eta}_1 \times \boldsymbol{\eta}_2 \cdot \mathbf{n}_k(E_3). \quad (6.1)$$

Here R represents the angular radius of the patch size on the sampled γ -ray sky. N_3 is the number of photons in energy bin E_3 , while \mathbf{n}_k is the unit vector pointing from the center of patch towards the source. $\boldsymbol{\eta}_1$ and $\boldsymbol{\eta}_2$ are essentially the vectors on the sky patch, pointing from the source location to the average location of the photons in energy bin E_1 and E_2 respectively. If Q is positive it implies that there is an excess of right-handed helices in the EGMF, and a negative value of Q implies an excess of left-handed helices in the EGMF. Based on observation from Fermi-LAT, Tashiro et al. suggest that the EGMF should be left-handed with $B_{\text{rms}} \simeq 10^{-14}$ G and $L_c \simeq 10$ Mpc. However, this analysis assumes that all detected photons within the patch of the γ -ray sky are from the same source, in addition to no detector anomaly. These assumptions are rather bold, which means that one would require more statistics and a more precise PSF of Fermi-LAT to make a reliable prediction. Nevertheless, by cross-referencing the analysis from Tashiro et al. and the Monte Carlo simulations from ELMAG, the parameters of the EGMF can be constrained even further. Thus, yet another confirmation that ELMAG will be relevant for future work within the task of determining the parameters of the EGMF.

6.4 FUTURE WORK

The polarization of the EGMF should be evaluated further. A more detailed statistical treatment is required before one can draw a conclusion of how the different polarized fields affect the band image.

Further work with this program would be to implement a more accurate distribution function inside the Fermi-LAT's PSF. This could be a trivial Gaussian profile or the more complex two-dimensional King profile [31] recommended by the Fermi Collaboration [32]. The results from ELMAG should also be compared to the data from Fermi-LAT, which can be retrieved through Fermi Science Tools.

As mentioned in section 6.2, other similar programs use a cubic cell spaced EGMF with a uniform field in each cell oriented in a random direction in the three-dimensional space.

In order to compare results from ELMAG more accurately to results from these programs, it would be necessary to include a routine for generating such an EGMF distribution. This should be a rather straight forward process, seeing that all implementations necessary can be contained in the bturb.f90 file.

In this thesis electromagnetic cascades from a VHE γ -ray emitter have been described in detail. Cross sections between γ -rays and the EBL, and VHE charged particles and the background photons have been derived. Deflection of charged particles in a turbulent magnetic field and theoretical boundaries to the parameters of the EGMF have also been presented. The program ELMAG has been presented in detail, with its previous functionality and the new features developed during this Master thesis.

During the development of ELMAG, all new routines have been tested extensively, and proved to produce the expected results. For solving the Lorentz force ODE in a turbulent magnetic field, an adaptive stepsize solver has been implemented. It was chosen based on both its efficiency and precision for turbulent fields, and has been tested to give satisfactory results compared to theoretical predictions, e.g. charged particle deflection in a turbulent magnetic field or solving for the expected Larmor radius in a uniform magnetic field.

The program ELMAG can now calculate three-dimensional electromagnetic cascades evolving from an extragalactic point source. A turbulent magnetic field has been implemented, where any desired field strength, power spectrum, helicity and correlation length can be specified. The program has preserved all previous implementations, and the old program is implemented within the new version. By now calculating the three-dimensional evolution of the cascade, the program can simulate the expected observed sky image from any desired source with any desired turbulent magnetic field. The output routine for the two-dimensional grid representing the sky image, and a python-file for plotting purposes, are available in the new release of ELMAG. Also, the program can now account for any desired jet distribution profile. Further development of the program should be to include a cubic cell spaced magnetic field, for comparing to other similar cascade programs. Moreover, it is desirable to compare theoretical results from ELMAG with data from detectors, e.g. Fermi-LAT.

Band images of γ -ray sky around the blazar 1ES 0229+200 have been produced, and shows brightness profiles in agreement with theoretical predictions. Helicity of the EGMF has also been tested. Further tests of different initialized magnetic fields are necessary to conclude what distinguishes the differently polarized fields. However, some deviance was observed,

which opens for further investigation of a polarized helical EGMF. This means that ELMAG can be paramount in the continual search for a polarized EGMF, which again can prove CP violation in the Early Universe.

The complete program is open source and can be downloaded from [33]. ELMAG is warmly recommended for Monte Carlo simulations of extragalactic electromagnetic cascades detectable in the γ -ray sky above ~ 1 GeV.

- ¹C. Grupen, *Astroparticle physics* (Springer, 2005).
- ²C. L. Bennett et al., “Nine-Year Wilkinson Microwave Anisotropy Probe (WMAP) Observations: Final Maps and Results”, *Astrophys. J. Suppl.* **208**, 20 (2013).
- ³A. A. Penzias and R. W. Wilson, “A Measurement of excess antenna temperature at 4080-Mc/s”, *Astrophys. J.* **142**, 419–421 (1965).
- ⁴H. Tashiro, W. Chen, F. Ferrer, and T. Vachaspati, “Search for CP Violating Signature of Intergalactic Magnetic Helicity in the Gamma Ray Sky”, *Mon. Not. Roy. Astron. Soc.* **445**, L41–L45 (2014).
- ⁵M. Kachelriess, S. Ostapchenko, and R. Tomas, “ELMAG: A Monte Carlo simulation of electromagnetic cascades on the extragalactic background light and in magnetic fields”, *Comput. Phys. Commun.* **183**, 1036–1043 (2012).
- ⁶S. Perlmutter et al., “Measurements of Omega and Lambda from 42 high redshift supernovae”, *Astrophys. J.* **517**, 565–586 (1999).
- ⁷T. K. Gaisser, R. Engel, and E. Resconi, *Cosmic Rays and Particle Physics* (Cambridge University Press, 2016).
- ⁸A. A. Abdo et al., “Fermi large area telescope observations of Markarian 421: The missing piece of its spectral energy distribution”, *Astrophys. J.* **736**, 131 (2011).
- ⁹A. Cooray, “Extragalactic Background Light: Measurements and Applications”, (2016).
- ¹⁰R. Durrer and A. Neronov, “Cosmological Magnetic Fields: Their Generation, Evolution and Observation”, *Astron. Astrophys. Rev.* **21**, 62 (2013).
- ¹¹D. Grasso and H. R. Rubinstein, “Magnetic fields in the early universe”, *Phys. Rept.* **348**, 163–266 (2001).
- ¹²D. Griffiths, *Introduction to elementary particles* (2008).
- ¹³M. Thomson, *Modern Particle Physics* (Cambridge University Press, 2013).
- ¹⁴M. E. Peskin and D. V. Schroeder, *An introduction to quantum field theory* (Westview, Boulder, CO, 1995).

- ¹⁵E. Dwek and F. Krennrich, “The Extragalactic Background Light and the Gamma-ray Opacity of the Universe”, *Astropart. Phys.* **43**, 112–133 (2013).
- ¹⁶V. V. Vassiliev, “Extragalactic background light absorption signal in the TeV gamma-ray spectra of blazars”, *Astropart. Phys.* **12**, 217–238 (2000).
- ¹⁷T. M. Kneiske and H. Dole, “A Lower-Limit Flux for the Extragalactic Background Light”, *Astron. Astrophys.* **515**, A19 (2010).
- ¹⁸A. Neronov and I. Vovk, “Evidence for strong extragalactic magnetic fields from Fermi observations of TeV blazars”, *Science* **328**, 73–75 (2010).
- ¹⁹J. Giacalone and J. R. Jokipii, “The Transport of Cosmic Rays across a Turbulent Magnetic Field”, *The Astrophysical Journal* **520**, 204–214 (1999).
- ²⁰D. Harari, S. Mollerach, E. Roulet, and F. Sanchez, “Lensing of ultrahigh-energy cosmic rays in turbulent magnetic fields”, *JHEP* **03**, 045 (2002).
- ²¹A. Elyiv, A. Neronov, and D. V. Semikoz, “Gamma-ray induced cascades and magnetic fields in intergalactic medium”, *Phys. Rev.* **D80**, 023010 (2009).
- ²²C. Caprini and S. Gabici, “Gamma-ray observations of blazars and the intergalactic magnetic field spectrum”, *Phys. Rev.* **D91**, 123514 (2015).
- ²³J. Miralda-Escude and E. Waxman, “Signatures of the origin of high-energy cosmic rays in cosmological gamma-ray bursts”, *Astrophys. J.* **462**, L59–L62 (1996).
- ²⁴W. H. Press, S. a. Teukolsky, W. T. Vetterling, and B. P. Flannery, *Numerical Recipes in Fortran 77: the Art of Scientific Computing. Second Edition*, Vol. 1 (1996).
- ²⁵D. J. Griffiths, *Introduction to electrodynamics; 3rd ed.* (Prentice-Hall, Upper Saddle River, NJ, 1999).
- ²⁶V. N. Baier, V. M. Katkov, and V. M. Strakhovenko, *Electromagnetic processes at high energies in oriented single crystals* (1998).
- ²⁷W. H. Press, S. A. Teukolsky, W. T. Vetterling, and B. P. Flannery, *Numerical recipes in fortran 90 (2nd ed.): the art of parallel scientific computing* (Cambridge University Press, New York, NY, USA, 1996).
- ²⁸A. Neronov, D. Semikoz, M. Kachelriess, S. Ostapchenko, and A. Elyiv, “Degree-scale GeV ‘jets’ from active and dead TeV blazars”, *Astrophys. J.* **719**, L130 (2010).
- ²⁹K. Dolag, M. Kachelriess, S. Ostapchenko, and R. Tomas, “Lower limit on the strength and filling factor of extragalactic magnetic fields”, *Astrophys. J.* **727**, L4 (2011).
- ³⁰*Message passing interface forum. mpi: a message passing interface standard*, (1995) <http://www.mpi-forum.org>.
- ³¹A. M. Read, S. R. Rosen, R. D. Saxton, and J. Ramirez, “A New Comprehensive 2-D Model of the Point Spread Functions of the XMM-Newton EPIC Telescopes : Spurious Source Suppression and Improved Positional Accuracy”, *Astron. Astrophys.* **534**, A34 (2011).

BIBLIOGRAPHY

³²*Fermi gamma-ray space telescope, the point spread function*, (2018) https://fermi.gsfc.nasa.gov/ssc/data/analysis/documentation/Cicerone/Cicerone_LAT_IRFs/IRF_PSF.html.

³³*Elmag*, (2019) <http://elmag.sourceforge.net/>.

ACRONYMS

AGN	Active Galactic Nucleus.
CMB	Cosmic microwave background.
COB	Cosmic optical background.
CR	Cosmic ray.
EBL	Extragalactic background light.
EGMF	Extragalactic magnetic field.
IACT	Imaging Atmospheric Cherenkov Telescope.
IC	Inverse Compton scattering.
ODE	Ordinary differential equation.
PSF	Point spread function.
QED	Quantum electrodynamics.
QFT	Quantum field theory.
VHE	Very high energy.

Appendices



APPENDIX A

MANDELSTAM VARIABLES

In 1958 Stanley Mandelstam introduced his relativistic scalar invariant variables. The variables consist of s , t , and u and refers to the different channels of tree level Feynman diagrams.

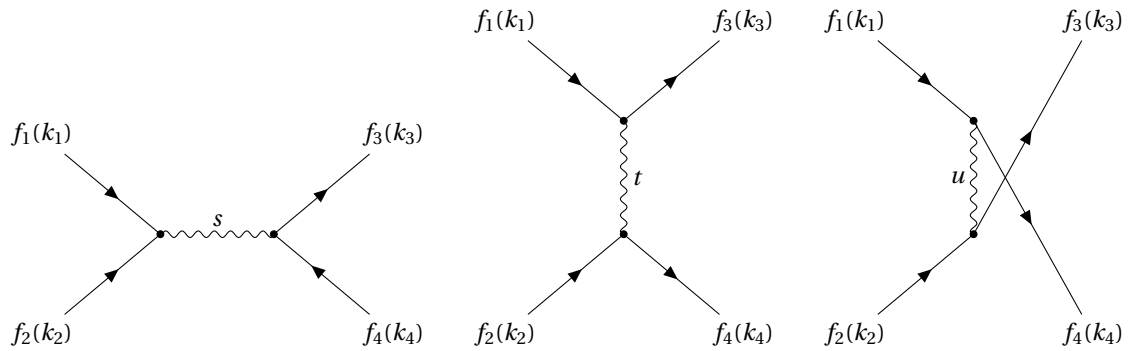


Figure A.1: Tree level Feynman diagrams representing the s -channel, t -channel and u -channel (from the left).

The Mandelstam variables represent the squared four-momentum of the internal propagator, thus by Figure A.1 the equations for s , t and u becomes

$$\begin{aligned}
 s &= (k_1 + k_2)^2 = (k_3 + k_4)^2 \\
 t &= (k_1 - k_3)^2 = (k_2 - k_4)^2 \\
 u &= (k_1 - k_4)^2 = (k_2 - k_3)^2.
 \end{aligned}
 \tag{A.1}$$

The Mandelstam variables are frequently used to shorten amplitude expressions in particle physics. They are also favorable to use when performing crossing symmetry. Letting each particle f_i have a rest mass m_i , another relation of the variables is that

$$s + t + u = \sum_{i=1}^4 m_i^2.
 \tag{A.2}$$

APPENDIX B

ADDITIONAL FIGURES

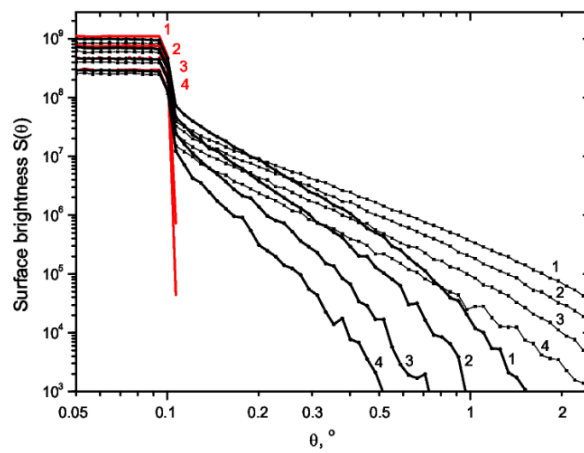


Figure B.1: Surface brightness plot from Elyiv et al. [21]. The thin line is deflection in a cubic cell spaced EGMF with $B = 10^{-14}$ G, while the thick line is for $B = 10^{-15}$ G.

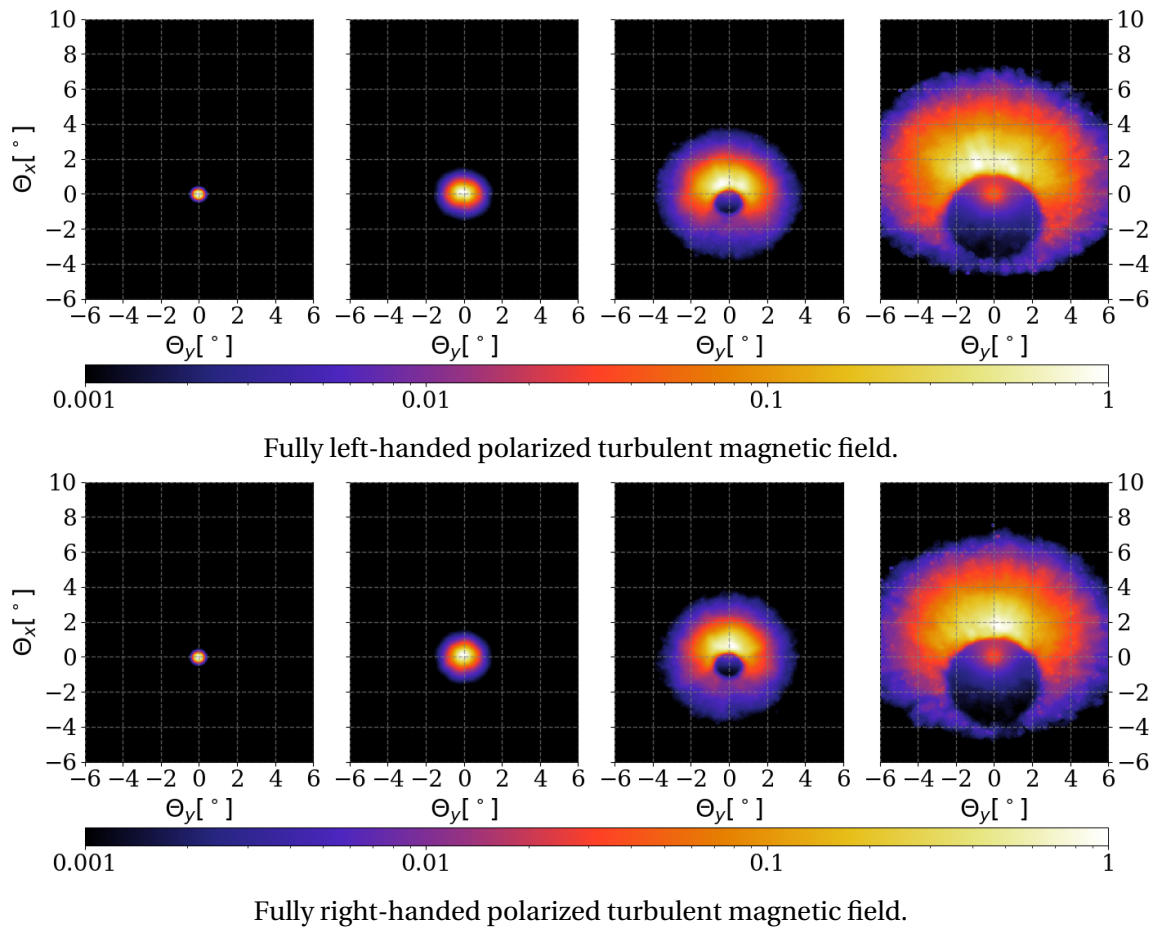


Figure B.2: Band image for $\Theta_{\text{obs}} = 3^\circ$ and $B_{\text{rms}} = 10^{-13}$ G, split into the epochs from Table 6.1.

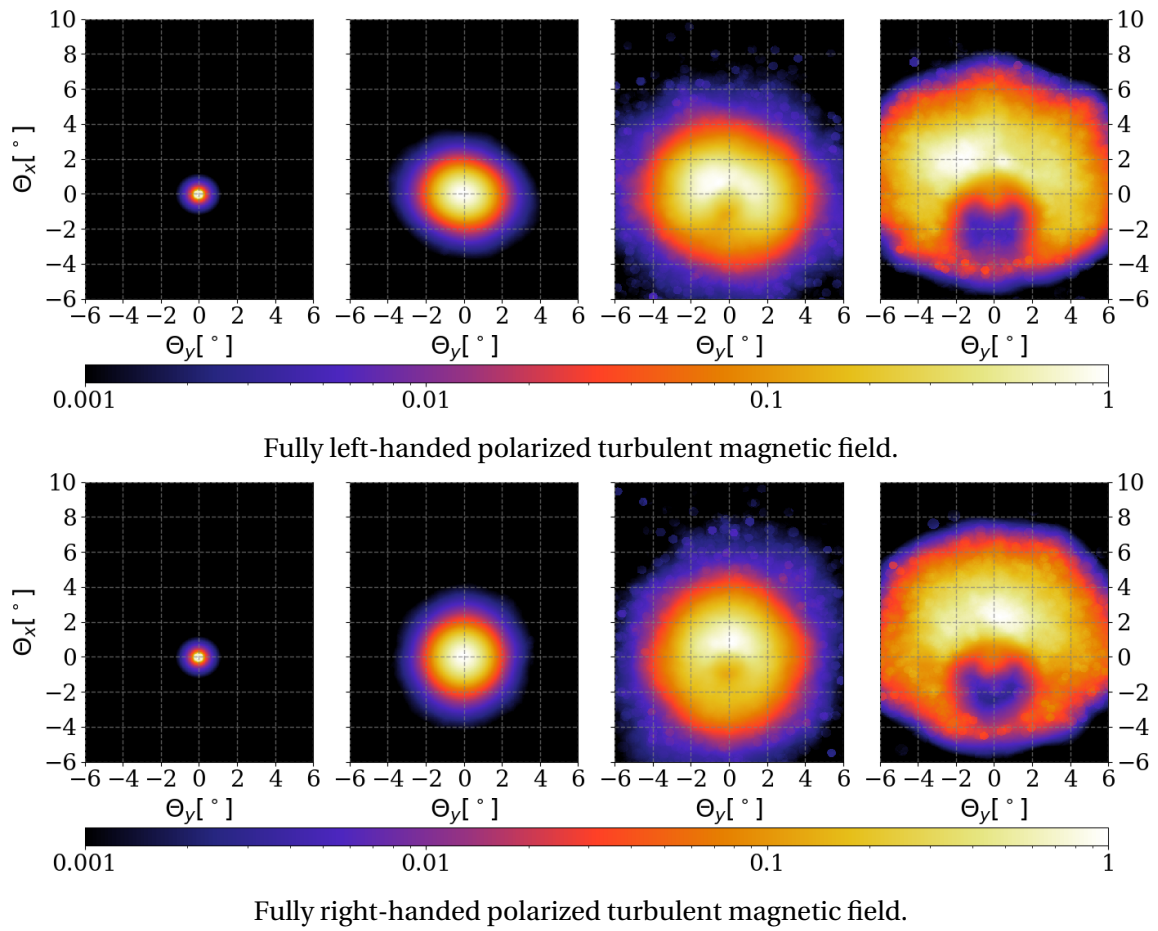


Figure B.3: Band image for $\Theta_{\text{obs}} = 3^\circ$ and $B_{\text{rms}} = 10^{-16}$ G, split into the epochs from Table 6.1.

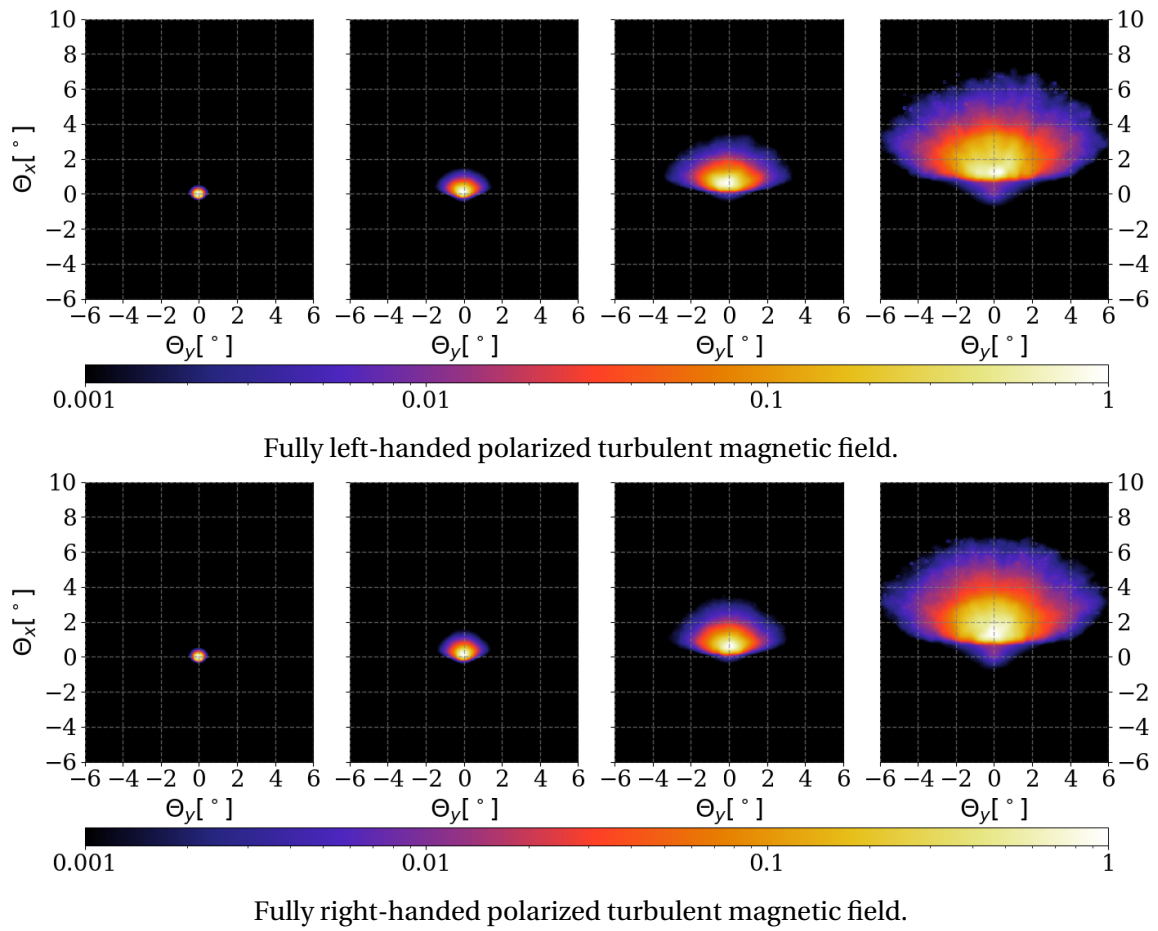


Figure B.4: Band image for $\Theta_{\text{obs}} = 6^\circ$ and $B_{\text{rms}} = 10^{-13}$ G, split into the epochs from Table 6.1.

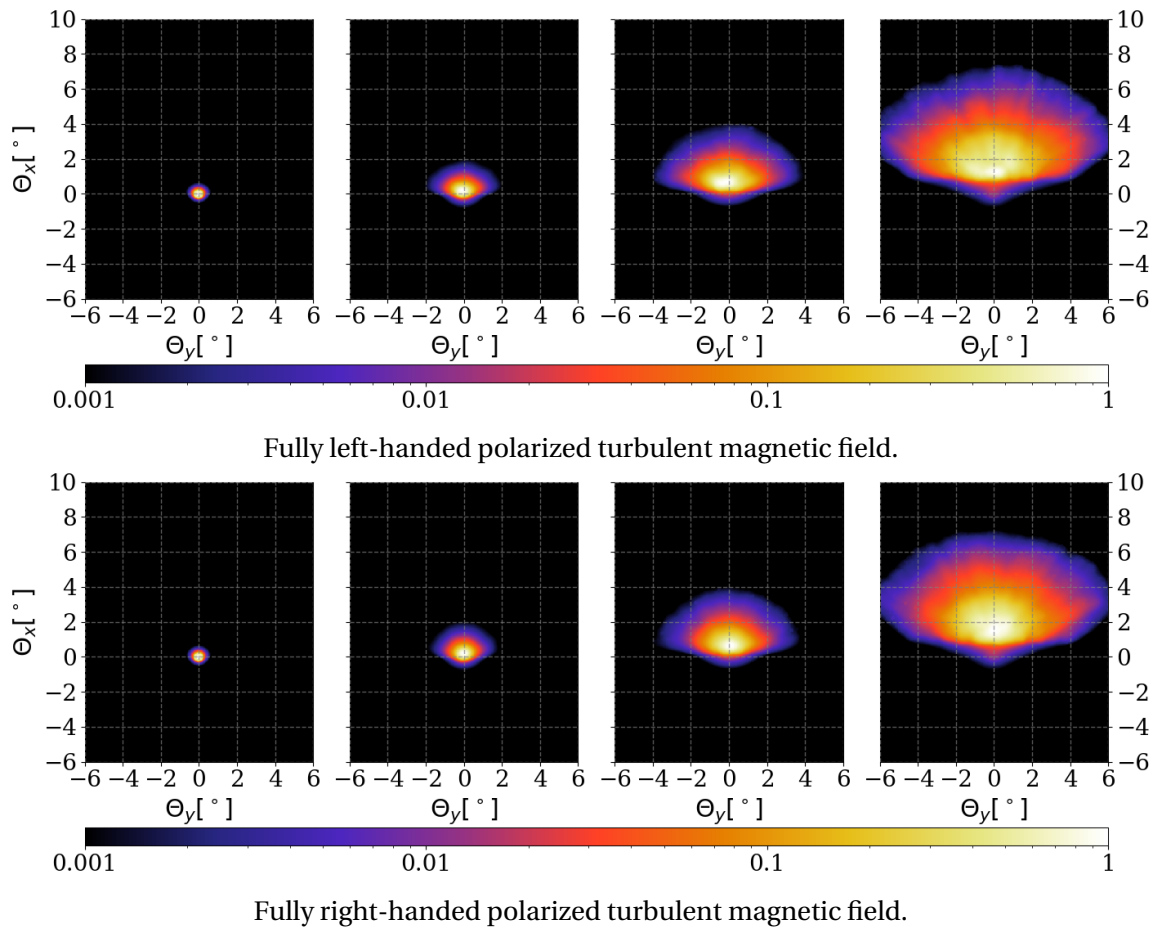


Figure B.5: Band image for $\Theta_{\text{obs}} = 6^\circ$ and $B_{\text{rms}} = 10^{-14}$ G, split into the epochs from Table 6.1.

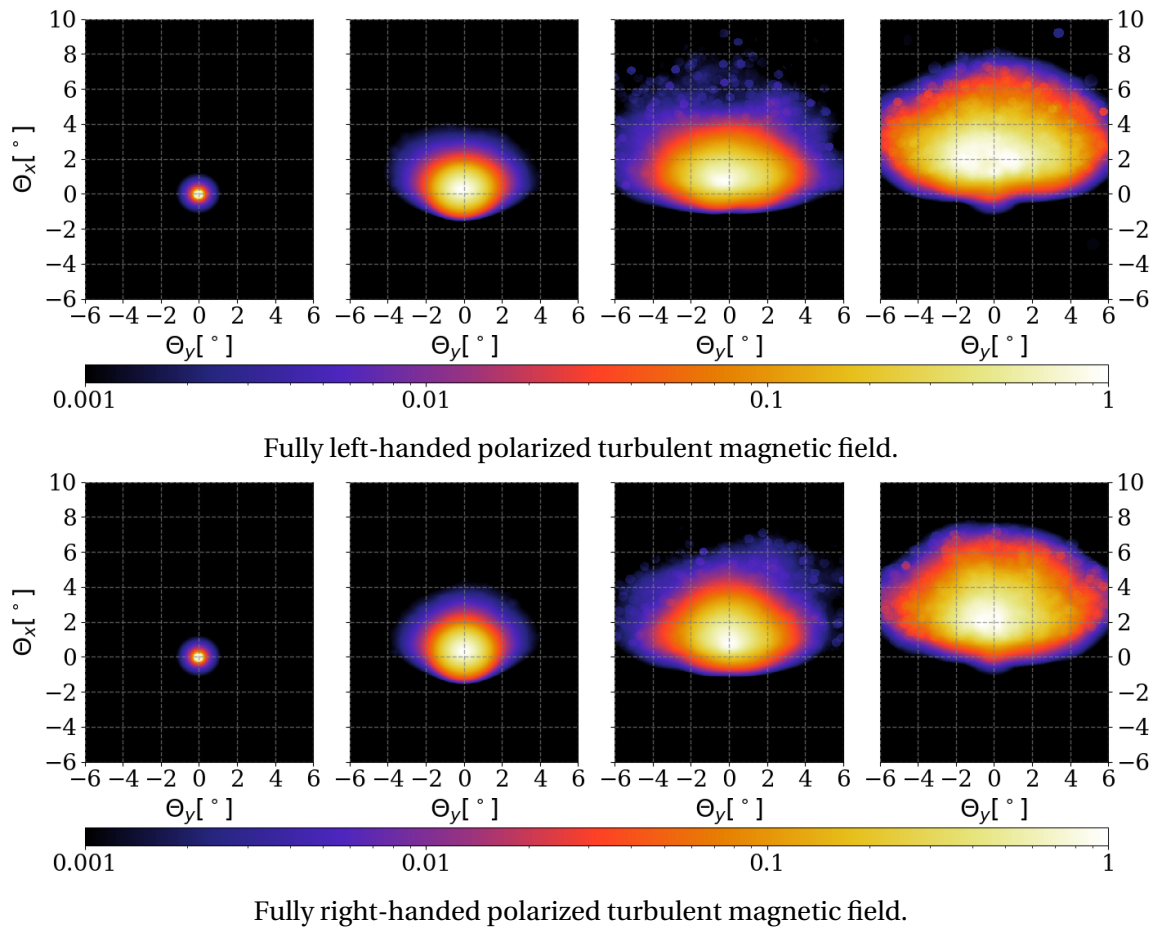


Figure B.6: Band image for $\Theta_{\text{obs}} = 6^\circ$ and $B_{\text{rms}} = 10^{-16}$ G, split into the epochs from Table 6.1.

